CALCIUM SULPHOALUMINATE HYDRATES:
crystal growth, stability and flow properties

Camelia Maria Vladu

A thesis submitted for the degree of Doctor of Philosophy

School of Engineering & Electronics
The University of Edinburgh

October 2005

to my parents

... for a lifetime of love and support

and Marc
... 'who already knew the answers'

Abstract

The calcium sulphoaluminate hydrates are important components of portland cement and constitute the principal matrix formers of some sulphoaluminate cements. Their practical importance lies in the involvment as intermediates and products of the hydration of portland cements under geothermal conditions. Ettringite is a complex mineral ($Ca_6[Al(OH)_6]_2(SO_4)_3 \cdot 26H_2O$) formed during the initial stages of portland cement hydration at ambient temperature, by reaction of sulphate ions released by gypsum ($CaSO_4 \cdot 2H_2O$) with tricalcium aluminate ($Ca_3Al_2O_6$). After exhaustion of gypsum, the remaining tricalcium aluminate in solution reacts with already formed ettringite transforming to monosulphate ($Ca_4Al_2(SO_4)(OH)_{12} \cdot xH_2O$). At higher temperature (>100°C), ettringite is unstable and transforms to monosulphate. Monosulphates are known to exist as at least four different hydrate forms (x = 8,10, 12, 14).

In this study the stability of calcium sulphoaluminate hydrates were mapped in various environments (variable relative humidity, temperature and alkalinity). The monosulphate hydrates were obtained by hydrothermal synthesis using microwave radiation at 120°C. Their formation is via ettringite thermal decomposition in autoclave conditions under autogenous pressure. It has been shown that a series of calcium sulphoaluminate hydrates can be obtained depending on temperature and water activity. The interconversion of the calcium sulphoaluminate hydrates was found to be an easy and rapid process, whereby metastable phases are readily formed, indicating the lability of Ca-OH-Al-SO_4 system.

The kinetics and the mechanism of growth of calcium sulphoaluminate hydrates are known to influence the development of mechanical properties and the characteristics of cements. The ettringite crystal growth process was evaluated from the point of view of its influence on crystal morphology. General crystallisation methods for ettringite synthesis were developed starting from supersaturated solutions of pure phases and its morphology was found to vary with crystallisation factors (temperature for instance); ettringite crystals are generally hexagonal rods with different aspect ratios.

The morphology is also expected to produce changes in the rheological behaviour of cement slurry. Here, the contributions of the morphology of the early hydration products were related to the evolution of this early time rheology. More specifically, the shear viscosity of ettringite rod suspensions has been investigated experimentally to explore the role of size, shape, size distribution and particle volume fraction. It was found that an ettringite suspension is a complex system and displays a rheology that has been interpreted semi-quantitatively using well-established rheological models and principles. This work shows how an ettringite-dominated suspension will behave as the rods nucleate and grow, and to some extent even aggregate.

Acknowledgements

A great challenge has been to work with Prof. Chris Hall at Edinburgh University. I owe him a great debt for teaching me how to, and sometimes how not to, do research. His confidence in my work was very supportive and encouraged me to strive to become a good scientist. I always had the freedom to follow my own ideas which I am very grateful for. His enthusiasm and openness to new ideas and uncompromising faith in people have been qualities I wish I would inherit.

I take this opportunity to say a sincere 'thank you' to Nic Meller for her constant support extended over my work and my personal welfare. Part of my knowledge on X-ray Powder Diffraction, Synchrotron Energy Dispersive Diffraction and experimental techniques is the result of many discussions and our active collaboration. The quality of this manuscript has also improved substantially through her helpful advice.

I would like to thank Chris Jeffree who helped me to understand and perform the high-resolution Scanning Electon Microscopy investigations. Thank goes to Laurianne Robinet for sharing with me some of the 'secrets' of Raman spectroscopy. In particular, I enjoyed provoking discussions with Vasileios Koutsos, it helped me to step back and to get a different perspective on the problems.

I have been fortunate to have full support of Schlumberger Cambridge Research Center, both financially and technically. Special thanks goes to Geoff Maitland for valuable discussions and comments on the rheology work. I am much obliged to Valerie Anderson and Jonathan Phipps who initiated me in this intriguing subject. John Crawshaw and Gerry Meeten from SCR are acknowledged for stimulating discussions.

I would like to thank all my colleagues at the Center for Materials Science and Engineering and at the Institute of Materials and Processes for the good times we shared, not only in the office but also in our free time. I am very grateful to my Romanian friends for their affection, encouragement and loyalty whenever needed.

A special gratitude goes to my parents and my brother for a lifetime of love and support. Last but not least I would like to thank 'my other half' Marc for always believing in me.

Contents

. ii
Declaration of originality iv
Acknowledgements v
Contents vi
List of figures viii
List of tables xiii
Glossary xiv

1 General Introduction **1**

2 Sulphate AFm hydrates microwave-assisted chemistry and their stability at various relative humidities **4**
2.1 Introduction 4
2.2 Conditions for the formation and stability of monosulphate 6
2.2.1 Formation and stability in pure systems and in cements 6
2.2.2 Structure and morphology of monosulphate 7
2.3 Microwave heating 11
2.3.1 Phenomenon at molecular level 11
2.3.2 Aqueous systems and microwave radiation 13
2.4 Preparation and analysis of samples 14
2.4.1 Microwave-hydrothermal method 14
2.4.2 Conventional oven method 15
2.4.3 Monosulphate synthesis and characterization 15
2.4.4 Stability involving various relative humidities and temperature 16
2.5 Results and discussion 20
2.5.1 Conventional heating 20
2.5.2 Microwave heating 23
2.5.3 Stability of monosulphate hydrate 29
2.6 Conclusions 33

3 Calcium sulphoaluminate hydrates: a synchrotron diffraction study up to 150°C and reversion on cooling **35**
3.1 Introduction 35
3.2 The Synchrotron and in situ energy-dispersive diffraction 40
3.3 Experimental 42
3.3.1 Station 16.4 42
3.3.2 Chemistry 43
3.3.3 Procedure 43
3.4 Results and discussion 45
3.4.1 Direct synthesis of calcium alumino-monosulphate hydrate 47
3.4.2 Thermal stability of ettringite in alkaline solutions up to 150°C 50
3.5 Conclusions 59

4 Crystal growth from solution of ettringite **61**
4.1 Introduction 61
4.2 Theoretical aspects on crystal growth from solution 63
4.3 Experimental details 70
4.4 Results and discussions 73
4.4.1 Crystallization by solution cooling 73
4.4.2 Crystallization by solvent evaporation 84
4.5 Conclusions 91

5 Flow properties of freshly prepared ettringite suspensions in water **92**
5.1 Introduction 92
5.2 Experimental 94
5.2.1 Preparation of ettringite suspensions 94
5.2.2 Scanning Electron Microscopy of ettringite suspensions 95
5.2.3 Rheological characterization 95
5.2.4 Review of particulate suspensions rheology; fundamental concepts: $\dot{\gamma}\ \tau\ \eta$ 96
5.2.5 Rheological models 99
5.2.6 Dependence on particle shape and concentration 100
5.3 Results and discussion 103
5.3.1 Ettringite particle characteristics 103
5.3.2 Flow curves of ettringite suspensions 106
5.3.3 Comparison with models 110
5.4 Conclusions 113
5.5 Significance of the ettringite flow behaviour for cement slurry rheology 114

6 Conclusions and future work **116**
6.1 Synthesis of calcium aluminosulphates: reactions, stoichiometry, analysis of products, stability 116
6.2 Ettringite crystal growth 120
6.3 Ettringite rheology 120

Bibliography **122**

A Phase relations in CaO - Al_2O_3 - $CaSO_4$ - H_2O system **135**

B Experimental crystal growth study **140**

C Mineralogical model of the early cement hydration. **141**

List of figures

2.1 (a) Irregular crystalline platelets of monosulphate observed by Meredith [90] during the hydration of tricalcium aluminate (C_3A) in the presence of 25% gypsum. (b) Hexagonal, lamellar crystals of monosulphate observed by Locher [83] during cement hydration. 9

2.2 (a) General view of monosulphate 12-hydrate structure as determined by Allman (1968) [1]. Structure visualisation and the exploration of crystal packing was carried out using Mercury 1.4 [143] (b) The main layer composition. Projection on [001] plane. 10

2.3 Definition of phase difference and its relation to ε', ε'' and ε^*, [144] 12

2.4 (a) Holder containing a monosulphate sample rehydrated at 100% r.h.. A mylar window film of 3μm of thickness was fixed with double sided sticky tape on the sample holder in order to maintain the r.h. constant. The cavity of the sample holder is 1.5cm in length, 1cm wide and 0.1cm in depth. (b) Photograph showing diffractometer set-up used for rehydration experiments. An Anton Parr TTK450 heating/cooling stage is used to examine the effects of changes in temperature in-situ from -190°C to +450°C. Samples can be heated in air or vacuum. 18

2.5 Focusing diagrams on Bruker AXS D8 diffractometer [142]: (a) conventional para-focusing Bragg-Brentano geometry, (b) parallel-beam geometry using a parabolic mirror in the incident beam path. 19

2.6 XRD (blue pattern) and EDD (red pattern) spectra illustrating formation of monosulphate accommodating twelve water molecules. Green sticks denote ICDD pattern for 12-water monosulphate (Card No. 45-158). The sample was synthesized at 125 °C $\pm$ 4 for 19h, by means of conventional heating method. . 21

2.7 X-ray spectra illustrating formation of monosulphate. Green, red and pink sticks denote ICDD patterns for 12-water monosulphate (Card No. 45-158), ettringite (Card No. 41-1451) and calcite (Card No. 05-0586). 22

2.8 Comparative diffraction patterns of monosulphate showing positions of peaks relative to ICDD patterns for 14-hydrate, 12-hydrate monosulphate and corundum. Bottom pattern represent the sample as-synthesized and the others represent patterns of samples obtained from different synthesis. The duration of the synthesis was 9h for all samples. Green, blue and red sticks denote 14-hydrate, 12-hydrate monosulphate and corundum. Corundum was added as internal standard (mixed with the sample in a known proportion) in the last sample to confirm accurate peak positions. Key: ms12 = $C_4A\overline{S}H_{12}$, ms14 = $C_4A\overline{S}H_{14}$ 24

2.9 Contour plot of several XRD scans illustrating mineralogical changes through time. Scans were collected on samples with synthesis times from 1 to 9h, 2 weeks after they were conditioned over silica gel desiccant beds with r.h. between 13 - 40%. Key: ms12 = $C_4A\overline{S}H_{12}$, ms14 = $C_4A\overline{S}H_{14}$, e = $C_6A\overline{S}_3H_{32}$ 27

2.10 Contour plot of several XRD scans illustrating mineralogical changes through time. Scans were collected on the same samples as in figure 2.9, which were conditioned at the same r.h. for another 2 weeks. Corundum was added as internal standard for accurate identification of peak position. Key: ms12 = $C_4A\bar{S}H_{12}$, ms14 = $C_4A\bar{S}H_{14}$, e = $C_6A\bar{S}_3H_{32}$, c = Al_2O_3 28
2.11 Contour plot of several XRD scans illustrating mineral changes as function of r.h.. All range of r.h. was covered as in Table 2.1. Additional samples were also vacuumed. The starting material was 14-hydrate still wet with the mother liquor. Key: as in Fig. 2.10, ms10 = $C_4A\bar{S}H_{10}$ 30
2.12 Contour plot of several XRD scans illustrating mineral changes as function of r.h.. The sample was dry material previously conditioned on silica desiccant beds with r.h. 30%. 31
2.13 (a) Contour plot of several XRD scans illustrating monosulphate 12-hydrate dehydration as function of temperature. The temperature was ramped from 25 to 150°C. Two main transformations are observed at 40 and 100°C when conversion to 10 and 8-hydrate monosulphate occurs. (b) Plot of d-spacing changes versus water loss. 32
2.14 Contour plot of several XRD scans illustrating monosulphate 12-hydrate rehydration to 14-hydrate as function of temperature. The temperature was ramped from 25 to 150 °C. The transformation occurs at 60°C. 33

3.1 Schematic diagram of the 3-element detector at Station 16.4 [95]. 42
3.2 (a) Autoclave cell machined from polymer polyetheretherketone (PEEK) (b) The Schlumberger furnace used for reactions under hydrothermal conditions. . 44
3.3 Representation of the principle of EDD experiment operating with an autoclave hydration cell. Furnace main features are also showed: heating element, fan, thermocouple and PEEK cell [27]. 45
3.4 $C\bar{S}H_2$ patterns collected from top, middle and bottom detectors to optimize the calibration. The detectors were positioned at 2θ angles: 1.788, 4.554 and 7.477°, respectively. Tick marks in red represent characteristic reflections for gypsum according to ICDD. 46
3.5 Thermal synthesis of AFm. Synchrotron diffraction patterns illustrating mineral changes over 6 h. 180 patterns were collected at 2 min interval as the temperature was ramped from 30 to 150°C at 2°min^{-1} and then the sample was naturally cooled to ambient temperature. These patterns are collected by the middle detector (2θ = 4.554°). Here every 5th successive pattern is shown. Key: o = peek polymer cell; **e** = $C_6A\bar{S}_3H_{32}$; **g** = $C\bar{S}H_2$; ms-14 = $C_4A\bar{S}H_n$; b = $C\bar{S}H_{0.5}$. 48
3.6 Plot of overlapping ettringite (100) (1/d 1.028 nm^{-1}) and monosulphate (003) (1/d 1.0471 nm^{-1}) over the temperature interval from 30 to 150°C and reverse on cooling to ambient temperature. The peak at 1/d 1.310 nm^{-1} is the 020 gypsum reflexion. These peaks are collected by the detector set at the lowest angle (2θ = 1.788°). Key: e = $C_6A\bar{S}_3H_{32}$; g = $C\bar{S}H_2$; ms-14 = $C_4A\bar{S}H_n$. 49

3.7 Ettringite thermostability in 0.5 M NaOH. Synchrotron diffraction patterns illustrating mineral changes over 2 h. 62 patterns were collected at 2 min interval as the temperature was ramped from 30 to 150°C at 1°min^{-1}. Here every 3rd successive pattern is shown. Key: o = peek polymer cell; p = CH; g = $C\bar{S}H_2$; ms-14 = $C_4A\bar{S}H_n$; h = C_3AH_6. 51
3.8 Expanded plot; ettringite thermostability in 0.5 M NaOH. Key: o = peek polymer cell; p = CH; g = $C\bar{S}H_2$; ms-14 = $C_4A\bar{S}H_n$; h = C_3AH_6. 53
3.9 Peak areas over time and increasing temperature showing gypsum (-221) (1/d 3.489 nm^{-1}) (□) , potlandite (101) (1/d 3.805 nm^{-1}) (△), ettringite (104) (1/d 2.132 nm^{-1})(×) and ms14 (006) (1/d 2.092 nm^{-1}) (+). 54
3.10 Ettringite synthesis at 150°C in 1 M NaOH. For reason of clarity, only one in every three diffraction patterns is shown. The experiment was ramped over 2 h and held for 5 min at the final temperature. 62 patterns were collected, one every 2 min. Key: o = peek polymer cell; p = CH; g = $C\bar{S}H_2$; ms-14 = $C_4A\bar{S}H_n$; h = C_3AH_6; u-ph = $C_4A\bar{S}_{1.5}N_{0.5}H_{15}$. 56
3.11 Expanded plot of ettringite synthesis at 150°C in 1 M NaOH. Key: o = peek polymer cell; p = CH; g = $C\bar{S}H_2$; ms-14 = $C_4A\bar{S}H_n$; h = C_3AH_6; u-ph = $C_4A\bar{S}_{1.5}N_{0.5}H_{15}$. 57
3.12 Main peak areas over time and increasing temperature from 30 to 150°C. Areas of AFt (104) (1/d 2.132 nm^{-1}) (× red), AFm (006) (1/d 2.092 nm^{-1}) (+), C_3AH_6 (211) (1/d 1.948 nm^{-1})(◁), CH (001) (1/d 2.029 nm^{-1})(△), $C\bar{S}H_2$ (-221) (1/d 3.481 nm^{-1}) (□) and 'U - phase'(103) (1/d 2.243 nm^{-1})(× black). . 58

4.1 Main stages of crystal formation from solution. 63
4.2 The solubility-supersolubility diagram 65
4.3 Incorporation of crystal forming elements on the surface of a growing crystal. . 67
4.4 Film model for crystal growth. 68
4.5 A three-dimensional crystal showing K, S, and F faces [63]. 70
4.6 (a) Synthetic ettringite grown in solution, showing needle-like morphology. (b) Fractured core co-existing with gypsum impurity. 75
4.7 (a) SEM of one single ettringite entity showing hexagonal cross-section. (b) Crystal structure of ettringite, showing columns whose empirical composition is $[Ca_3Al(OH)_6 \cdot 12H_2O]_2^{3+}$] and channel sites occupied by sulphate ions and water. 76
4.8 Indication of an internal structure of fibrils in the ettringite rods. 77
4.9 (a) Ettringite rods exhibiting a radial arrangement. (b) SEM micrograph of a ettringite core grown by solution cooling. 78
4.10 (a) SEM micrograph showing the existence of unstructured material as part of the core. (b) Large crystallite fractured with ragged ends. 79
4.11 Temperature dependence of the supernatant concentration prepared by mixing reactant solutions. Concentrations of aluminium, calcium and sulphate are shown as follows: Al^{3+} (•), Ca^{2+} (∗), $SO_4{}^{2-}$ (×). Equilibrium concentrations (at saturation) of aluminium, calcium and sulphate as determined by Perkins [108] in temperature-dependent ettringite dissolution experiments, are also shown: Al^{3+} (▲), Ca^{2+} (■), $SO_4{}^{2-}$ (♦). The area highlighted in pink represent the solubility line (in red) in the solubility-supersolubility diagram Fig. 4.2. 82

4.12 Representation of the time variation of conductivity of the supernatant. The conductivity is shown for two samples where the supernatant was withdrawn from the reactants mixture at 1 (×) and 20min (•). The change in solution conductivity indicates an induction time equal to zero at the time when first measurement was taken. The nucleation process appears to cease after ~3 days. 83
4.13 (a) SEM of ettringite obtained at ambient temperature by evaporation method showing a six-sided morphology. (b) Crystals have an average in length of ~60μm. 85
4.14 (a) and (b) Short ettringite crystals exhibiting a radial habit. 86
4.15 (a) Raman spectra of two areas on the sample compared with a gypsum reference specimen, (R). Strong peak is observed at 1006.7 cm^{-1} corresponding to the vibration of the SO_4^{2-} species. (b) Image of the precipitate obtained by evaporation of a supernatant having as a source synthetic ettringite, showing areas which were subject of investigation. 88
4.16 Raman spectra showing strong peak at 1086.6 cm^{-1} corresponding to the vibration of the CO_3^{2-} species. The area investigated is marked in Fig. 4.15b. . . 89
4.17 Compositional map of the precipitate obtained by ettringite supernatant evaporation at ambient temperature. (a) Image of the spot investigated. (b) OK. (c) SK. (d) CK. (e) CaK. (f) AlK. 90

5.1 (a) CVO rheometer (Bohlin Instruments) fitted with coaxial cylinder geometry (roughened cup and bob and double gap). (b) Experimental set-up showing a transparent cup used to observe the flow and determine the optimal shear rate at which dilute systems sedimentation is prevented. (c) Representation of the principle of the coaxial cylinder rheometer working on controlled shear mode. Torque/shear rate is measured on the rotor axis. Outer cylinder is stationary. (d) Flow pattern in a rotational rheometer/viscosimeter, describing a laminar (steady) and one dimensional flow. 97
5.2 Typical rheograms encountered in fluids; a - plastic (showing flow above a yield stress, corresponding to the transition from elastic to plastic deformation) b - pseudoplastic (shear thinning), c - shear thickening, d - Newtonian. 99
5.3 (a) Sketch showing highly entangled rods, where due to constraints the rod diffuse only in the direction of its own axis, changing its direction gradually. (b) Comparative SEM micrograph showing, in the same manner, ettringite needle strongly entangled. The structures were grown, in the present study, for a solid volume fraction, $\phi = 0.05$. 102
5.4 (a) Scanning electron micrograph of fresh ettringite grown for a solid volume fraction, $\phi = 0.03$. (b) Hexagonal cross-section of an ettringite crystal grown by cooling from a supernatant with low supersaturation. 104
5.5 Cumulative frequency plot showing a median value $r_i = 8.4$. A sample of n = 30 particles was measured. 105
5.6 Shear viscosity of rod-like ettringite suspensions dependence on different solids content as a function of the shear rate applied. Suspensions at nine volume fractions from 0.01 to 0.08 are shown as follows: 0.01 (•), 0.02 (□), 0.025 (♦), 0.03 (×), 0.04 (○), 0.05 (■), 0.06 (◁), 0.07 (▲), 0.08 (+). 106

5.7 Shear stress versus shear rate over a range of different solid contents, compared with the predictions of Ostwald-de Waele, equation 5.3. The ettringite data are shown for volume fractions of 0.01 (•), 0.02 (□), 0.03 (×), 0.04 (○), 0.05 (■), 0.06 (◁), 0.07 (▲), 0.08 (+). The drawn lines are the Ostwald-de Waele fits. The fit-parameters are listed in Table 5.1. 107

5.8 Cross-model describing ettringite suspensions flow with asymptotic viscosities at zero and infinite shear rates. Solid volume fractions: 0.01 (•), 0.02 (□), 0.03 (×), 0.04 (○), 0.05 (■), 0.06 (◁), 0.08 (+). Dashed lines represent the Cross model fit with the infinite shear viscosity fixed at $\eta_\infty = \eta_0/0.85r_i$ and m = 1.5. The solid curve shows an alternative fit for the highest concentration suspension with m = 1.15 and $\eta_\infty = \eta_0/4r_i$. 109

5.9 Relative low shear viscosity, $\eta_{20s^{-1}}/\eta_{H_2O}$, as a function of ettringite rod volume fraction. The line has a slope of approximately 3000, far in excess of $[\eta] \sim 10$ for rods of this aspect ratio. The value of η_{H_2O} at 25°C was taken to be 0.89 mPa s. 111

5.10 Shear viscosity of ettringite rods suspensions as a function of the particle volume fraction for a shear rate of $20s^{-1}$. 112

6.1 Schematic representation of monosulphate stability derived from the data such as those presented in Chapter 2. The stability map of monosulphate was built for relative humidities from 10 to 100% and temperatures up to 150°C. Key: ms(x) = calcium aluminium monosulphate hydrate ($C_4A\overline{S}H_n$), where x = n = 8, 10, 12, 14 denote the number of water molecules present in the sample, RH = relative humidity. 117

6.2 Summary of the stable phase assemblages identified for up to 150°C and 1M NaOH. The temperature and time markings are included to give an indication of when each event occurs. Key: CH = Portlandite/$Ca(OH)_2$, AFt = Ettringite/ $Ca_6[Al(OH)_6]_2(SO_4)_3 \cdot 26H_2O$, $C\overline{S}H_2$ = Gypsum/$CaSO_4 \cdot 2H_2O$, AFm = Monosulphate/$Ca_4[Al(OH)_6]_2SO_4 \cdot xH_2O$, C_3AH_6 = Hydrogarnet/$3CaO \cdot Al_2O_3 \cdot 6H_2O$, U-phase = $NaCa_4Al_2O_6(SO_4)_{1.5} \cdot 15H_2O$ 119

A.1 Phase relations in the system CaO - Al_2O_3 - $CaSO_4$ - H_2O at **(a)** 25°C and **(b)** 50°C (according to Atkins and Glasser [3]) 136

A.2 Phase relations in the system CaO - Al_2O_3 - $CaSO_4$ - H_2O at 80°C (according to Atkins and Glasser [3]) 137

C.1 Summary of the early cement hydration according to Locher [83] 141

List of tables

2.1 Selected relative humidities and corresponding salt in water solutions [58]. . . . 17

3.1 Reagents and proportions used in EDD experiments. The experiment no.1 represents the control sample, which will be subsequently used to optimize the calibration data file. For this purpose an anhydrous sample of gypsum will be used. The following experiments investigate monosulphate and ettringite stability as proposed above. 43

3.2 Phase assemblages identified in the CaO - Al_2O_3 - $CaSO_4$ - H_2O system using Synchrotron energy dispersive diffraction method. 60

5.1 Best fit parameters 108

5.2 Best fit parameters of Cross model for m = 1.5 and $\eta_\infty = \eta_0/0.85r_i$ 109

5.3 Absolute viscosities determined at $20s^{-1}$ 110

A.1 Pseudo-invariant point aqueous compositions in the CH saturated region of the CaO - Al_2O_3 - $CaSO_4$ - H_2O system, as function of temperature and alkali content (from Glasser et al. [30, 31]). Concentrations are given in mM/L. . . . 138

A.2 Phase assemblage the system CaO - Al_2O_3 - $CaSO_4$ - H_2O at 25°C. Predictions of Clark and Brown [23] calculated using PhreeqC based on solubility products values (k_{sp}) reported by Damidot and Glasser [31]. SI = 0.0 indicates saturation while a negative value indicates undersaturation. 139

B.1 Concentration of the main species in the supernatant determined by ICP-AES in the crystallization by evaporation experiment. All concentration are expressed in mmol/L. The analytical precision is considered to be better than 1%. 140

B.2 Concentration of the main species in the supernatant determined by ICP-AES in the crystallization by cooling experiment. All concentration are expressed in mmol/L. The analytical precision is considered to be better than 1%. 140

Glossary

General cement nomenclature:

TLA	Three letter acronym
OPC	ordinary portland cement
C: Calcium oxide	CaO
A: Alumina	Al_2O_3
$\overline{S}$: Sulphate	SO_3
AH: Aluminium hydroxide	$Al(OH)_3$
$C\overline{S}H_2$: Gypsum	$CaSO_4{\cdot}2H_2O$
$C\overline{S}H_{0.5}$: Bassanite	$CaSO_4{\cdot}0.5H_2O$
CH: Calcium hydroxide/Portlandite	$Ca(OH)_2$
C_3AH_6: Hydrogarnet	$3CaO{\cdot}Al_2O_3{\cdot}6H_2O$
H: Water	H_2O
C_3A: Tricalcium aluminate	$3CaO{\cdot}Al_2O_3$
C_4AF: Tetracalcium aluminoferrite/Brownmillerite	$4CaO{\cdot}Al_2O_3{\cdot}\ Fe_2O_3$
$C_6A\overline{S}_3H_{32}$: Ettringite/(AFt)	$Ca_6[Al(OH)_6]_2(SO_4)_3{\cdot}26H_2O$
$C_4A\overline{S}H_n$: Monosulphate/(AFm)	$Ca_4[Al(OH)_6]_2SO_4{\cdot}xH_2O$
$C_4A\overline{S}_{1.5}N_{0.5}H_{15}$: U-phase	$NaCa_4Al_2O_6(SO_4)_{1.5}{\cdot}15H_2O$

Other shortenings:

SEM	Scanning Electron Microscope
FEG-SEM	Field Emission Gun Scanning Electron Microscope
XRD	X-ray Powder Diffraction
EDD	Energy Dispersive Diffraction
ICP-AES	Inductively Coupled Plasma Atomic Emission Spectroscopy
RS	Raman Spectroscopy

Glossary of terms:

Aggregates: are chemically inert, solid bodies held together by the cement (vermiculite, ceramic spheres, perlite, expanded clay, sand, crushed recycled concrete, river gravel, steel or iron pellets, etc.).

Cement: is a finely pulverized material which by itself is not a binder, but develops the binding property as a result of hydration (i.e., from chemical reactions between cement minerals and water). A cement is called **hydraulic** when the hydration products are stable in aqueous environment. The most commonly used hydraulic cement for making concrete is **portland cement**.

Cement hydration: is as sequence of chemical reactions between cement minerals and water, leading to setting and hardening of the cement-water mixtures.

Cement paste: Constituent of concrete consisting of cement and water.

Colloid: a mixture with properties between those of a solution and fine suspension.

Colloidal suspension: a colloid that has a continuous liquid phase in which a solid is suspended in a liquid.

Concrete: is a composite material-synthetic rock that consists of a binding medium (cement paste) within which are embedded particles or fragments of aggregates.

Flash set: the rapid development of rigidity in a mixed portland cement paste, mortar or concrete usually with the evolution of considerable heat. When little or no gypsum was added to a ground portland cement clinker, the hydration of tricalcium aluminate (C_3A) is rapid and and the hexagonal-plate calcium aluminate hydrates starts forming in large amounts soon after the addition of water, causing almost an instantaneous set. Rigidity cannot be dispelled nor can the fluidity be regained by further mixing without addition of water.

Ionic strength: the weight concentration of ions in solution, calculated by multiplying the concentration of each ion in the solution (C) by the corresponding square of the charge on the ion (z) summing this product for all ions in the solution and dividing by 2, ($I=0.5\sum(z^2 \times C)$).

Laminar flow: flow without turbulence.

Newtonian: flow model of fluids in which a linear relationship exists between shear stress and shear rate, where the coefficient of viscosity is the constant of proportionality.

Non-Newtonian: any laminar flow that is not characterized by a linear relationship between shear stress and shear rate .

Placeable concrete: how easily fresh concrete can be placed and consolidated in forms.

Portland cement clinker: is produced by heating the ground raw materials in a rotating kiln to 1450°C. It is ground to a fine powder and mixed with a few wt% gypsum to make portland cement.

Raw mix: consists of limestone, clay, bauxite, iron ore and quartz.

Shear-thinning (pseudoplastic): a decrease in viscosity with increasing shear rate during steady shear flow.

Solubility: the maximum equilibrium amount of solute which can normally dissolve per amount of solvent (or solution) is the solubility of that solute in that solvent.

Structure: in rheology, structure is a term that refers to the formation of stable physical bonds between particles (or chemical bonds between macromolecules) in a fluid. These bonds result in aggregate, floc, or network structure, which impacts the rheological behavior of the fluid and provides elastic and plastic properties.

Supernatant: is the liquid, containing soluble compounds, that is left behind after a mixture is precipitated.

Supersaturation: refers to a solution that contains more of the dissolved material than could be dissolved by the solvent under normal circumstances.

Viscosity: the tendency of a liquid to resist flow as a result of internal friction. During viscous flow, mechanical energy is dissipated as heat and the stress that develops depends on the rate of deformation.

Chapter 1
General Introduction

A gain in knowledge on calcium sulphoaluminate hydrates formation, their stability and flow properties assumes a central role in this work. The sulphoaluminate hydrates are important components of portland cement and constitute the principal matrix formers of some sulphoaluminate cements [131]. These phases are responsible for the setting behaviour of cement [51] and affect the hardening process at later stages of hydration.

The two complex salts of target interest in this study are calcium aluminate trisulphate hydrate and calcium aluminate monosulphate hydrate, commonly referred in cement literature to as ettringite (AFt) and monosulphate (AFm).

Ettringite ($C_6A\overline{S}_3H_{32}$) is formed during the initial stages of portland cement hydration at ambient temperature, by the reaction of sulphate ions released by gypsum ($C\overline{S}H_2$) with tricalcium aluminate (C_3A). After exhaustion of gypsum, the remaining C_3A in solution reacts with already formed ettringite transforming to monosulphate ($C_4A\overline{S}H_n$, where n=14). At elevated temperatures, T >100°C, ettringite is unstable and decomposes to monosulphate.

Monosulphates are known to exist as at least four different hydrate forms [76]. However, as with many compounds encountered in cement chemistry, the water content of the monosulphate hydrate is not always definite. One of the main handicaps is the difficulty in stabilizing the water content during characterization, particularly of the higher hydrate forms (n>12).

Monosulphate in its pure state remains difficult to synthesize. Since the pioneering work of Lerch [80] on monosulphate, revisited by Berman, in 1963, to determine its heat of formation [15], it has largely been ignored. The preparation methods of monosulphate mainly result from solving the equilibrium diagrams in C-$\overline{S}$-A-H system at different temperatures. However, current synthesis methods are restricted by an extremely long reaction time and small yield.

The importance of the calcium sulphoaluminate hydrate stability to cement hydration has been long established [32, 68, 69]. Up to now, most of the publications dealing with the stability of ettringite and monosulphate generally refer to ex-situ experiments where the temperature and

alkali effects were evaluated independently. Hence, combined effects of those two parameters has to be investigated specifically.

The kinetics and the mechanism of the formation of calcium sulphoaluminate hydrates are believed to influence the development of mechanical properties [64] and the characteristics of cement. The morphology of the calcium sulphoaluminate hydrates for different crystal growth conditions is still not a well-resolved question. Most of the studies on the mechanism of ettringite formation were focused to explain the expansion characteristics of expansive cements and lack a common opinion about the mechanism. Therefore, knowledge on the mechanism of crystal growth and its influence on ettringite crystal morphology, are required.

Ettringite formed in cement/water systems is one of the earliest products and therefore it is likely that the ettringite plays an important role in determining the rheology of cement at early times. Hence, the morphology is expected to produce changes in the rheological behaviour of cement.

This thesis is organized as follows. In Chapter 2 a novel method to synthesize pure phase of monosulphate, based on microwave heating, is reported. Further, the stability of the monosulphate hydrates, in various relative humidity environments, was investigated using powder X-ray diffraction (XRD) and complemented by energy dispersive diffraction (EDD).

In Chapter 3 the combined effects of temperature and alkali on the stability of ettringite and monosulphate were studied using synchrotron energy dispersive diffraction (EDD). This chapter is divided into two parts. The first one deals with in-situ synthesis of monosulphate, to solve any uncertainties regarding the reaction products and their stability on cooling from elevated temperatures, as emerged from Chapter 2, whereas the second part is concerned with the alkali influence on ettringite thermal decomposition to ascertain thermodynamic predictions of Damidot and Glasser on hydrate phase stability [30, 31], in analogous conditions.

In Chapter 4 the ettringite crystal growth process from solution was evaluated from the point of view of its influence on crystal morphology. Two different experimental directions were taken whereby the supersaturation of the mother liquor was induced either by cooling or solvent evaporation. These directions were chosen to be sympathetic to the growing conditions of ettringite in the cement systems. Some aspects of nucleation and growth processes are also summarized in this chapter with emphasis on the theories of crystal growth from solution and on the two main mechanisms that govern crystal growth.

The dependence of shear viscosity of ettringite rod suspensions on size and shapes distributions and particle volume fraction is investigated in Chapter 5. This chapter describes the preparation structure of ettringite suspensions, their rheological characterization and a comparison of this with models developed for rod-like colloids.

Chapter 2
Sulphate AFm hydrates microwave-assisted chemistry and their stability at various relative humidities

In this chapter, microwave radiation is successfully used to provide a novel synthesis method for monosulphate hydrate. The stability of the monosulphate hydrates, in various environments are investigated using powder X-ray diffraction (XRD).

2.1 Introduction

The behaviour of the sulphoaluminates of calcium is of special interest to the cement industry, their stability being directly related to the physical and mechanical properties of portland cements (fluidity, setting time, initial strength development, etc.) as well as corresponding mortars and concrete. These phases are responsible for the setting behaviour of the cement and affect the hardening process at later stages of hydration [51].

The crystalline monosulphoaluminate of calcium hydrate is one of the two complex salts that are formed during cement hydration. In construction or oil well cements, hydrated calcium aluminate sulphates form from calcium aluminate phase (C_3A, C_4AF)[1] and a sulphate source such as gypsum ($C\overline{S}H_2$) [89]. Depending on the concentration of aluminate and sulphate ions in the solution, the precipitating crystalline product is either calcium aluminate trisulphate hydrate (AFt) or the calcium aluminate monosulphate hydrate (AFm) [80]. In saturated solutions with respect to calcium and hydroxyl ions, the former crystallizes as prismatic needles in a columnar like structure and is referred to as high-sulphate hydrate or ettringite. The monosulphate, a trivial name of the low-sulphate form, crystallizes as hexagonal plates.

[1]Cement nomenclature will be used throughout, see Glossary.

The relevant chemical reactions may be written as:

$$2[AlO_4]^- + 3[SO_4]^{2-} + 6[Ca]^{2+} + 32 \cdot H_2O(aq.) \Rightarrow C_6A\overline{S}_3H_{32}(AFt) \quad (2.1)$$

$$2[AlO_4]^- + [SO_4]^{2-} + 4[Ca]^{2+} + 32 \cdot H_2O(aq.) \Rightarrow C_4A\overline{S}H_n(AFm) \quad (2.2)$$

where n is variable n = 10, 12, 14, etc. Within minutes of cement hydration, ettringite is usually the first hydrate to crystallize because of the high $[SO_4]^{2-}$ to $[AlO_4]^-$ ratio in the solution phase. Later, when all the free sulphate is consumed, ettringite reacts with remaining calcium aluminate to form monosulphate. AFm forms in addition at temperature above 70°C in preference to ettringite (AFt), [101]. An insufficient supply of sulphate ions causes the reactive calcium aluminate phase to convert to monosulphate instead of ettringite, which negatively affects the fluidity of the cement paste [102]. The presence of monosulphate is thought to be the cause for rapid stiffening (flash set) [83].

However, there are controversial findings with regard to the influence of sulphates on calcium aluminate phases dissolution. Although the hydration products of C_3A and C_4AF depend on the quantity of $[SO_4]^{2-}$ in solution, the amount of calcium aluminate dissolution does not change, according to Odler and Locher [83, 102]. Nevertheless the rheological changes due to the addition of calcium sulphate could not be related to an excessive C_3A and C_4AF hydration, but only to the different hydrates formed.

Monosulphate in its pure state remains difficult to synthesize. Since the work of Lerch [80] on monosulphate, revisited by Berman, in 1963, to determine its heat of formation [15], it has largely been ignored. Experimentally in laboratory conditions, monosulphate 14-hydrate has been synthesized by hydrothermal decomposition of ettringite at 114°C using conventional heating methods [59]. Small impurities of bassanite were also found as a final product of ettringite decomposition. In dry conditions, ettringite is known to start decomposing at temperatures < 70°C and little or no monosulphate is formed, suggesting that the transformation, ettringite to monosulphate, requires environmental control.

The aim of the work described in the first part of this chapter is to provide a novel method to synthesize hydrated calcium aluminate sulphates (AFm)[2] based on non-conventional heating methods such as microwave heating. This method is increasingly used in material synthesis due

[2]In cement literature the terms AFm and AFt are employed to designate the products which may have variable chemical compositions but are structurally similar to monosulphate hydrate or ettringite, respectively.

to attractive properties of the microwaves. Any low molecular weight, dipolar solvent may be heated using microwave radiation. The use of polar starting materials and final products allow rapid, specific and controllable synthesis.

The second half of this chapter is devoted to sulphate AFm hydrates stability in various relative humidity environments. As with many compounds encountered in portland cement chemistry, the water content is not always definite. One of the main handicaps is the difficulty of stabilizing the water content during characterization, particularly of higher hydrate forms.

2.2 Conditions for the formation and stability of monosulphate

2.2.1 Formation and stability in pure systems and in cements

A tremendous amount of studies have been carried out on the equilibrium of solid hydrated phases in their mother liquor and on the direct observation of these phases by means of physico-chemical methods (X-ray powder diffraction, microscopy, infrared spectroscopy, differential calorimetry, etc.).

This has made possible identification of the calcium aluminate hydrates and solution of equilibrium diagrams in C - $\overline{S}$ - A - H system at different temperatures. The evolution of these phases within cements or in the presence of sulphates, carbonates and chlorides have been also investigated. The comprehensive study of Jones [69] and D'Ans and Eick [32] on the quaternary system C - C$\overline{S}$ - A - H, showed the equilibrium diagrams for two sets of products, a stable system in which the trisulphate is formed and a metastable system in which the monosulphate is formed. More recently, a thermodynamic approach was given by Damidot [31] to determine the variation of the system in presence of solutions having known compositions. This was in good agreement with Jones and D'Ans works, showing that at 25°C, monosulphoaluminate appears to be always a metastable phase with respect to ettringite or to C_3AH_6.

Nevertheless, during portland cement hydration, the transformation of ettringite to monosulphate at low sulphate concentrations, seems to disagree with the results of Damidot which predict the formation of C_3AH_6 instead of monosulphoaluminate (Fig. A.1). This was explained by the fact that, for the most part, the cement hydration does not take place under equilibrium conditions and the system is far more complicated (more additional ions in solution, presence of CO_2). Applying the ambient temperature methodology for elevated temperatures, Damidot

has evaluated the same system at 50°C and 80°C [30]. The results indicate that monosulphoaluminate becomes the stable phase at temperatures higher than 45°C, findings also reported by Ogawa and Roy [103] and Ghorab and Kishar [52].

The heat of formation of $C_4A\overline{S}H_{12}$ was determined by Berman [15] who also found it to be a metastable compound within certain limits of the concentration ratios of the various reacting ions. The minimum CaO/Al_2O_3 molar ratio is significant because a high OH^- concentration favours formation and longer persistence of monosulphate.

The pure phase of monosulphoaluminate is known to dissolve incongruently [2], with progressive precipitation of ettringite, confirming the relative thermodynamic stability for these two phases.

Studies on the mechanism of formation of crystalline hydrates in the system $C_4A_3\overline{S}$ - $C\overline{S}$ - C - H as reported by Hanic and Gabarisova [61] describe the monosulphoaluminate hydrate formation in a two-step reaction. The second step of the reaction is characterized by a first-order (one-way) reaction mechanism. The ettringite converts entirely to the monosulphate hydrate phase after one hour in boiling water as seen from X-ray diffraction patterns by Ghorab and Kishar [50]. The monosulphate remains stable with a further rise of the sulphate ion concentration and a decrease in the aluminium concentration in a solution with an average pH value of 11.6 after one week at 100°C. The stability of monosulphate hydrate is enhanced in alkaline environments where splitting of the sulphate free phase is favoured [51].

2.2.2 Structure and morphology of monosulphate

Mechanical properties of cements as well as corresponding mortars and hardened concrete are significantly affected by the formation of calcium aluminate hydrates [86]. The formation and the morphology of calcium sulphoaluminate hydrates are associated with key properties, such fluidity, setting time and initial strength development. At later stages, focus is placed on phenomena such as the disruption of hardened concrete (expansion) by sulphate attack, production of shrinkage-compensated and chemically prestressed concrete under restraining conditions.

AFm forms in cement pastes, but persists only in contact with solutions of much lower sulphate concentration than is required for stabilization of AFt. The implications of calcium aluminate hydrates on the initial fluidity of cement paste is described by Locher [83] in a mineralogical

model for C_3A hydration (Fig. C.1). In conditions of normal setting, C_3A is converted into ettringite and as long as the hydrates are not large enough to bridge the space between particles, the cement paste is still placeable. When there is an insufficient supply of sulfates, AFm is formed (Fig. C.1, case III and IV). In case III small amounts of ettringite are formed during the first seconds of hydration, after that the main phases are plate-like crystals of monosulphate or calcium aluminate hydrates. The new minerals formed have a negative influence on the rheological properties due to their morphology. AFm formation results in a stiff consistency which can no longer be improved.

The morphology of hydrates precipitated from undersaturated solutions with respect to $Ca(OH)_2$ and $CaSO_4$ is not similar to that of the hydrates formed in supersaturated solutions [80]. The hydrates in cements are formed normally under conditions of supersaturation. Replicating those conditions and by means of optical microscopy and scanning electron microscopy (SEM) Mehta [86] and recently Meredith [90] observed that the monosulphate hydrate has a plate-like morphology (Fig. 2.1) and ettringite is grown as short, stubby needles with thickness-length ratio of about 1:3. The AFt formed in unsaturated conditions present itself as long slender, needle-shaped crystals, hence, during its formation, ettringite may cause expansive stress on the confined space [60]. The AFm formation in a confined space may not lead to any expansive pressure on the restraining medium, because the stress caused by crystal formation is likely to be dissipated by the tendency of plate-like crystals to orientate themselves as 'leaves of a book' [86]. However, a reverse effect is expected from the short prismatic crystals of ettringite, which appear less sensitive to orientation in conditions of external stress constraint.

The morphology of monosulphate hydrate obtained by ettringite decomposition, at 130°C to 150°C in the range of 100psi to 600psi, in water was found to be different from that in a cement paste [103]. Pseuso-hexagonal outlines of monosulphate hydrate plates with many hexagonal holes were observed together with traces of crystal growth in the crystalline mass. AFm shows a layer structure in a plate-like morphology, as in clay minerals (Fig. 2.2a). The calcium monosulphate hydrate plates are hexagonal or pseudo-hexagonal and optically birefringent. The density is $1.90 g/cm^3$, as determined by Kuzel [76].

The calcium monosulphate hydrate was synthesized for the first time by Lerch, Ashton and Bogue [80]. In the pure phase, $C_4A\bar{S}H_{12}$ is difficult to obtain due to a tendency to form solid solution together with α-C_4AH_{13}.

(a) (b)

Figure 2.1: *(a) Irregular crystalline platelets of monosulphate observed by Meredith [90] during the hydration of tricalcium aluminate (C_3A) in the presence of 25% gypsum. (b) Hexagonal, lamellar crystals of monosulphate observed by Locher [83] during cement hydration.*

A considerable number of studies have dealt with the crystal structure investigation of the lamellar AFm [1, 76]. All of them report a layer structure, of the brucite type, for calcium monosulphate hydrate.

The structural determination from single crystal diffraction, performed by Allmann [1], yields the following lattice constants at 21°C: c_0=26.79Å and a_0=5.76Å. The space group is $R\bar{3}$. The main layer composition is described by $[Ca_2Al(OH)_6]^+$, with an Al-OH bond length of 1.905Å and respectively Ca-OH bond lengths of 2.36Å (3x) and 3.45Å (3x). This represents, the almost invariant 'vertebral column' of the AFm phases.

The three octahedral sites of the ordered brucite-like main layer are occupied by one Al and two Ca (Fig. 2.2b). The Ca atoms are shifted by 0.57Å in the [001] direction away from the center of their octahedron and approach an H_2O molecule of the interlayer by 2.51Å , therefore resulting is a 7-fold coordination for Ca. The rest of the interlayer consisting of $1/2SO_4^{2-}$, and $1H_2O$, is disordered. The SO_4^{2-} groups randomly occupy one of the two possible sites in every other cell (Fig. 2.2a). When it is missing, SO_4^{2-} is replaced by 2 molecules of water connected by the center of inversion. The water molecules adjacent to the Ca form a hydrogen-bond to the sulphate group: H_2O-O=2.37Å. The two types of layers are connected by hydrogen-bonds with O-O lengths higher than 2.74Å (Fig. 2.2b). The water of crystallization is bounded in the interlayer normal to the *c*-axis. This facilitate the dehydration properties of calcium aluminate monosulphates.

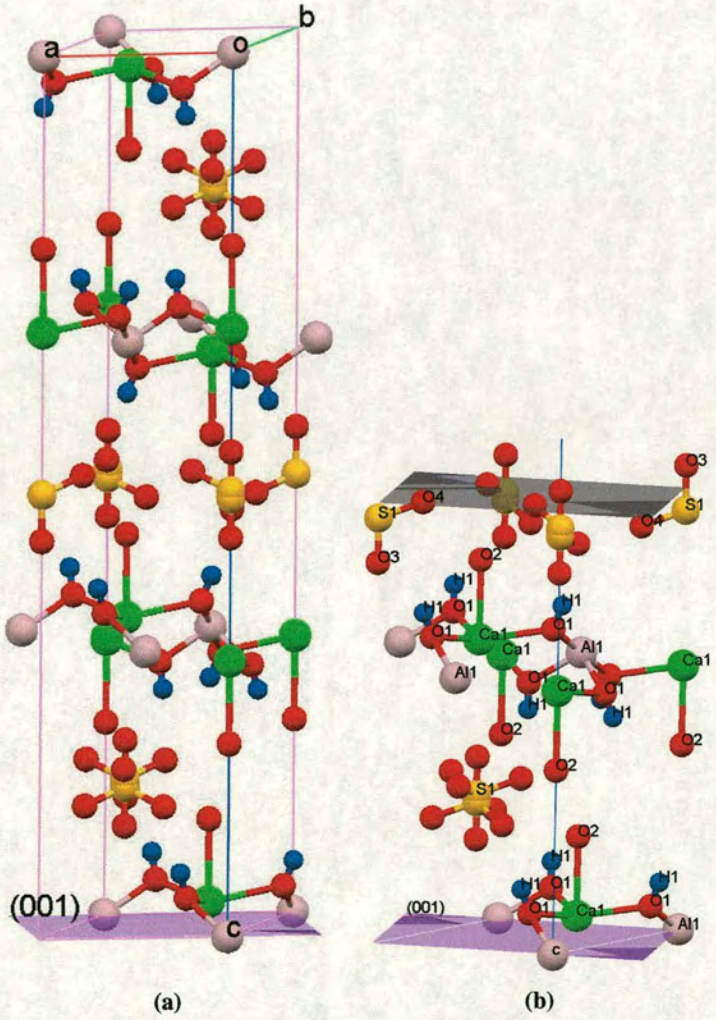

(a) (b)

Figure 2.2: *(a) General view of monosulphate 12-hydrate structure as determined by Allman (1968) [1]. Structure visualisation and the exploration of crystal packing was carried out using Mercury 1.4 [143] (b) The main layer composition. Projection on [001] plane.*

It has been found that for a relative humidity of 35 to 40%, its composition can be expressed as follow: $[Ca_2Al(OH)_6]^+ \cdot [1/2SO_4 \cdot 3H_2O]^-$ [76].

Calcium aluminate monosulphate does not form solid solutions with its homologue, calcium aluminate trisulphate hydrate. Instead, there is evidence of solid solution with its corresponding calcium ferrate hydrate [54].

2.3 Microwave heating

2.3.1 Phenomenon at molecular level

The electromagnetic spectrum is made of various regions, for example X-rays, ultraviolet and infra-red region. The region between the infra-red and radio wave is known as the microwave region. Microwave radiation has wavelengths between 1μm and 1m, and frequencies between 30 and 0.3GHz [47]. Generally the electromagnetic waves consist of two components, the magnetic and the electric fields, which are orthogonal [71]. Materials can be heated with high frequency waves, such heating being entirely due to the electric field component. The electric field component is responsible for the dielectric heating via two mechanisms [92]:

1. Conduction mechanism; if there are charged particles present in the sample that can move freely through the solid or liquid then these will move under the influence of the field, producing an oscillating electric current. Resistance to their movement (increased collision rate) causes energy to be transferred to the surroundings as heat. This is conduction heat.

2. Dipolar polarization mechanism: if there are no particles that can move freely in the sample but there are molecules or units with dipole moments then the electric field acts to align the dipole moments. This produces dielectric heating.

The electric field of microwave radiation, like that of all electromagnetic radiation, is oscillating at the frequency of the radiation. The electric dipoles in the solid do not change their alignment instantaneously but with a characteristic time, τ. If the oscillating electric field changes its direction so the time between changes is greater than τ then the dipoles can follow the changes, hence will rotate in phase with the oscillating electric field. A small amount of energy is transferred to the surroundings as heat each time the dipole realigns but this is just a small

heating effect [92]. If the electric field of radiation oscillates very rapidly then the dipoles cannot respond fast enough to realign. The frequency of the microwave radiation is such that the electric field changes sign at a speed that is the same order of magnitude as τ. Under these conditions the dipole realignment falls behind the change of electric field. This phase difference causes energy to be lost from the dipole by molecular friction and collisions giving rise to the dielectric heating [92].

The quantities governing this process are the dielectric constant which determines the extent of dipole alignment, and the dielectric loss, which governs how efficiently the absorbed radiation is converted to heat. To use microwave heating in solid state synthesis at least one component of the reaction mixture must absorb microwave radiation [44]. The relationship for the dielectric constant, ε^*, can be shown as:

$$\varepsilon^* = \varepsilon^{'} + i\varepsilon^{''} \tag{2.3}$$

where $\varepsilon^{'}$ is the ability of the material to be polarized by the external electric field, $\varepsilon^{''}$ (the loss factor) quantifies the efficiency with which the electromagnetic energy is converted to heat and $i = \sqrt{(-1)}$. The relationship between $\tan\delta$ and $\varepsilon^{'}$ and $\varepsilon^{''}$ is purely mathematical [82] and can be described using simple trigonometric rules (Figure 2.3). The following considerations are made: the total current is the vector sum of the charging current and the loss current; the angle δ is the phase difference (lag) between the electric field and the resultant polarization of the material.

$$\tan\delta = \varepsilon^{''}/\varepsilon^{'} \tag{2.4}$$

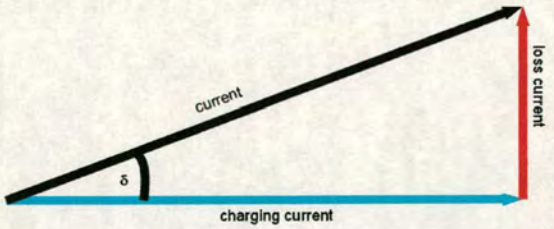

Figure 2.3: *Definition of phase difference and its relation to $\varepsilon^{'}$, $\varepsilon^{''}$ and ε^*, [144]*

2.3.2 Aqueous systems and microwave radiation

In solvent systems the microwave heating results from dipolar polarization [71]. Many solvents have a permanent electric dipole due to the differences in the electronegativity of the atoms of the molecules. The dielectric properties of water and aqueous solutions are clearly relevant to the primary applications of microwave dielectric heating [47]. The water dipole attempts to continuously reorient in the oscillating electric field. Dependent on the frequency the dipole may move in time to the field, lag behind it or remain apparently unaffected. When the dipole lags behind the field then interactions between the dipole and the field leads to an energy loss by heating, the extent of which is dependent on the phase difference of these fields; heating being maximal twice each cycle. The ease of the movement depends on the viscosity and the mobility of the electron clouds [144]. In water, these depend on the strength and extent of the hydrogen bonded network. In free liquid water this movement occurs at GHz frequencies (microwaves) whereas in more restricted 'bound' water it occurs at MHz frequencies (short radiowaves) and in ice at kHz frequencies (long radiowaves). The re-orientation process may be modelled using a 'wait-and-switch' process where the water molecule has to wait for a period of time until favourable orientation of neighboring molecules occurs and then the hydrogen bonds switch to the new molecule [144]. Debye's theoretical expressions for $\varepsilon^{'}$ and $\varepsilon^{''}$ (equations 2.5 and 2.6) control the extent to which a substance is capable to couple with microwave radiation and therefore are the fundamental parameters for interpreting the dielectric heating [47].

$$\varepsilon^{'} = \varepsilon_{\infty} + \frac{\varepsilon_s - \varepsilon_{\infty}}{1 + \omega^2 \tau^2} \tag{2.5}$$

$$\varepsilon^{''} = \frac{(\varepsilon_s - \varepsilon_{\infty})\omega\tau}{1 + \omega^2 \tau^2} \tag{2.6}$$

where ε_{∞} and ε_s are the dielectric constants under high frequency and static fields respectively and ω is the angular frequency in radians second^{-1}. ε_{∞} results from atomic and electronic polarization and ε_s results from the sum of all polarization mechanisms. The relaxation time, also considered as the delay for the particles to respond to the field change, is given as:

$$\tau = \frac{4\pi\eta r^3}{kT} \tag{2.7}$$

where r is the molecular radius, k is the Boltzman constant, T is the temperature and η is the viscosity. The maximum loss occurs when $\omega = 1/\tau$. For water at 25°C, τ is about 8ps and

r is half of the inter-oxygen distance (1.4 Å) [144]. As the temperature or the water activity increases, the strength of the hydrogen bonds decreases, hence the static and optical dielectric permittivities lower. The difficulty for the movement dipole lessens allowing the water molecule to oscillate at higher frequencies and reduce the drag of the rotation of the water molecules which translate in friction reduction and hence the dielectric loss. The maximum for the dielectric loss is encountered at frequencies higher than 2.45GHz, produced by most commercially available microwave ovens [144].

Microwave energy has been successfully applied in the precast concrete industry, to reduced the final setting times of cementitious mortars without degradation of 28-day strength [125]. They were also found to greatly accelerate the formation of apatitic calcium phosphate bone cements [74]. Because microwave energy generates heat in cement pastes due to the dielectric nature of water, microwave heating is a potential method to accelerate cement hydration. However, previous research has revealed several advantages from microwave-assisted wet chemical synthesis in reaction acceleration, yield improvement, enhanced physicochemical properties and the evolvement of new material phases [133].

2.4 Preparation and analysis of samples

2.4.1 Microwave-hydrothermal method

A microwave acid digestion system, MARS 5 (CEM corporation) was used to conduct all microwave-hydrothermal synthesis of calcium aluminium sulphate hydrate. The system is designed for digesting, dissolving, hydrolyzing or drying a wide range of materials and has as primary purpose the rapid preparation of samples for chemical analysis. The system uses a 2.45GHz frequency microwave radiation and can operate at a maximum power of 1.2kW $\pm$15%, but the power can be controlled from 0 to 100%. The system can also be operated under controlled pressure up to a maximum of 800psi and the temperature up to 240°C. The various parameters were monitored and controlled by a programmable microcomputer which is interfaced with the previously stated equipment. The microwave-hydrothermal reactions were carried out in double-walled digestion vessels each of which consists of an inner Teflon vessel and an outer high strength shell made of Ultem polyetherimide. The temperature inside the vessel was measured by an optical probe. The microwave-hydrothermal reactions were carried out at 120°C under autogenous pressure. The experimental programm consisted of 2 stages: a

5min ramp to above mentioned temperatures, followed by holding the samples at that temperature from 1 to 9h. For approximately 40mL of sample, at the aforementioned temperatures the pressure recorded in the sample vessel was 14±1psi.

2.4.2 Conventional oven method

An autoclave system type was built placing a sample cell machined from engineering polymer PEEK [145], in a Pyrex bottle with high temperature screw lid. An appropriate volume of water was sealed in the system in order to obtain a constant inner vapour pressure. The entire autoclave-type system was heated using a conventional oven at 120±5°C from 1 to 22h. After synthesis, the suspensions were cooled to ambient temperature with a cooling step occurring by classical convection (the oven was switched off and the sample left to cool naturally to ambient temperature).

2.4.3 Monosulphate synthesis and characterization

A stoichiometric slurry consisting of calcium hydroxide (4g of Aldrich $Ca(OH)_2$), aluminium hydroxide (2.78g of Aldrich $Al(OH)_3$) calcium sulphate hydrate (3.06g of Aldrich $CaSO_4 \cdot 2H_2O$) in 150mL of water was prepared.

$$\begin{aligned} &3Ca(OH)_2 + 2Al(OH)_3 + Ca(SO_4)_2 \cdot 2H_2O + nH_2O \\ &\rightarrow Ca_4Al_2(SO_4)(OH)_{12} \cdot 6H_2O + (n-4)H_2O \end{aligned} \tag{2.8}$$

The mixing procedure was carried out under nitrogen flow in a glove box to minimize sample carbonation. Later, appropriate volumes of sample were transferred to the Teflon container for microwave heating or the PEEK cell for conventional oven heating.

After the microwave-hydrothermal reaction, or conventional oven heating the solids and solution products were separated by vacuum filtration through a 0.45mm nitrate membrane filter. The solid reaction products were dried on silica gel desiccant beds, with a relative humidity of 12 to 40%, to drive off excess liquid. The dried solids were subsequently characterized by powder X-ray diffraction (XRD) using a Bruker AXS D8 diffractometer with CuK_α radiation (40kV, 40mA). Bragg-Brentano para-focussing geometry with fully monochromated beam was used for almost all samples analysis unless otherwise stated. A position sensitive detector BRAN (PSD) was employed with this geometry to allow rapid data collection. A monochro-

matic X-ray beam is generated by the characteristic K_α emission of a Cu target element, filtered by means of a certain absorbtion edge and additionally sharpened in wavelength by the help of a crystal monochromator. In order to record a reflection of order n from a set of lattice planes (hkl), the incidence angle θ must meet Bragg's condition:

$$n\lambda = 2d\sin\theta \tag{2.9}$$

where the wavelength, λ=1.5406Å and θ is the angle of diffraction relative to the crystalline surface (adjustable). The letter n is an integer, the factor 2 is the result of the diffracted radiation successively passing twice across the space between adjacent planes in the crystal and d is the atomic spacing.

All samples analyzed in this geometry were scanned over an angular range of 5 to 80° 2θ using a step size of 0.014° 2θ with a count time of 0.3s per step. The samples were brought to a suitable grain size using a Retsch mixer mill and then pressed in front loading holders.

Some of the XRD analysis have been complemented by energy dispersive diffraction (EDD) analysis in order to evaluate wether sample preparation alters the results and to interpret the XRD data more fully. EDD is a high-speed method employed to acquire high quality data non-destructively. It is a relatively new technique, first demonstrated by Geissen and Gordon in 1968 [49]. EDD is also based on the form of Bragg's law (Eq. 2.9), where λ, the wave length, is variable, unlike the XRD, and θ, the angle of diffraction relative to the crystalline surface, is fixed (but adjustable). More information on the EDD will be given in Chapter 3, (section 3.2, 3.3) where the technique constitutes the main investigation tool.

2.4.4 Stability involving various relative humidities and temperature

The effects of exposure to either moist or aggressive drying conditions of calcium aluminate monosulphate hydrates (lower and higher hydrate forms), were examined. For this, two main types of experiments were devised: the samples were either conditioned at various relative humidities (r.h.) or dehydrated/rehydrated following a sequence of temperatures from ambient temperature to 200°C.

The conditioning agents used are listed in Table 2.1. Salt in water solutions were prepared and placed in individual desiccators to create the corresponding r.h.%. The desiccators were then stored at ambient temperature from 1 to 4 weeks.

Conditioning agents	Relative humidities (r.h. %)
LiCl	12
$MgCl_2 \cdot 6H_2O$	33
$Mg(NO_3)_2 \cdot 6H_2O$	53
NH_4Cl	79.5
KNO_3	94
$K_2Cr_3O_7$	97

Table 2.1: *Selected relative humidities and corresponding salt in water solutions [58].*

The starting materials were either a fresh product, as resulted from the vacuum filtration following synthesis, or material dried beforehand on silica gel desiccant beds with relative humidity from 10 to 40%.

Furthermore, in order to observe lower hydrate forms than the ones supplied by various conditioning agents, the samples were dehydrated following a sequence of temperatures from ambient temperature to 200°C. The sample decomposition is assumed to occur above 250°C. These experiments were performed in-situ using a Bruker AXS D8 diffractometer (CuK_α radiation, 40kV, 40mA) with an Anton Parr TTK450 heating/cooling stage (Fig. 2.4b). Samples were flat pressed and heated in air. The diffractometer was set up in Bragg-Brentano parafocussing geometry with a monochromated beam.

Rehydration experiments were also carried out in-situ on the XRD to observe the higher hydrates reformation in conditions of 100% r.h. and temperature up to 50°C. For this experiment, a mylar window film with 3μ of thickness was fixed with double sided sticky tape on the sample holder in order to maintain the appropriate r.h. conditions (Fig. 2.4a). The holder has a cavity of 1.5cm in length, 1cm wide and 0.1cm in depth. In all experiments the sample was subjected to weighing in order to prove water loss and the accuracy of phase identification. During this type of analysis, sample high effects are expected due to possible expansion of the sample. Fluid pressure build up causes sample to swell. Therefore sample height effects were overcome by using parallel-beam geometry. In conventional Bragg-Brentano para-focussing geometry the X-ray beam is focussed on the detector (Fig. 2.5a). This technique imposes strict geometric requirements on the sample surface and position [119]. If the sample is irregularly shaped (displays height variation) the beam will be defocused and peak shift will occur. The problems of line broadening and peak shift can be cancelled with a parallel-beam optics. On this purpose a 1mm Göbel mirror exit slit and 0.1mm receiving slit was used to obtain a parallel beam from a divergent one (Fig. 2.5b).

(a)

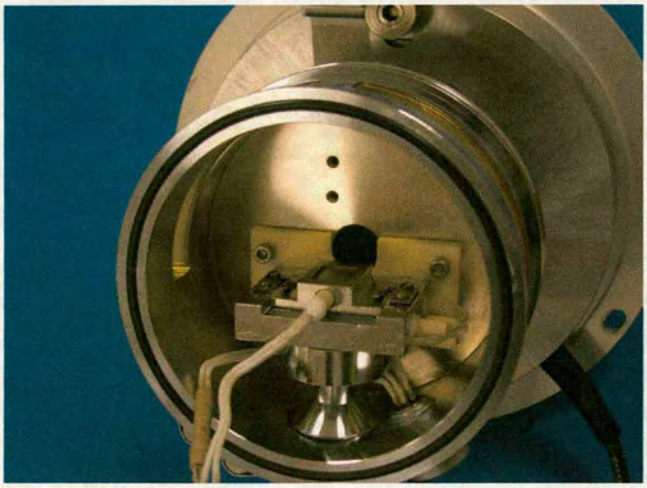

(b)

Figure 2.4: *(a) Holder containing a monosulphate sample rehydrated at 100% r.h.. A mylar window film of 3μm of thickness was fixed with double sided sticky tape on the sample holder in order to maintain the r.h. constant. The cavity of the sample holder is 1.5cm in length, 1cm wide and 0.1cm in depth. (b) Photograph showing diffractometer set-up used for rehydration experiments. An Anton Parr TTK450 heating/cooling stage is used to examine the effects of changes in temperature in-situ from -190° C to +450° C. Samples can be heated in air or vacuum.*

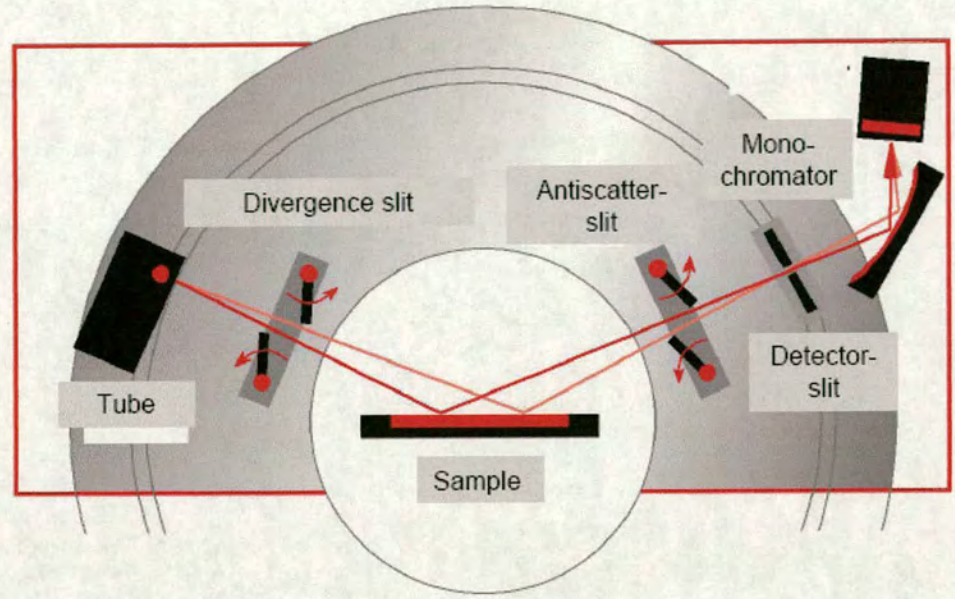

(a)

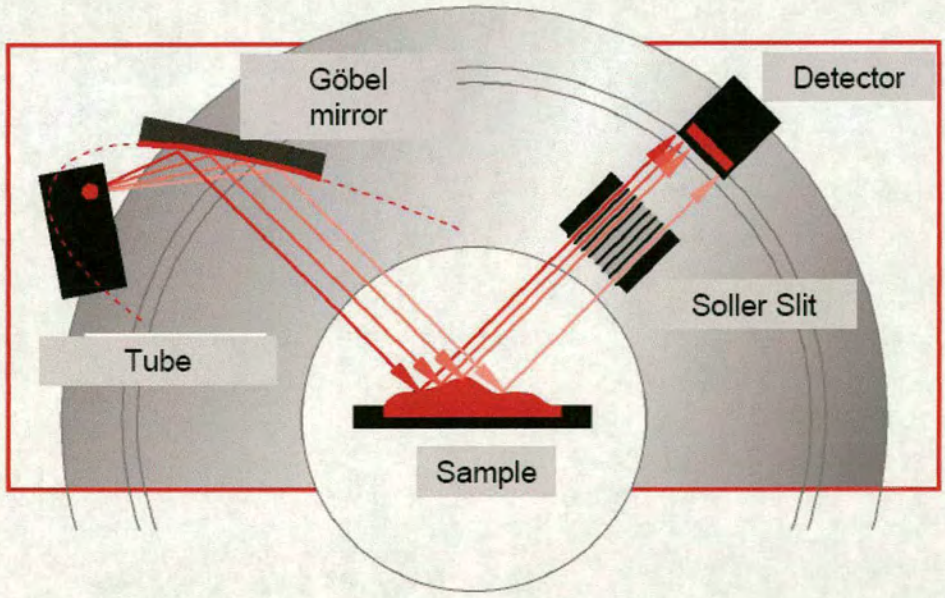

(b)

Figure 2.5: *Focusing diagrams on Bruker AXS D8 diffractometer [142]: (a) conventional para-focusing Bragg-Brentano geometry, (b) parallel-beam geometry using a parabolic mirror in the incident beam path.*

The mirror is a parabolically curved multilayer mirror composed of alternating light and heavy elements (nickel and carbon) [119]. A scintillation counter replaces the PSD used to detect the diffracted X-rays. Long sollers were placed before the detector to exclude non-parallel X-rays. Silica flour was used as a standard to calibrate the experiment and compared with the ICDD (International Centre for Diffraction Data) pattern (Card No. 033-1161). The calibration error was less than 0.5%. Diffraction patterns were collected over an angular range of 5 to 60° 2θ for approximately half an hour total time using a step size of 0.014° 2θ and a count time of 0.1s per step when parallel beam geometry was employed.

2.5 Results and discussion

The preparation methods of sulphate AFm result mainly from solving the equilibrium diagrams in C - $\overline{S}$ - A - H system at different temperatures [68]. However, synthesis of monosulphate in its pure state remains difficult and requires a strict environmental control. Current methods to synthesize pure monosulphate are restricted by an extremely long reaction time, forming crystals insufficiently large and by small quantities of yield material. The yield cannot be increased just by multiplying the batches or increasing the volume of the mixture, due to the variability of the sample (the precipitates obtained in different batches are distinct in composition, even mixed they would not be uniform). Here hydrothermal synthesis assisted by microwaves is proposed to produce the sulphate AFm. Simultaneously, the conventional heating method was also used in order to prove the advantages of the microwaves on chemical systems.

2.5.1 Conventional heating

The sulphate AFm was initially synthesized using the stoichiometric slurry as calculated in Eq. 2.8 and following the conventional method described in section 2.4.2. In this case only one parameter was varied: the hydrothermal synthesis duration from 1 to 19h. The synthesized phases were characterized ex-situ by powdered XRD analysis and energy-dispersive diffraction (EDD) and the corresponding results will be presented below.

XRD/EDD spectra indicate that the sample is crystalline, with peaks characteristic of monosulphate 12-hydrate ($C_4A\overline{S}H_{12}$) structure (Fig. 2.6).

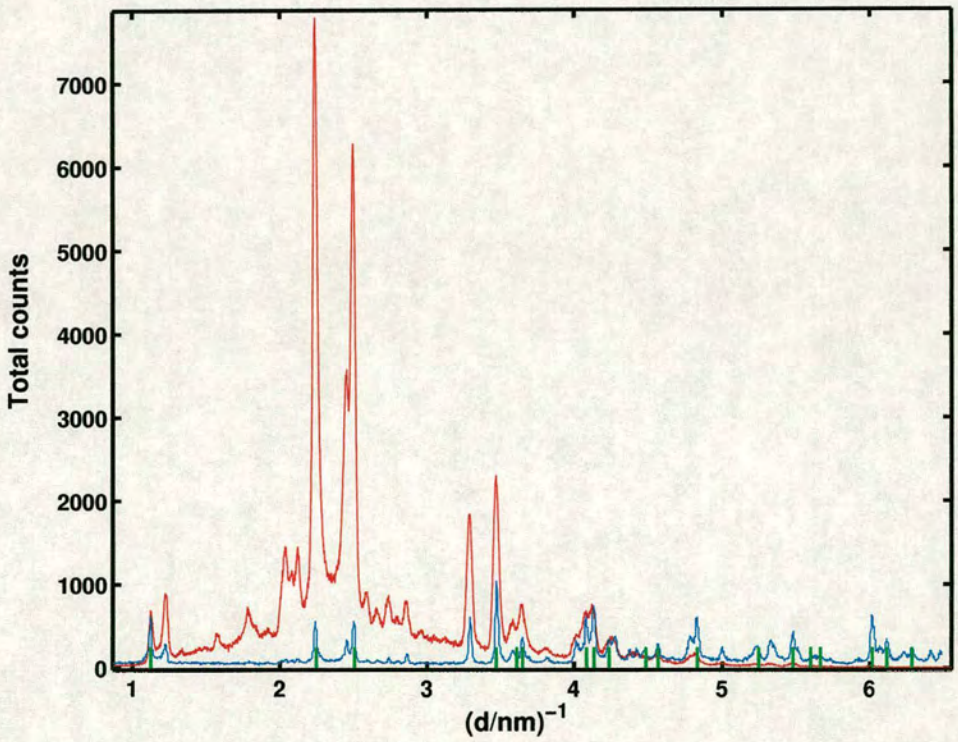

Figure 2.6: *XRD (blue pattern) and EDD (red pattern) spectra illustrating formation of monosulphate accommodating twelve water molecules. Green sticks denote ICDD pattern for 12-water monosulphate (Card No. 45-158). The sample was synthesized at 125 °C ± 4 for 19h, by means of conventional heating method.*

A variation in pattern quality obtained from different systems can be observed. The progression in quality from laboratory to a high resolution Synchrotron is observed from the increased number of diffraction peaks that can be resolved. The intense X-ray beam permits the collection of the powder diffraction pattern with good counting statistic. A superior collimation of the synchrotron X-ray beam is reducing the broadening of the diffraction peaks observed in conventional X-ray and therefore makes them sharper and better resolved. Typically in EDD the radiation is horizontally polarized in the plane of the electron orbit by comparison to laboratory X-ray sources where the polarization is equal in all directions. This means that the rapid fall-off of the intensity associated with laboratory diffraction is reduced.

Improved crystallinity was obtained with longer synthesis times. Small amounts of ettringite and calcite ($CaCO_3$) were identified as the only other foreign phases (Fig. 2.7).

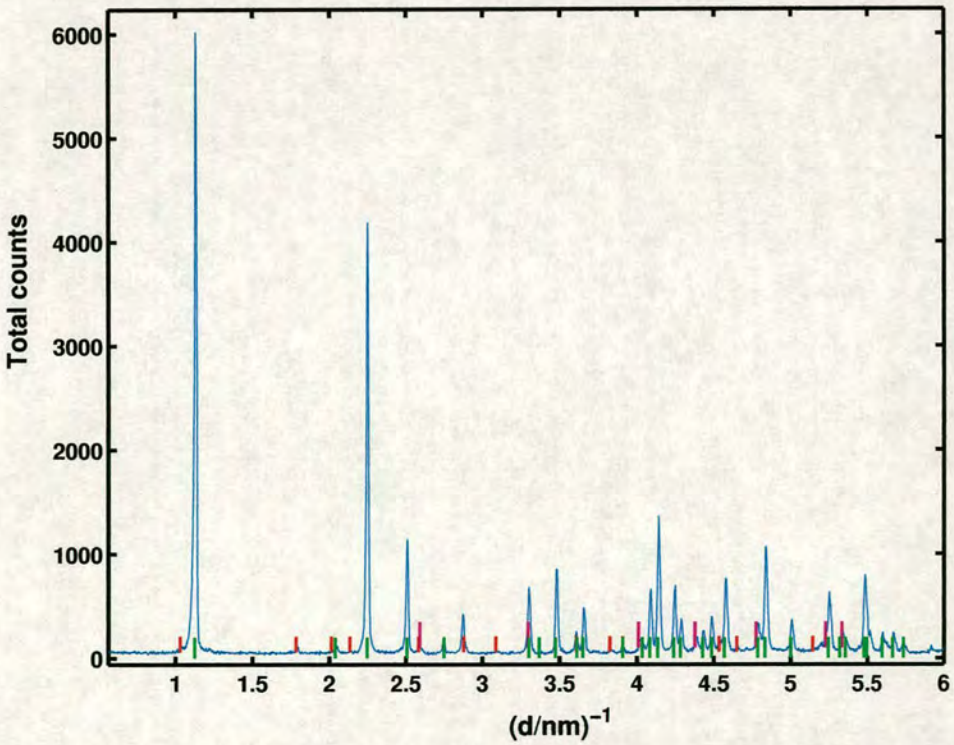

Figure 2.7: *X-ray spectra illustrating formation of monosulphate. Green, red and pink sticks denote ICDD patterns for 12-water monosulphate (Card No. 45-158), ettringite (Card No. 41-1451) and calcite (Card No. 05-0586).*

This suggests a possible carbonation of the sample due to destabilization of the system under nonequilibrium conditions (non-conservation of water content and the pressure in the autoclave due to inadequate seals) and consequently an incomplete transition of ettringite to monosulphate takes place.

Alternatively, on cooling from elevated temperature there is a possible partial disproportion to form ettringite, but there is no clear proof. However this synthesis has proved to be not wholly reproducible in subsequent experiments. The evidence suggests the interconversion of the hydrates is an easy rapid process whereby metastable phases are readily formed. All this strongly indicates that the C - $C\overline{S}$ - A - H system is labile and is not yet fully understood. Conventional heating does not allows easy observation of all complex sequences of changes which occur during mineral transformations. It should be noted here that in all conventional heating, energy is transferred from the surface, to the bulk mixture (the mixture must be in physical contact with a surface that is at higher temperature than the rest of the mixture), and eventually to the reacting species. The energy can act in two ways: it can increase the reaction kinetics or make the reaction thermodynamically allowed [82]. Nevertheless spontaneous mixing of the reaction mixture can occur through convection in the absence of mechanical means. Thus the homogenous distribution of reagents and temperature throughout the autoclave does not take place and so the transformation of ettringite to monosulphate is incomplete.

In conclusion, monosulphate synthesis by means of conventional heating can provide 100% crystalline material, for relatively long synthesis time, over 19h, and poor degree of purity. The difficulty to secure good seals of the system complemented by a non-uniform heating establish this method as insufficient to produce high quality yield.

This made the subsequent use of the synthesis product, to study its stability involving various relative humidities and temperatures, impossible.

2.5.2 Microwave heating

The use of microwave heating for the synthesis of sulphate AFm is evaluated here. Starting from the stoichiometric formulation (Eq. 2.8) we demonstrate that microwave heating drastically shortens the synthesis duration. It was decided to use microwave heating to accelerate the very long synthesis time typically described in the literature and in section 2.5.1. The structure of as-synthesized monosulphate was determined by X-ray diffraction patterns (XRD). Fig. 2.8 shows the XRD patterns of as-synthesized sample immediately after filtration in the wet state compared with samples dried over silica gel desiccant beds at ambient temperature.

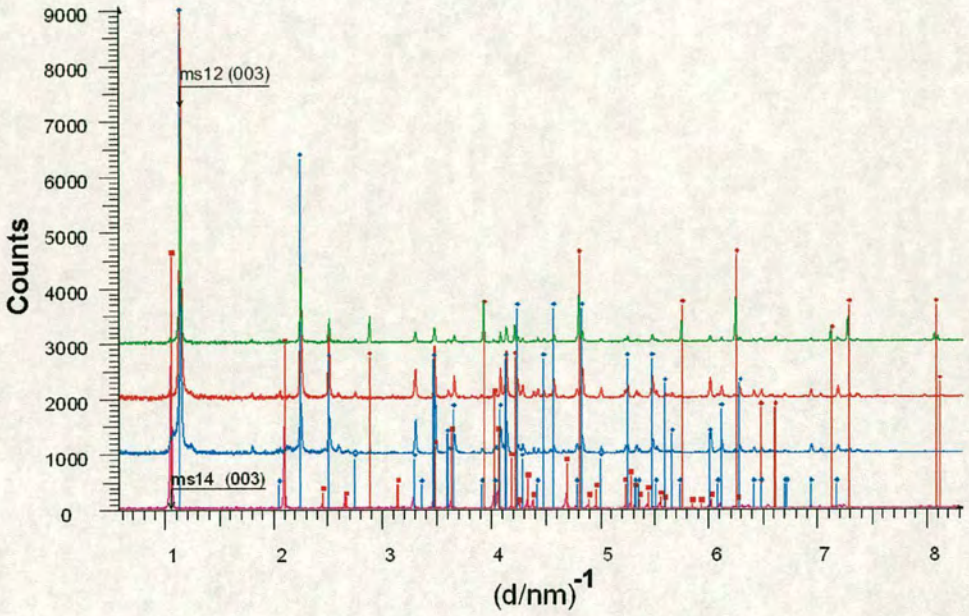

Figure 2.8: *Comparative diffraction patterns of monosulphate showing positions of peaks relative to ICDD patterns for 14-hydrate, 12-hydrate monosulphate and corundum. Bottom pattern represent the sample as-synthesized and the others represent patterns of samples obtained from different synthesis. The duration of the synthesis was 9h for all samples. Green, blue and red sticks denote 14-hydrate, 12-hydrate monosulphate and corundum. Corundum was added as internal standard (mixed with the sample in a known proportion) in the last sample to confirm accurate peak positions. Key:* ms12 = $C_4A\overline{S}H_{12}$, ms14 = $C_4A\overline{S}H_{14}$

After 9h of synthesis, the pattern of the sample X-rayed when still moist with the mother liquor shows peaks characteristic of monosulphate 14-hydrate ($C_4A\overline{S}H_{14}$) structure (at 0.95nm, 1/d 1.05nm^{-1}). Under conditions of low r.h. (12 to 40 %) this phase dehydrates to 12-hydrate monosulphate ($C_4A\overline{S}H_{12}$) with a basal spacing of 0.89nm (1/d 1.12 nm^{-1}). These compounds have the same crystal structure and differ only in the presence of hydrate water present in the zeolitic channels. Some of the water in these compounds is tightly bound chemically; the remainder is more loosely bound and capable of variation with ambient temperature and humidity. In order to give a good representation of multiple scans, that highlights trends between scans in time, a level view mode was chosen. The level view is an X-Z view of the 3D data. The scans are always displayed with increasing reaction time and cover exactly the same range and were measured at the same step-size. The information on Z is given by iso-intensity curves (contours). A local maximum of the surface corresponds to a contour of the iso-intensity lines forming concentric circles around a point.

Increasing the synthesis time shows the whole scenario for monosulpate formation. In the Fig. 2.8 and 2.9, the following sequence of d-spacing was found: 0.97nm (1/d 1.03nm^{-1}), 0.95nm (1/d 1.05nm^{-1}) and 0.88nm (1/d 1.13nm^{-1}) which correspond to ettringite, 14-hydrate and 12-hydrate monosulphate, respectively. The first period of reaction is characterized by the presence of ettringite even in the case of stoichiometric composition for monosulphate, in keeping with the observations of Havlica [64].

The measured pH of all samples at the end of synthesis varies between 11.6 and 12.5. This high OH^- concentration favours formation and longer persistence of monosulphate. The average pressure measured in the vessel was 10psi, the equivalent of $\sim$0.68bar. For this pressure, the boiling point of the system will be reached at approximately $\sim$90°C, which will correspond with the start of ettringite decomposition. After 3h synthesis we observe the ettringite peak (reflection 1 0 0 at 0.97nm 1/d 1.03nm^{-1}) decreasing at the expense of monosulphate 14-hydrate formation (reflection 0 0 3 at 0.95nm (1/d 1.05nm^{-1}). Small amounts of gypsum co-exist with the resulting products for up to 7h after which they are completely consumed to form monosulphate 14-hydrate.

The contour plot in Fig. 2.9, shows a sample conditioned on a silica desiccant beds for 2 weeks suggesting the cohabitation of ettringite and monosulphate phases up to 7h of synthesis. The co-existence of the two hydrated forms suggest two types of 14-hydrate structures, one in which the water is tightly bound chemically and a second were the water is more loosely bound, hence monosulphate 14-hydrate is capable of variation with ambient temperature and the above mentioned humidity. If samples were conditioned in the same conditions for an additional two weeks we observe a partial disproportion to form ettringite. It is apparent that the trisulphate was being reformed during the exposure, proving the metastability of the monosulphate 14-hydrate structure at room temperature.

Fig. 2.10 shows several XRD scans on samples analyzed after 4 weeks of conditioning at r.h. between 13-40%. Only ettringite and monosulphate 12-hydrate were observed as stable phases in these conditions.

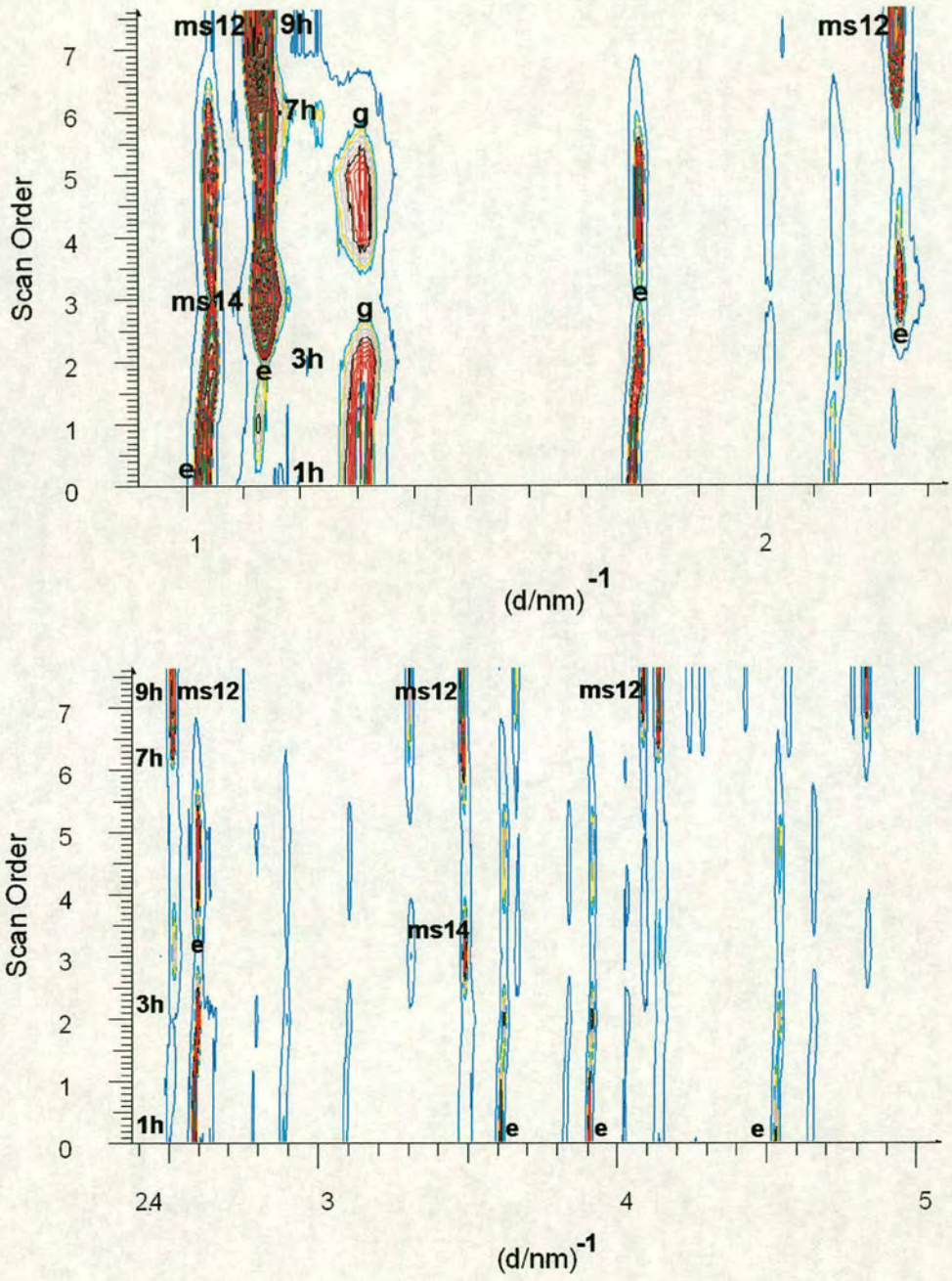

Figure 2.9: *Contour plot of several XRD scans illustrating mineralogical changes through time. Scans were collected on samples with synthesis times from 1 to 9h, 2 weeks after they were conditioned over silica gel desiccant beds with r.h. between 13 - 40%. Key:* ms12 = $C_4A\overline{S}H_{12}$, ms14 = $C_4A\overline{S}H_{14}$, e = $C_6A\overline{S}_3H_{32}$

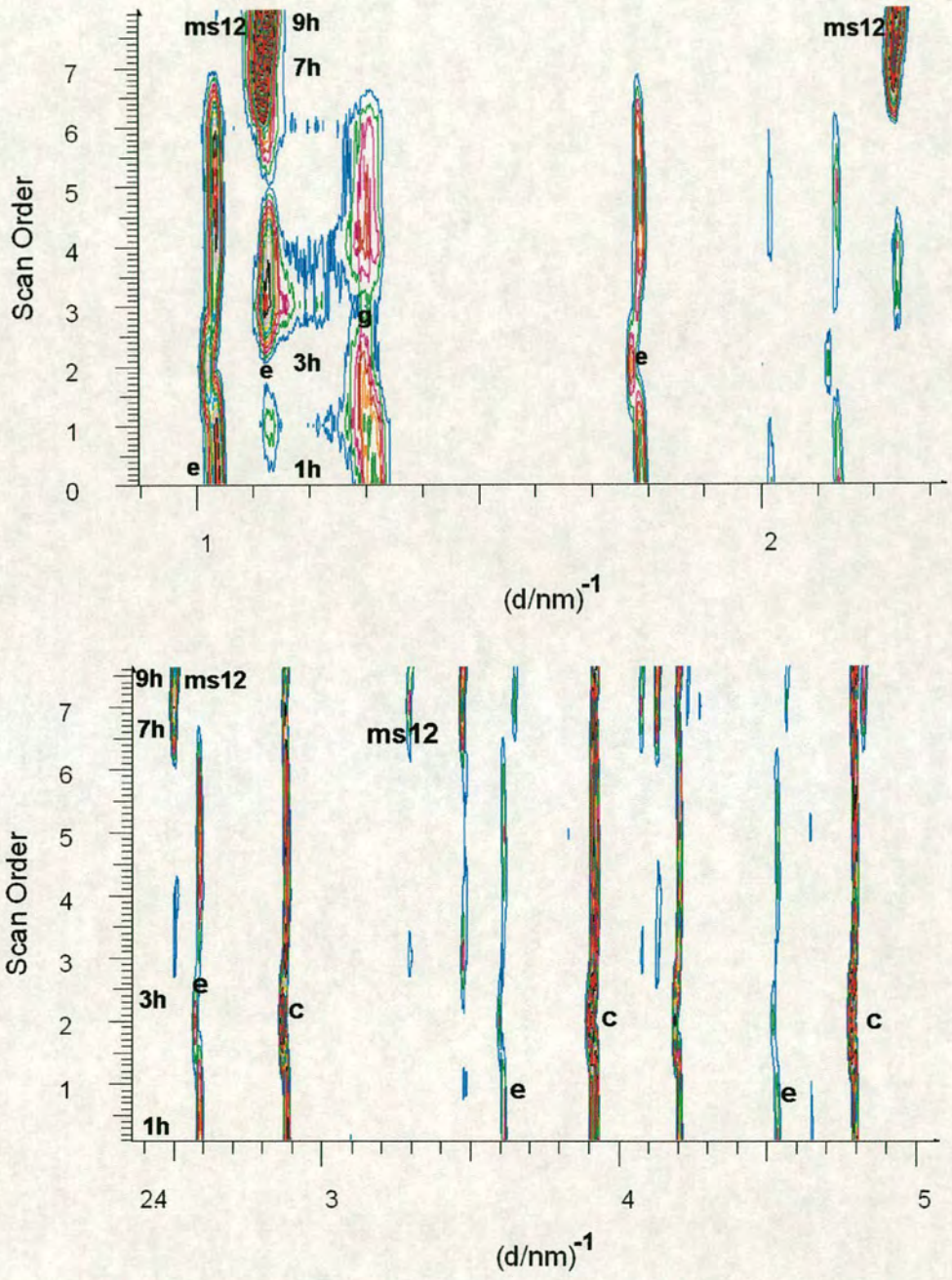

Figure 2.10: *Contour plot of several XRD scans illustrating mineralogical changes through time. Scans were collected on the same samples as in figure 2.9, which were conditioned at the same r.h. for another 2 weeks. Corundum was added as internal standard for accurate identification of peak position. Key:* ms12 = $C_4A\overline{S}H_{12}$, ms14 = $C_4A\overline{S}H_{14}$, e = $C_6A\overline{S}_3H_{32}$, c = Al_2O_3

2.5.3 Stability of monosulphate hydrate

By the reduction in the temperature and/or augmentation of the hygrometry one reforms initial aluminates. To observe the hydration stages of monosulphate, the samples were first conditioned at various relative humidities (r.h.) using different conditioning agents, as described in section 2.4.4. Samples consisting of monosulphate 14-hydrate were exposed when still moist with the mother liquor. The dehydration process was followed by X-ray analysis.

As can be seen in Fig. 2.11 after one week of exposure, monosulphate 14-hydrate is stable above 94% r.h.. Below 79% r.h. at ambient temperature, complete transition to the low-hydrate form is observed. This corresponds to monosulphate 12-hydrate with a characteristic peak at 0.88nm (1/d 1.13nm^{-1}). This is in agreement with the work of Dosch and Keller [40] which state that the dehydration of 14-hydrate to 12-hydrate occurrs at room temperature and 95% r.h..

If aggressive dehydration then proceeded in a vacuum, an additional peak to that of monosulphate 12-hydrate, with basal d-spacing of 0.804nm (1/d 1.24nm^{-1}) is observed. This corresponds to a hydrate form with water content less then 10 molecules. Monosulphate 10-hydrate, with basal spacing of 0.815nm (1/d 1.22nm^{-1}) was observed on a sample dehydrated on silica gel desiccant beds with r.h. maintained to 10%. The relative humidity at which the 10-hydrate is observed here is much lower than the one stated by Dosch and Keller [40].

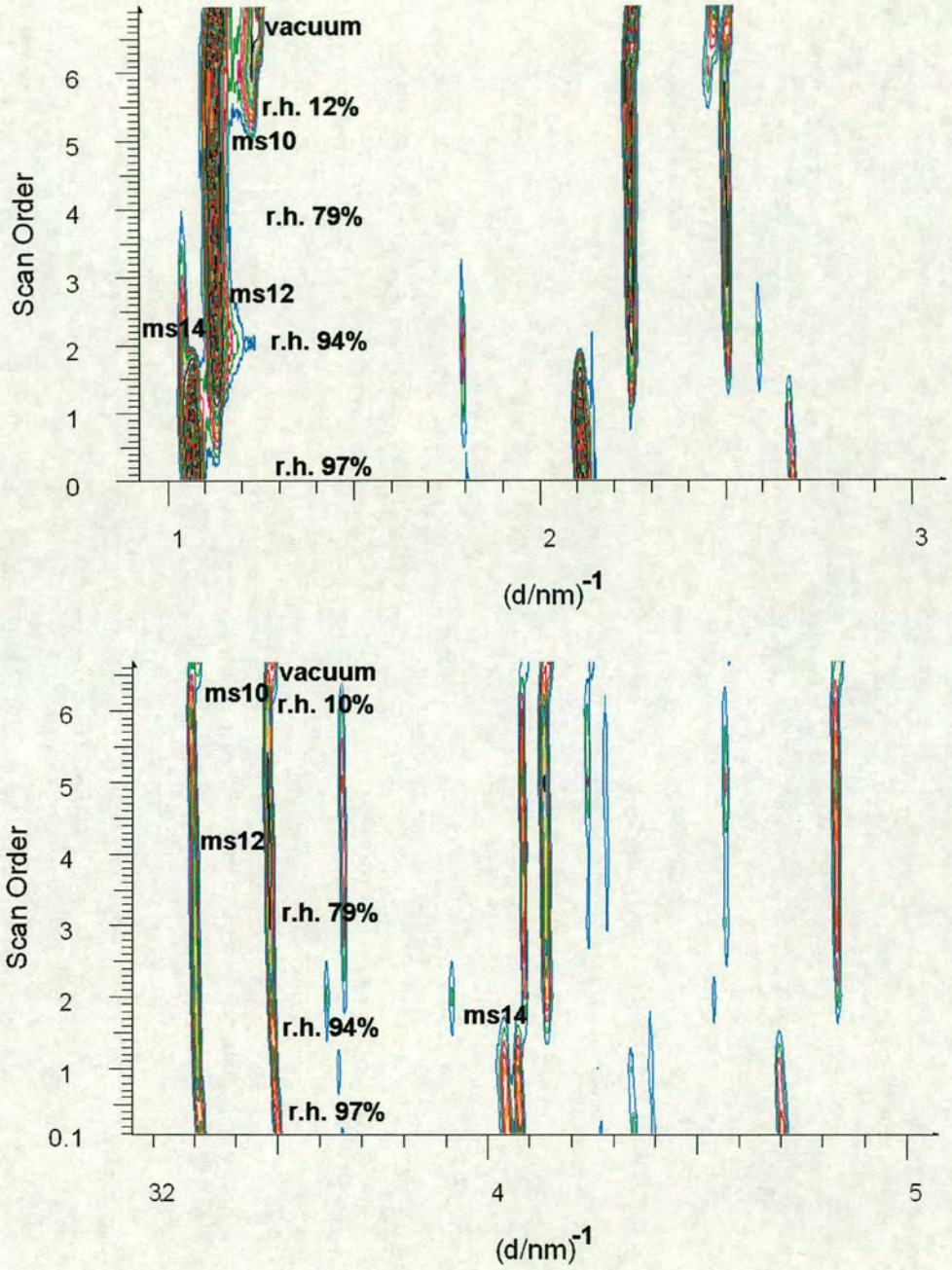

Figure 2.11: *Contour plot of several XRD scans illustrating mineral changes as function of r.h.. All range of r.h. was covered as in Table 2.1. Additional samples were also vacuumed. The starting material was 14-hydrate still wet with the mother liquor. Key: as in Fig. 2.10,* ms10 $= C_4A\bar{S}H_{10}$

The effect of relative humidity on dried specimens was also investigated. For samples previously dried using the hydration/dehydration yield interesting results. Fig. 2.12 shows reformation of ettringite for r.h. above 79%.

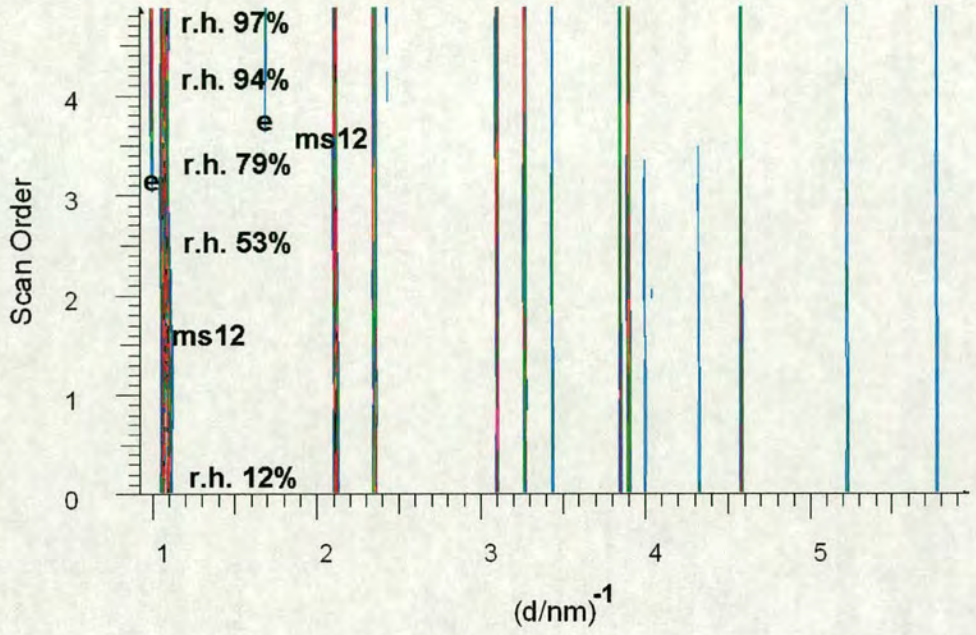

Figure 2.12: *Contour plot of several XRD scans illustrating mineral changes as function of r.h.. The sample was dry material previously conditioned on silica desiccant beds with r.h. 30%.*

Aggressive dehydration of monosulphate 12-hydrate at elevated temperature in a dry state (r.h.=12) was observed using the heating stage as described in section 2.4.4. Fig. 2.13 shows the main changes in basal d-spacing at 40 and 100°C. We observe monosulphate 12-hydrate conversion to 10-hydrate with d-spacing of 0.81nm (1/d 1.23nm^{-1}) occurring at 40°C.

Further dehydration produces a split off of two more water molecules from the interlayer obtaining a phase with basal spacing of 0.79nm (1/d 1.26nm^{-1}) occurring at 100°C. This corresponds to 8-hydrate as the d-spacings plot linearly for water loss (Fig. 2.13).

In presence of 100% r.h and temperature of 60°C, using the same set-up described in section 2.4.4, we observe complete rehydration of 12-hydrate to monosulphate 14-hydrate (figure 2.14).

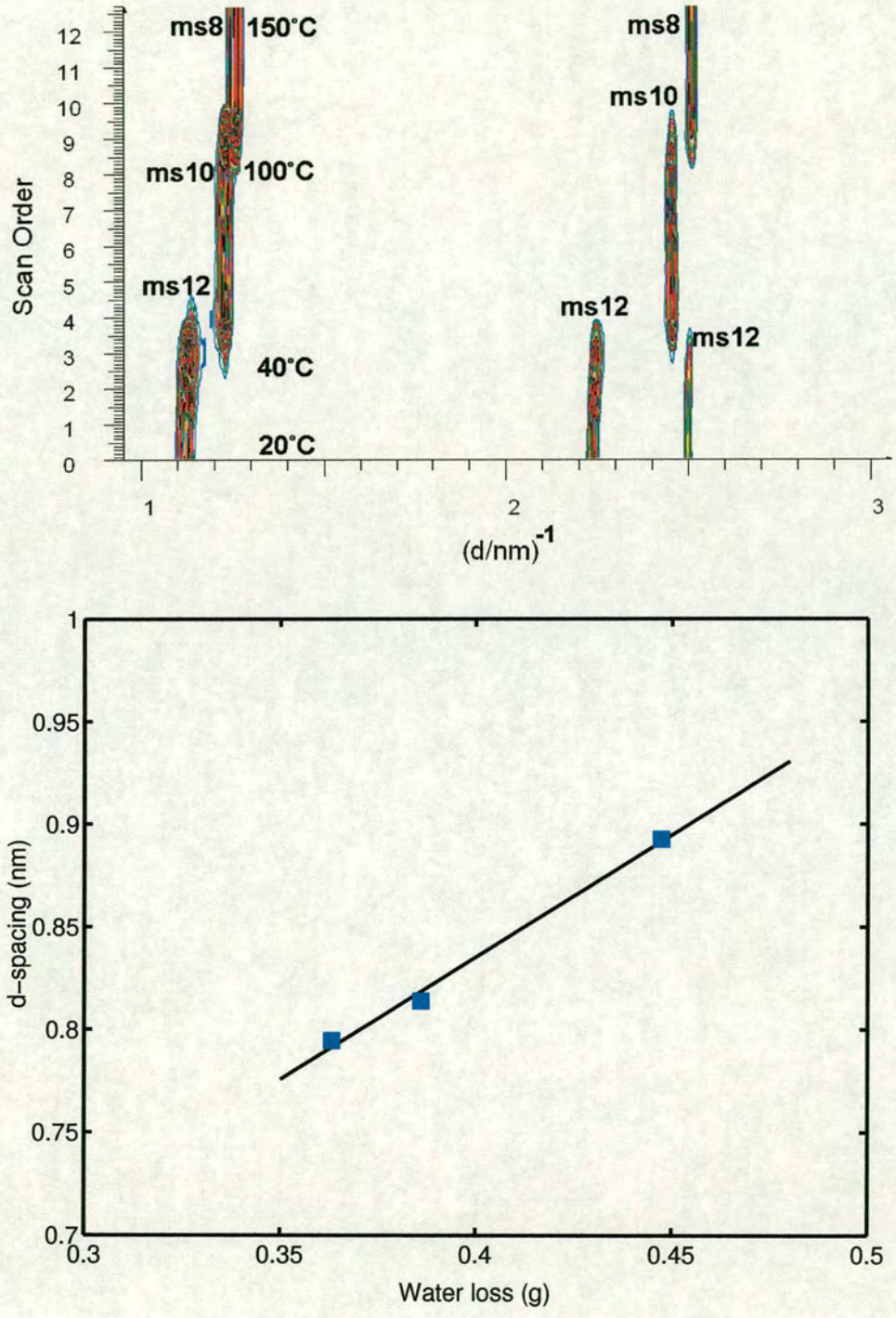

Figure 2.13: *(a) Contour plot of several XRD scans illustrating monosulphate 12-hydrate dehydration as function of temperature. The temperature was ramped from 25 to 150°C. Two main transformations are observed at 40 and 100°C when conversion to 10 and 8-hydrate monosulphate occurs. (b) Plot of d-spacing changes versus water loss.*

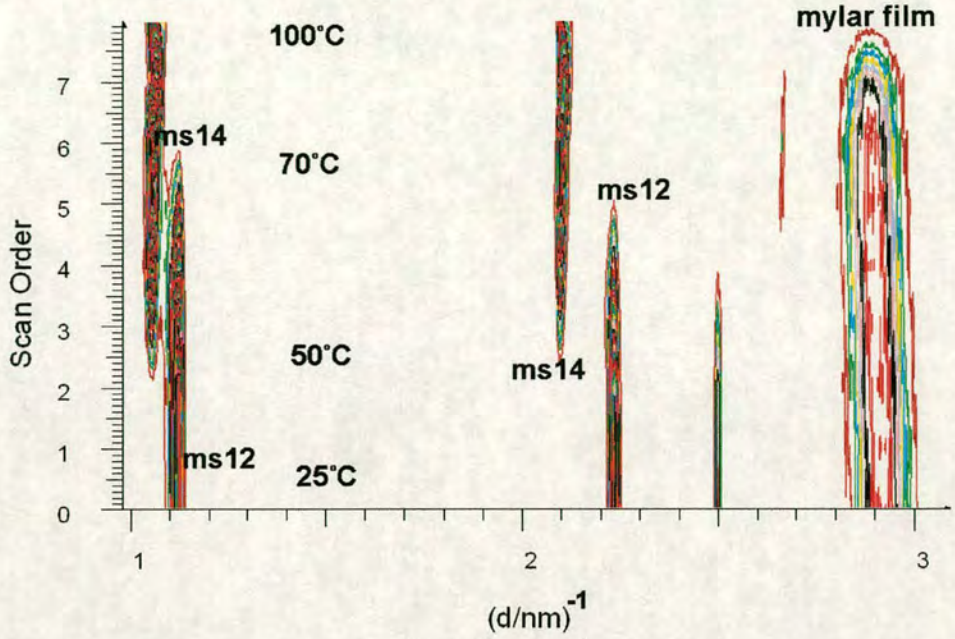

Figure 2.14: *Contour plot of several XRD scans illustrating monosulphate 12-hydrate rehydration to 14-hydrate as function of temperature. The temperature was ramped from 25 to 150 °C. The transformation occurs at 60° C.*

2.6 Conclusions

The practical importance of mapping the hydrothermal stabilities of these compounds lies in their involvement as intermediates and products of the hydration of portland cements under geothermal conditions. As with many compounds encountered in portland cement chemistry, the water content is not always clearly stated.

A novel method for monosulphate synthesis was provided and monosulphate hydration stages were investigated.

1. From reaction mixtures, the monosulphate 14-hydrate (as-synthesized sample, in wet state) was obtained by hydrothermal synthesis using microwave radiation at 120°C. Although 100% crystalline samples have been obtained by both synthesis methods, the overall synthesis time is shortened from 19h to 9h in the microwave-assisted heating compared with the conventional method. Microwave heating has several advantages over conventional heating: it is able to reduce non-uniformity due to its superior penetration depth and it can better control the energy absorbtion which leads to optimization of the overall heating process.

2. Monosulphate formation is via ettringite thermal decomposition in autoclave conditions under autogenous pressure. It has been shown that a series of AFm hydrates can be obtained depending on temperature and water activity. Some of the water in these compounds is tightly bound chemically; the remainder is more loosely bound and capable of variation with ambient temperature and humidity.

3. After one week of exposure to salt solutions with various r.h., monosulphate 14-hydrate is stable above 94% r.h.. Below 79% r.h. and ambient temperature, transition to monosulphate 12-hydrate is observed.

4. Monosulphate 14-hydrate is found to be a metastable phase in conditions of ambient temperature and r.h. up to 40%. This phase dehydrates to 12-hydrate in above mentioned conditions and for longer exposure times presents a disproportion to form ettringite.

5. Monosulphate 10-hydrate was observed on samples dehydrated on silica gel desiccant beds with r.h. maintained to 10% or more aggressively in vacuum conditions.

6. The following sequence of transformations: monosulphate 12-hydrate - monosulphate 10-hydrate - monosulphate 12-hydrate was observed at elevated temperature in dry state. Two main transformations are observed at 40 and 100°C when conversion to 10 and 8-hydrate monosulphate occurs.

7. At 60°C and 100% r.h monosulphate 12-hydrate reconverts back to monosulphate 14-hydrate.

Chapter 3

Calcium sulphoaluminate hydrates: a synchrotron diffraction study up to 150°C and reversion on cooling

In this chapter new information on combined effects of temperature and alkali on the stability of ettringite and monosulphate, studied in-situ by synchrotron energy dispersive diffraction (EDD), are reported.

3.1 Introduction

The conditions under which the calcium sulphoaluminate hydrates form or are stable are of great importance with regards to the setting of cement paste and the durability of concrete [17]. Hence the stability of calcium sulphoaluminate hydrates has received renewed interest associated with controversies over the temperature and alkali influence.

The complex calcium sulphoaluminate hydrates are formed in the initial stage of portland cement hydration by the reaction of the aluminate phases, calcium sulphate and water. In almost all commercial cements, which contain any form of calcium sulphate ($C\overline{S}H_x$), ettringite ($C_6A\overline{S}_3H_{32}$) is the first complex hydrate to crystallize because of a high sulphate/aluminate ratio in the solution phase during the first hour of hydration [48]. Once the calcium sulphate initially present has been consumed ettringite begins to decompose and monosulphate ($C_4A\overline{S}H_n$) forms in its place.

The ettringite forms in the first few hours of hydration of tricalcium aluminate (C_3A) and brownmillerite (C_4AF) and plays a key role in setting [88]. After a few days hydration only a small amount remains in the cement paste. In portland cements, the average content of C_3A and C_4AF is about 4-11% and respectively 8-13% [113]. The hydration of C_3A is controlled by the addition of calcium sulphate dihydrate, thus the flash set is avoided.

In cements, monosulphate either forms at ambient temperature by exhausting the sulphate source [78] or above 114°C by ettringite decomposition [59]. Formed after AFt disappearance, this phase constitutes 10% of the solid phase in a mature cement paste. The reactions of C_3A and C_4AF with $C\overline{S}H_2$ proceed as follow:

$$C_3A + 3C\overline{S}H_2 + 16H \rightarrow C_6A\overline{S}_3H_{32} \tag{3.1}$$

$$2C_3A + C_6A\overline{S}_3H_{32} + (3n - 32)H \rightarrow 3C_4A\overline{S}H_n \tag{3.2}$$

$$C_4AF + 3C\overline{S}H_2 + 30H \rightarrow C_6A\overline{S}_3H_{32} \tag{3.3}$$

$$C_6A\overline{S}_3H_{32} \rightarrow C_4A\overline{S}H_n + 2C\overline{S}H_2 + (28 - n)H \tag{3.4}$$

where n is variable [131], but commonly n = 12 or 14. The C_4AF phase is known to yield the same sequence of products as C_3A, however, the reactions are slower [131]. Nevertheless the rate of hydration depends on the composition of the ferrite phase. The relatively slow hydration of brownmillerite in the absence of calcium sulphate at low temperature (below 50°C) suggests that $C\overline{S}H_2$ is not essential for control of early hydration kinetics in portland cements with low aluminium/iron ratio [88].

AFt and AFm stability is frequently considered with respect to the availability of sulphate. Since the aluminate to sulphate balance in the solution phase of the hydrated portland cement paste primarily determines whether the setting behaviour is normal or not, various setting phenomena are affected by an imbalance in the aluminium/sulphate ratio. During a thermal excursion, a considerable repartition of sulphate occurs between cement containing solid and aqueous phases. AFt may dissolve in part or completely at 85°C to maintain high SO_4 levels required by the solubility products of AFm /AFt [3]. Upon cooling these processes are reversed and AFt precipitation occurs. This mechanism underlies the damaging reversionary ettringite found in some heat-cured cements. The stability of calcium sulphoaluminate hydrates is strongly influenced by the temperature and solution chemistry [17]. At room temperature, the stability region for AFt and AFm was determined by establishing the quaternary C - $\overline{S}$ - A - H system [32, 68, 69]. More recently, the system was comprehensively reviewed by Taylor [131] and Damidot and Glasser [30, 31], for a range of temperatures (25 - 85°C) and alkali (Na_2O) contents.

Using thermodynamic modelling, the stable phases predicted, at 25°C, are CH, C_3AH_6, AFt, AH and $C\overline{S}H_2$ with the invariant points given by the stable 3-phase assemblage (Fig. A.1a):

1. CH + C_3AH_6 + AFt,
2. CH + AFt + $C\overline{S}H_2$,
3. C_3AH_6 + AFt + AH,
4. AFt + AH + $C\overline{S}H_2$.

AFm is confirmed to be metastable at ambient temperature, although in reality it does form in cement-based systems due to hydration being a very dynamic process. During the hydration of C_3A and C_4AF systems a lot of heat is released. Only C_4AF hydration, alone, supply heat need to form monosulphate [88]. More details on phase relations and and solubility equilibria are presented in the appendix (Fig. A.1a). The effect of temperature and alkali concentration on invariant point compositions are also included (see Table A.1).

An increase of temperature drastically influences the stability of each hydrate. Between 60°C and 80°C AFt becomes unstable with respect to AFm and calcium sulphate [120]. The breakdown of the crystalline hydrated calcium aluminium sulphates reduces the bound water content relative to the degree of hydration. For temperature higher than 50°C, there are 6 stable phase assemblages predicted (Fig. A.1b):

1. CH + C_3AH_6 + AFm,
2. CH + AFm + AFt,
3. CH + AFt + $C\overline{S}H_2$,
4. C_3AH_6 + AFm + AH,
5. AFm + AFt + AH,
6. AFt + $C\overline{S}H_2$ + AH.

At temperatures approaching 100°C monosulphate also becomes unstable and hydrogarnet phases (C_3AH_6) may form. Taylor reports the formation of hydrogarnet in cement pastes moist cured at 90°C for 2 months [131].

In portland cement clinker, alkalies such as Na and K are present. They are derived from the clay components accompanying the raw mix. The total amount expressed as Na_2O equivalent (Na_2O + 0.64 K_2O) ranges from 0.3 to 1.5 %. Their presence is known to have a significant influence on the early hydration reactions of the cement [85]. More specific, the presence of alkali contributes to OH^- or pH concentration in real cements [31]. The pH variation as a function of sulphate concentration is particulary relevant to the stability of calcium sulphoaluminate hydrates. In alkaline environment (Na_2O), there are no new hydrated phases formed in the system C - $\overline{S}$ - A - H. Phase relations are similar, but the disposition of the solubility surfaces in space are strongly affected [3]. Damidot *et al.* [30] have shown that with increasing Na content and constant temperature, Ca is depressed while Al and especially SO_4 are increased. For an increase of Na content from 0 to 1.0 M/L SO_4 levels are increased from 0.015 to 11.22mM/L for the following phase assemblage C_3AH_6 + AFt + CH. The balance between OH^- and $SO_4{}^{2-}$ moves to higher $SO_4{}^{2-}$ levels even further, with increasing temperature. This increase is not only due to the decomposition of the sulphoaluminate phases, but also as a result of a shift to the right of the equilibrium between alkali hydroxide, calcium sulphate compounds, alkali sulphates and calcium hydroxide with increasing temperature [120]:

$$CaSO_4(s) + 2Me^+(aq.) + 2OH^-(aq.) \leftrightarrow Ca(OH)_2(s) + 2Me^+(aq.) + SO_4^{2-}(aq.) \quad (3.5)$$

where $CaSO_4(s)$ represents sulphate in AFt, AFm and gypsum and Me = Na, K.

At 85°C, 1.0 M/L NaOH and $SO_4(aq.)$ = 193 mM/L the following assemblage was predicted: C_3AH_6 + AFm + CH (Fig. A.2) [30]. These two assemblages hold in the more complex OPC.

A variety of investigations have been concerned with the thermostability of AFt in pure systems, in cements and in alkaline environments. It has been reported that ettringite decomposes at 10^{-6} bar at 18°C, at 74°C under conditions of normal humidity and pressure, and at 84°C in wet N_2 gas [52]. When autoclaved at 120°C, ettringite decomposes to AFm and calcium sulphate hemihydrate [59]. At temperatures higher than 190°C, sulphate free AFm (hydrogarnet) was observed, but undecomposed ettringite was still present [117]. When synthetic material of AFt was examined in NaOH solutions up to 1 M and heat treatment at 80°C, it was found to convert to a Na-substituted AFm phase ($C_4A\overline{S}_{1.5}N_{0.5}H_{15}$/'U - phase') [123]. Instead, no U-phase was observed when AFt was directly synthesized in presence of NaOH and temperatures from 40 to 80°C, with a 3:1 sulphate to aluminate ratio [23]. AFt + $C\overline{S}H_2$ are the only crystalline phases identified, evidence that disproves the calculated phase assemblage predicted

by the speciation program. However, the rate of ettringite formation was retarded in NaOH at all temperatures when compared with synthesis in deionized water [23]. Complex assemblages consisting of: AFm + AFt + U - phase were observed for 1:1 sulphate to aluminate ratio [24].

While much work has been done examining the formation of calcium sulphoaluminate hydrates and the interaction of various ionic species, only a few studies have examined the combined effects of alkali and temperature on kinetics [23, 24, 30, 31, 123]. Investigations on calcium sulphoaluminate hydrates obtained in various conditions were typically carried out ex-situ on reaction products where the reactions had been stopped in some way. This is commonly done by adding acetone or methanol and such treatment may remove water from very delicate hydrous phases, such as calcium sulphoaluminate hydrates. Moreover, under hydrothermal conditions, it is difficult to quench the reaction satisfactorily. As there has been much discussion as to whether intermediate phases may not be detected during formation of calcium sulphoaluminate hydrates, or accurate transformation temperatures are not obtained, it was decided to use a time-resolved, in-situ diffraction method to solve this problem. Synchrotron diffraction using hard X-ray allows the observer to see the phases which are present in a bulk sample throughout the course of the reaction in the presence o water and without inducing sample preparation artifacts [88].

The purpose of this chapter is to further study the stability of ettringite and monosulphate in hydrothermal, alkaline environments using synchrotron energy dispersive diffraction. The practical importance of mapping the hydrothermal stabilities of these compounds lies in their involvement as intermediates and products of hydration of portland cements under hydrothermal conditions. There is much interest in the use of mineral/solution equilibrium models for predicting mineral transformations under hydrothermal environments and synchrotron X-ray diffraction provides the only realistic way to monitor complex sequences of changes which occur [8]. Two experiments are proposed as follow:

1. Direct synthesis of monosulphate hydrate, $Ca_4Al_2O_6(SO_4) \cdot xH_2O$, thermal stability up to 150°C and reversion on cooling. The conventional laboratory X-ray diffraction study undertaken in chapter 2 has detailed the whole process regarding the monosulphate formation and its stability but there are still uncertainties. The monosulphate is found to be a very delicate phase and very sensitive to any change of humidity therefore in-situ synthesis will solve any concern regarding the reaction products and their stability on cooling from elevated temperatures;

2. Alkali (NaOH) influence on ettringite thermal decomposition at 150°C to test the thermodynamic predictions of Damidot and Glasser [30, 31] on hydrate stability in the CaO - Al_2O_3 - $CaSO_4$ - H_2O system in the presence of additional ions such as sodium.

3.2 The Synchrotron and in situ energy-dispersive diffraction

A synchrotron is a cyclic particle accelerator that boosts the velocity of electrons, protons or ionized atoms very close to the speed of light (e.g. ~0.9999 of the speed of light at 2GeV). It is a fundamental principle of physics, that when charged particles are accelerated they emit electromagnetic radiation [8]. A wide range of electromagnetic radiation are produced by a synchrotron. However, they are often constructed so that the predominant emission consists of X-rays. In a synchrotron this energy may used for a number of experimental purposes.

Particle acceleration is caused by a variable magnetic field coupled with a variable frequency of electric field. An adequate adjustment of these parameters secure a constant path of the particles during acceleration. This allows the vacuum container for the particles to be a ring. The shape also allows and requires the use of multiple magnets to bend the particle beam.

X-rays produced by the synchrotron method have several advantages over those from conventional sealed X-ray tubes [8]. The X-ray beam is more intense, hence useful data may be collected from samples of much smaller volumes in a much shorter time. Despite the continuing success of conventional diffractometers, the higher intensity patterns obtain with synchrotron radiation can be used to resolve more difficult space group or symmetry problems, or can more easily identify minor phases present in the samples [19, 95, 135]. Another advantage of synchrotron radiation is the continuum wavelength produced from infrared to hard X-ray. Thus the appropriate wavelength for a particular experiment can be chosen so that a wider range of d-spacing can be detect and different minerals. Any problems related to fluorescence and absorption are eliminated. These advantages have guided the development of specialized techniques such as energy dispersive X-ray diffraction.

Energy dispersive diffraction (EDD) was first demonstrated by Geissen [49] in 1968. The EDD is based on Bragg's equation:

$$n\lambda = 2d\sin\theta \tag{3.6}$$

where the wavelength, λ, is variable and the angle of diffraction relative to the crystalline

surface, θ, is fixed (but adjustable). The letter n is an integer, the factor 2 is the result of the diffracted radiation successively passing twice across the space between adjacent planes in the crystal and d is the atomic spacing. The atomic spacing information is obtained from measuring the energies of diffracted photons giving rise to a diffraction pattern dispersed in energy. Energy, E, relates to λ by h, Plank's constant and c, by:

$$E = \frac{hc}{\lambda} = \frac{12.3986}{\lambda}\text{keV} \tag{3.7}$$

Combining Eq. 3.6 and 3.7 the energy-dispersive relation is obtained:

$$Ed\sin\theta = \frac{hc}{2} = 6.1992\text{keV} \tag{3.8}$$

The energies of the diffracted photons are determined and counted by an energy discriminating detector located at a fixed angle. The diffraction spectrum from each detector comprises 4000 energy channels, with the channel width about 0.03keV.

There is a linear relationship between data collection channel numbers and photon energy. This relation is given by a equation described by the energy calibration: $E = ax + b$, where x is the channel number and a and b are the calibration coefficients obtained from characteristic fluorescence lines from various elements.

Conventional powder X-ray diffraction in time and/or temperature-resolved mode is an experimental technique to study solid-state kinetics and crystalline materials [122]. On the other hand EDD was used to monitor in situ, bulk samples while hydrating at elevated temperatures [28, 104]. The technique eliminates the need for quenching and work-up, during which the sample may undergo significant and indeterminable structural changes. Thus, it allows the direct observations of crystalline intermediate phases and their subsequent transformation into the product phase. Its application in the area of cement chemistry has proved particularly useful for detecting and monitoring structural changes and transformations in situations where conventional laboratory diffractions methods do not provide the required penetrating radiation, nor do provide sufficient time and resolution [27].

3.3 Experimental

3.3.1 Station 16.4

Synchrotron energy-dispersive diffraction (EDD) experiments were carried out on beam line 16.4 at the Synchrotron Radiation Source at Daresbury Laboratories, UK. The Synchrotron Radiation Source (SRS) at Daresbury is a low emittance storage ring which runs with an electron beam energy of 2GeV and stored beam currents in excess of 200mA [25]. Station 16.4 receives hard X-rays from a superconducting wiggler magnet positioned in straight 16 of the ring. The wiggler magnet is a three-pole device with an on-axis peak filed of 6T and return fields about 1.2T [25]. X-rays travel from the synchrotron, along an evacuated beam pipe, to the hutch. The beam pipe ends inside the experimental enclosure with a water-cooled, 0.1mm thick aluminium window, which is connected to the station front end by flexible bellows.

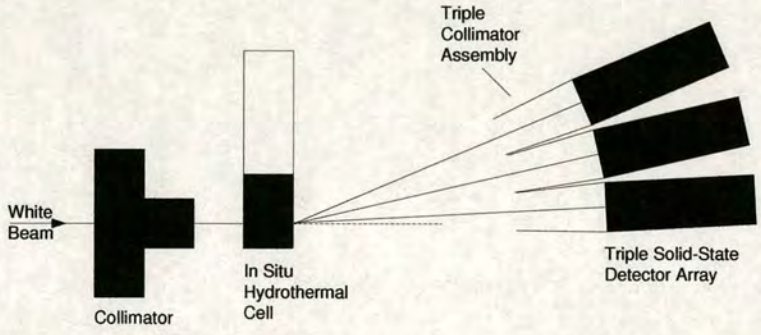

Figure 3.1: *Schematic diagram of the 3-element detector at Station 16.4 [95].*

A detailed description of the experimental enclosure is given by Clark [25]. The incident X-ray beam is shaped by a circular pinhole to 0.50mm diameter, and diffracted X-rays then reach the detector at fixed angles via flat plate collimators. The energy-dispersive method is a fixed geometry technique, with the incident and diffracted X-ray beam defined by the collimator system; the diffracted signal originates from a precise region named *a lozenge*. This region can be adjusted from $3mm^3$ to $10{,}000\mu m^3$ by adequate manipulation of the X-ray beam slits, collimation system and diffraction angle. Recently, a unique three-angle energy-dispersive detector has been successfully commissioned at station 16.4 [28]. This allows simultaneous data acquisition at three 2θ angles and it covers a greater range of reciprocal space (d - spacing). The detector unit consists of three germanium crystals, housed behind a thick beryllium window. The acquisition hardware is located behind the crystals.

3.3.2 Chemistry

Two reactions of high interest to cement hydration were observed:

1. Direct synthesis of calcium alumino-monosulphate hydrate. To synthesize monosulphate, a calcium sulphate solution was prepared by mixing 0.77g of AR hydrated calcium sulphate and 10g of deionised water. The solution was then added to a suspension of calcium hydroxide and aluminium hydroxide obtained by mixing 1g of CH and 0.69g AH with 10g of deionized water. The molar ratio CH:AH:$C\bar{S}H_2$ used was 3:2:1 (Table 3.1).

2. Ettringite stability in the presence of NaOH and temperatures up to 150°C. The sample of ettringite used here was prepared by dispersing 1g of AR calcium hydroxide and respectively dissolving 1.42g of aluminium sulphate 16-hydrate in 28.56g NaOH solution 0.5M or 1M. The mixture was rather granular and very fluid (low viscosity). Experiments at alkalinities of 0.25M and 0.75M respectively, were also carried out. Due to problems associated with the beam line (beam dump, beam injection, etc.), the outcome of these tests did not become fruitful.

No.	Formulations	Molar	No. patterns x collection time (min)	T/°C	Ramp/$^{\circ}min^{-1}$
1	$C\bar{S}H_2$	-	1 x 2	30	-
2	CH:AH:$C\bar{S}H_2$	3:2:1	30 x 2	150	2
3	CH:AH:$C\bar{S}H_2$	3:2:1	150 x 2	cooling to 30	-
4	CH:$A_2\bar{S}_3H_{16}$ in 0.5M NaOH	1:6	62 x 2	150	1
5	CH:$A_2\bar{S}_3H_{16}$in 1M NaOH	1:6	62 x 2	150	1

Table 3.1: *Reagents and proportions used in EDD experiments. The experiment no.1 represents the control sample, which will be subsequently used to optimize the calibration data file. For this purpose an anhydrous sample of gypsum will be used. The following experiments investigate monosulphate and ettringite stability as proposed above.*

3.3.3 Procedure

The samples were mixed outside the synchrotron beam, following the proportions described in Table 3.1. Each sample was loaded into a reusable autoclave cell (o.d. 12.5mm, i.d. 8mm) machined from the engineering polymer polyetheretherketone (PEEK).

The PEEK was chosen because of its resistance to high pH and low X-ray absorption. The autoclave cells were designed such that the can could withstand heating up to 200°C and 15bar internal pressure. The cell was sealed using a brass plug and Viton 'o' ring and then placed in a temperature-controlled furnace on the beam line (Fig. 3.2a).

The furnace is cylindrical and contains a heating element at the bottom and a rotation fan at the top which ensures a homogenous temperature within the cavity. The sample is mounted to intersect the X-ray beam and rotates at 60 revolutions min^{-1} about the cylinder axis to improve sampling statistics. Light sensitive paper was used to track the beam as it moved along the sample, in order to check the position at which the beam hit the sample and to ensure that the system was correctly aligned. The oven is fitted with a temperature ramp and hold programme. The sample temperature is monitored by a thermocouple inserted into the brass plug. Both the heating element and the thermocouple were connected to a temperature controller, working with an accuracy of $\pm$ 0.1°C. Any thermal losses were minimized by a double metallic wall separated by a layer of insulating material (see Fig. 3.2b). The beam passage to and from the sample was allowed by the two existent holes, on either sides of the furnace.

(a)

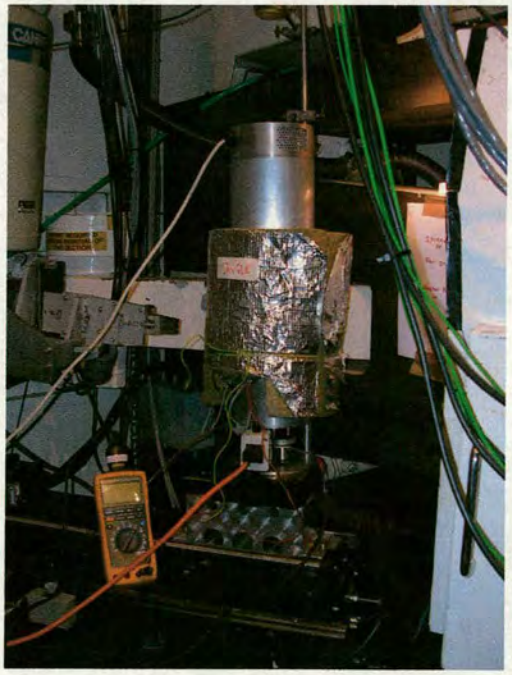

(b)

Figure 3.2: *(a) Autoclave cell machined from polymer polyetheretherketone (PEEK) (b) The Schlumberger furnace used for reactions under hydrothermal conditions.*

The principle of EDD method used in this work is described elsewhere [27] and a schematic diagram is provided in Fig. 3.3. The time delay between the start of reaction and start of data collection is usually about 5min. The data acquisition time for a single diffraction pattern was 120s (Table 3.1). The time to acquire a series of patterns from a single sample spanned a couple of hours. Repeat analysis of some samples were made to check the reproducibility of the experiments.

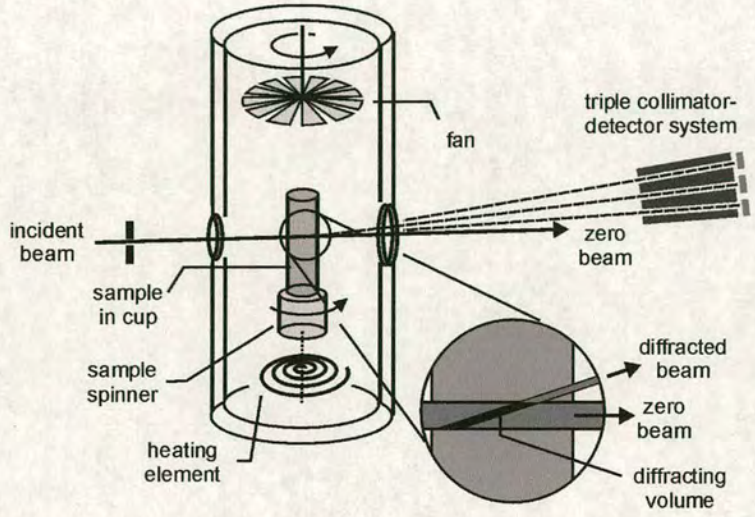

Figure 3.3: *Representation of the principle of EDD experiment operating with an autoclave hydration cell. Furnace main features are also showed: heating element, fan, thermocouple and PEEK cell [27].*

3.4 Results and discussion

Fig. 3.4 shows the powder diffraction pattern of gypsum, $C\overline{S}H_2$, constructed from data acquired by the three separate fixed-angle detectors. The energy-dispersive detectors allowed simultaneous data acquisition at three 2θ angles: 1.788, 4.554 and 7.477°, respectively. The pattern was obtained from a powder sample in a single 120s measurement in order to optimize the calibration data file of the following experiments. Typical d-spacing corresponding to $C\overline{S}H_2$ were identified by tick marking pattern no. 33-311 from ICDD (International Centre for Diffraction Data).

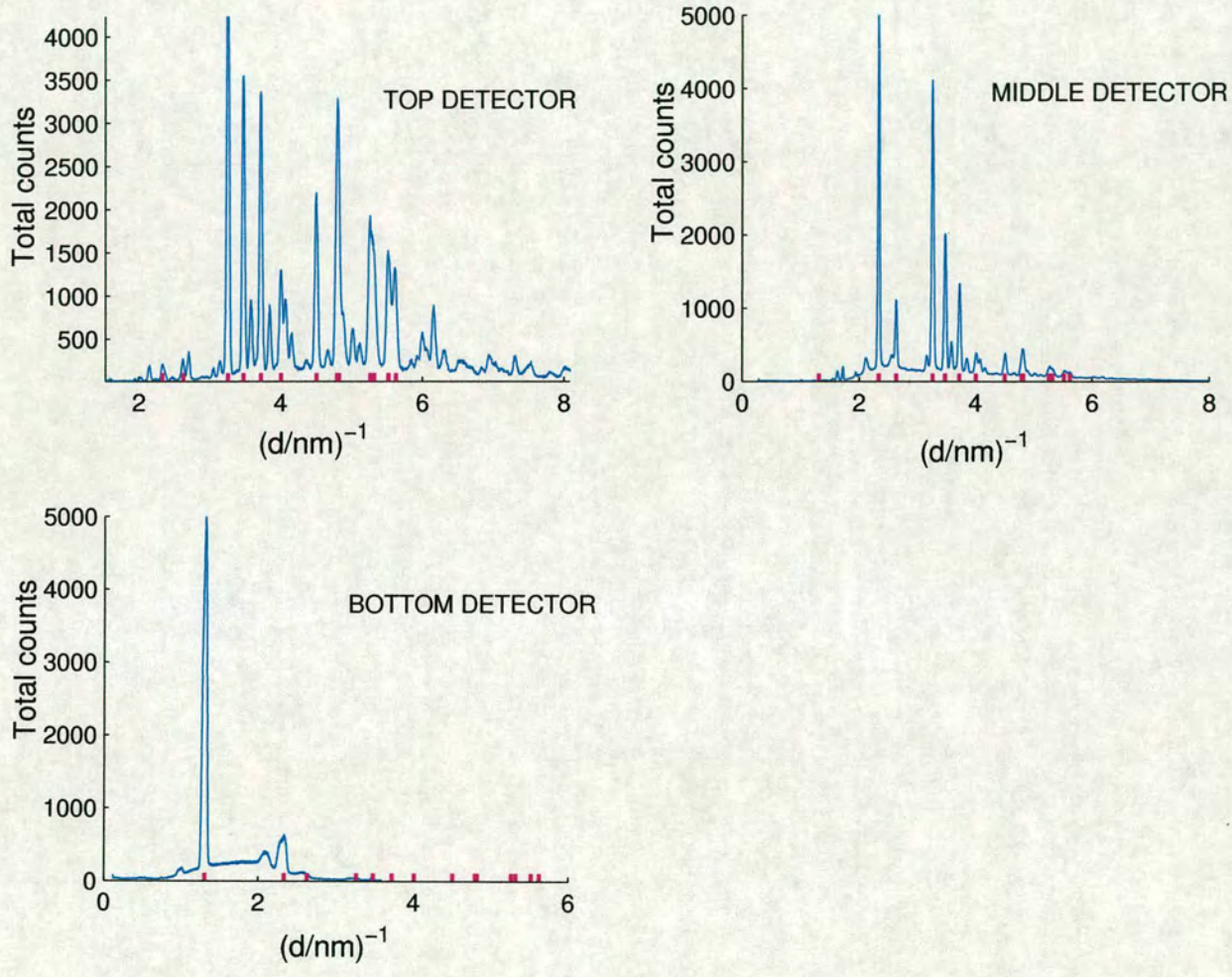

Figure 3.4: $C\bar{S}H_2$ *patterns collected from top, middle and bottom detectors to optimize the calibration. The detectors were positioned at 2θ angles: 1.788, 4.554 and 7.477°, respectively. Tick marks in red represent characteristic reflections for gypsum according to ICDD.*

3.4.1 Direct synthesis of calcium alumino-monosulphate hydrate

The synthesis method used in laboratory preparation of monosulphate hydrate was observed *in situ* (chapter 2, section 2.4.3). The progress of the reaction was tracked over 6h (Fig. 3.5). The temperature was ramped from 30 to 150°C at a rate of $2°min^{-1}$. On cooling, no ramp was set, the sample and the oven were left to cool naturally to room temperature whilst scanning. A data acquisition time of only 120s was used throughout the experiment. After 5min of mixing, ettringite is found to co-exist with gypsum reflections (1/d 3.262 (041), $2.334nm^{-1}$ (021)). Ettringite (104) and (114) reflections (1/d 2.124, $2.578nm^{-1}$) are observed from the first pattern immediately after mixing. The reaction progresses with a steady growth in ettringite until all hydrated calcium sulphate goes completely into solution, at 75°C±1, as its solubility increases with increasing temperature. At temperatures below 75°C, the following phase assemblage is observed: AFt + $C\bar{S}H_2$. An important observation is that crystalline ettringite forms almost immediately due to high sulphate/aluminate ratio even though the stoichiometric composition corresponds to monosulphate. The estimate of the temperature error is ±1°C.

At 114°C we observe ettringite decomposition, its intense (100) reflection is replaced by a new one which match the basal reflection (003) of monosulphate 14-hydrate at 1/d 1.047 nm^{-1} (Fig. 3.6). The monosulphate with basal spacing of 1/d 1.047 nm^{-1} is the 14-hydrate and not the 12-hydrate usually reported. This result is consistent with the early work on thermal decomposition of ettringite at a calculated water vapour pressure of 1.63bar [59]. The gypsum acts as a transient intermediate in the decomposition. Bassanite (calcium sulphate hemihydrate) is also observed as a decomposition product; the gypsum reflection (014) at 1/d 2.334 nm^{-1} disappears and (022) bassanite reflection reforms at 1/d 3.287 nm^{-1}(Fig. 3.5). An important observation is that the 1/d 3.287 nm^{-1} bassanite formed is stable throughout the experiment.

Ettringite becomes hydrothermally unstable at elevated temperatures, part of the sulphate is quickly removed from the ettringite structure and monosulphate is formed. When the temperature is ramped even higher, the AFm monosulphate hydrate formed on decomposition of ettringite is stable up to the maximum experimental temperature of 150°C. At 150°C AFm 14-hydrate co-exists with bassanite. An increase in temperature does not induce further changes to the stable hydrate assemblages. The same thermal decomposition sequence was reported by Satava and Veprek [117], who studied ettringite decomposition in autoclave conditions up to 232°C. They also reported the stability of monosulphate 14-hydrate up to 190°C.

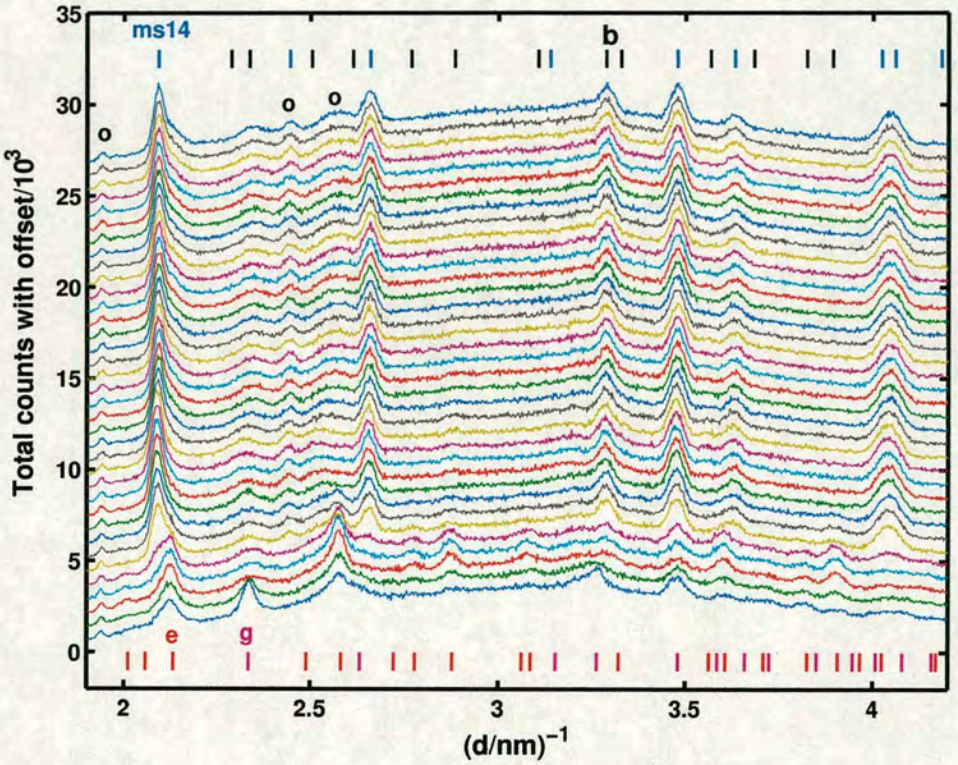

Figure 3.5: *Thermal synthesis of* AFm. *Synchrotron diffraction patterns illustrating mineral changes over 6 h. 180 patterns were collected at 2 min interval as the temperature was ramped from 30 to 150°C at 2°min^{-1} and then the sample was naturally cooled to ambient temperature. These patterns are collected by the middle detector (2θ = 4.554°). Here every 5th successive pattern is shown. Key: o = peek polymer cell;* ***e*** = $C_6A\overline{S}_3H_{32}$; ***g*** = $C\overline{S}H_2$; *ms-14* = $C_4A\overline{S}H_n$; *b* = $C\overline{S}H_{0.5}$.

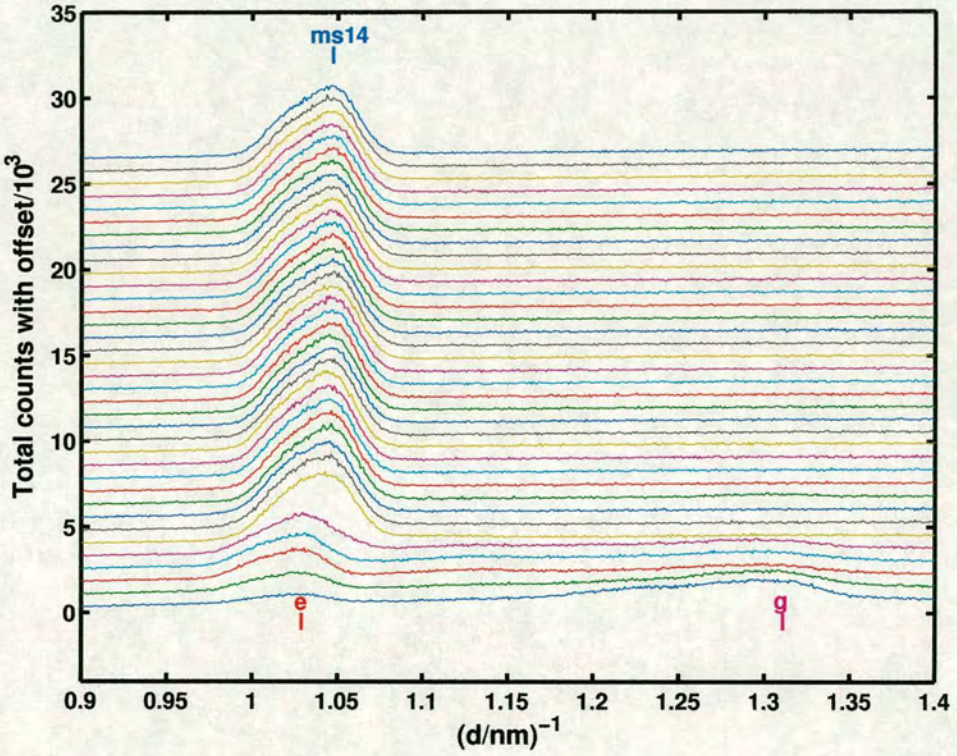

Figure 3.6: *Plot of overlapping ettringite (100) (1/d 1.028 nm^{-1}) and monosulphate (003) (1/d 1.0471 nm^{-1}) over the temperature interval from 30 to 150°C and reverse on cooling to ambient temperature. The peak at 1/d 1.310 nm^{-1} is the 020 gypsum reflexion. These peaks are collected by the detector set at the lowest angle (2θ = 1.788°). Key: e = $C_6A\overline{S}_3H_{32}$; g = $C\overline{S}H_2$; ms-14 = $C_4A\overline{S}H_n$.*

On cooling over 5h to ambient temperature, no disproportion to reform ettringite was observed. Monosulphate 14-hydrate is a stable phase at ambient temperature and 100% relative humidity, even if the low sulphate form is known to be unstable in water at 30°C [51]. Ghorab *et al.*[52] have described the chemistry of changes of mortars (cured at elevated temperatures) after cooling at ambient temperature. They reported that the monosulphate formed after the heat treatment decreases and ettringite reforms, in contradiction with our findings whereby monosulphate 14-hydrate seems to be the stable phase on cooling from elevated temperature. However other investigations confirm our results, namely those where cements high in C_3A or lower in sulphate were used. In these situations monosulphate is stable at room temperature [43].

3.4.2 Thermal stability of ettringite in alkaline solutions up to 150°C

The effects of temperature and NaOH concentration on the formation and stability of ettringite were established by hydrating CH and $A_2\overline{S}_3H_{16}$ in 0.5 and respectively 1M NaOH at temperatures from 30 to 150°C.

3.4.2.1 Hydration of CH + $A_2\overline{S}_3H_{16}$ in 0.5M NaOH solution

The presence of alkali contributes to the hydroxyl concentration both in pure phase systems and real cements. The pH variation as a function of sulphate concentration is particulary relevant to the stability of ettringite. Modifications of the activity coefficients takes place due to the variation in the ionic strength. Thus, a displacement of the equilibrium curve is induced and stability fields are modified [30, 31]. An increase in temperature is also likely to modify the phase diagram as the solubility products vary with the temperature.

According to the work presented here the ettringite stability at 30°C is not affected by the presence of dilute alkaline solutions (Fig. 3.7). The data in Fig. 3.7 illustrate the synchrotron diffraction patterns of ettringite formation at temperatures up to 150°C in an alkaline environment of 0.5M NaOH solution. The temperature was ramped from 30 to 150°C at a rate of $1°min^{-1}$ and 62 patterns were collected every 2min for 2h. While increased temperature may decrease ettringite stability, hydration at elevated temperatures (up to 80°C) does not preclude the ettringite formation.

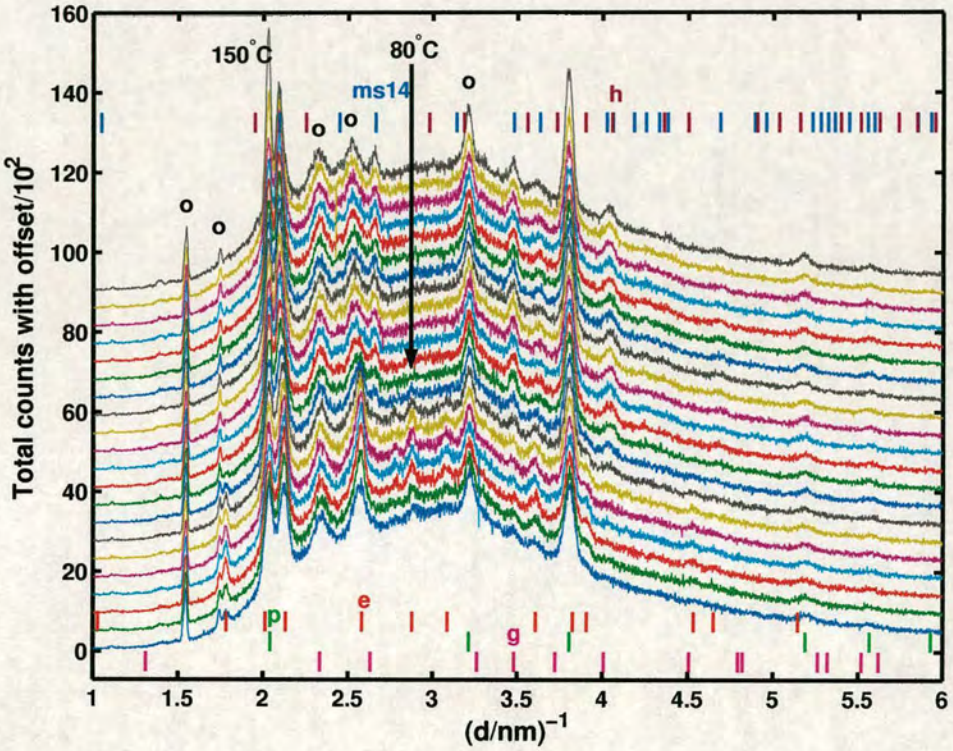

Figure 3.7: *Ettringite thermostability in 0.5 M NaOH. Synchrotron diffraction patterns illustrating mineral changes over 2 h. 62 patterns were collected at 2 min interval as the temperature was ramped from 30 to 150° C at 1° min^{-1}. Here every 3rd successive pattern is shown. Key: o = peek polymer cell; p = CH; g = $C\bar{S}H_2$; ms-14 = $C_4A\bar{S}H_n$; h = C_3AH_6.*

Ettringite was found to be the dominant crystalline phase over the temperature range from 30 to 80°C and 0.5M sodium hydroxide. The nature and sequence of appearance of the new phases at 30°C were the same as for water where the stable phases are CH, AFt and $C\bar{S}H_2$. When CH and $A_2\bar{S}_3H_{16}$ is hydrated in 0.5M NaOH solution, the ettringite reflection ($\bar{1}04$) at 1/d 2.125nm^{-1} is observed within 5min of initial contact with the solution. The reflections at d-spacings of 2.623 and 2.869nm (1/d 3.805 and 3.489nm^{-1} respectively) correspond to CH (101) and $C\bar{S}H_2$ (-221).

The effect on hydration of sodium and sulphate ionic species depends on their concentrations [24]. At equivalent sodium concentrations, AFt is preferred at high sulphate concentrations. If the Na content increases Ca is depressed while Al and especially SO_4 are increased. The effect of alkali and elevated temperature together increase the SO_4 solubility even further so that at 85°C±1 we state the following phase assemblage: AFm + CH. These results support the calculations made by Damidot and Glasser [31], which indicate that AFt becomes more soluble with increased temperature and alkali concentrations. The study also indicates that sodium will not be incorporated into the solid phase. This assemblage stands in the most complex ordinary portland cements (OPC) [3].

As the hydration reaction proceeds and the temperature reaches 75°C, at pattern 22, two new reflections are observed to grow (Fig. 3.8). These correspond to AFm at 1/d 2.656 and 4.046nm^{-1} respectively. At this point AFt and AFm co-exist as it was previously observed [113]. At pattern 25 corresponding to 80°C±1, the ettringite reflection ($\bar{1}04$) at 1/d 2.125nm^{-1} disappears and AFm (006) is observed at *d*-spacing of 4.779nm, 1/d 2.092nm^{-1}.

At increasing temperature, the AFm becomes the destination of all sulphate thus the $C\bar{S}H_2$ (-221) reflection at 1/d 3.489nm^{-1} disappears and AFm (110) forms at 1/d 3.475nm^{-1} while the ettringite (212) at 1/d 2.878nm^{-1} completely disappears. The week reflection of ettringite (304) is also replaced by AFm (113) with a d-spacing of 2.756nm. The portlandite reflection (101) at 1/d 3.805nm^{-1} is observed throughout the experiment.

After 50min of hydration ettringite converts entirely to monosulphate. The stability of monosulphate hydrate is enhanced in an alkaline environment at increasing temperature. Generally the AFm is increased with increasing temperature above 80°C, indicating an increasing amount of AFm.

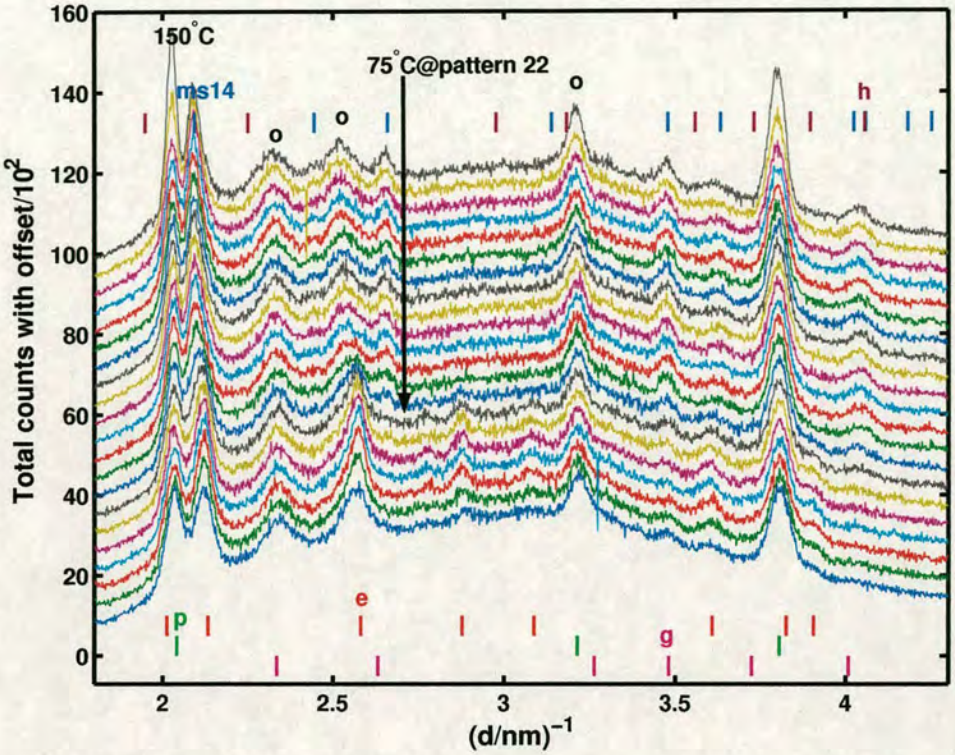

Figure 3.8: *Expanded plot; ettringite thermostability in 0.5 M NaOH. Key: o = peek polymer cell; p =* CH*; g =* $C\bar{S}H_2$*; ms-14 =* $C_4A\bar{S}H_n$*; h =* C_3AH_6.

Fig. 3.9 shows the peak area of the principal Bragg peaks during hydration, each peak having been fitted to a single gaussian function.

The sequence of events on ramping the temperature at 1°C min^{-1} from 30 to 150°C begins with a initial rapid reaction to form ettringite. At around 80°C and 50min after mixing ettringite is replaced by AFm. At the same time, gypsum is largely consumed as its peak area decreases. A striking observation is that at temperatures approaching 130°C, the portlandite CH peak area shows a minima followed by an abrupt increase while the temperature is approaching 150°C. A further increase in temperature does not affect the phase relations and at 150°C we report the following stable phase assemblage: CH + AFm. However, the decomposition of the low sulphate form to C_3AH_6 was not observed in those conditions as predicted in the study of Ghorab and Kishar [51].

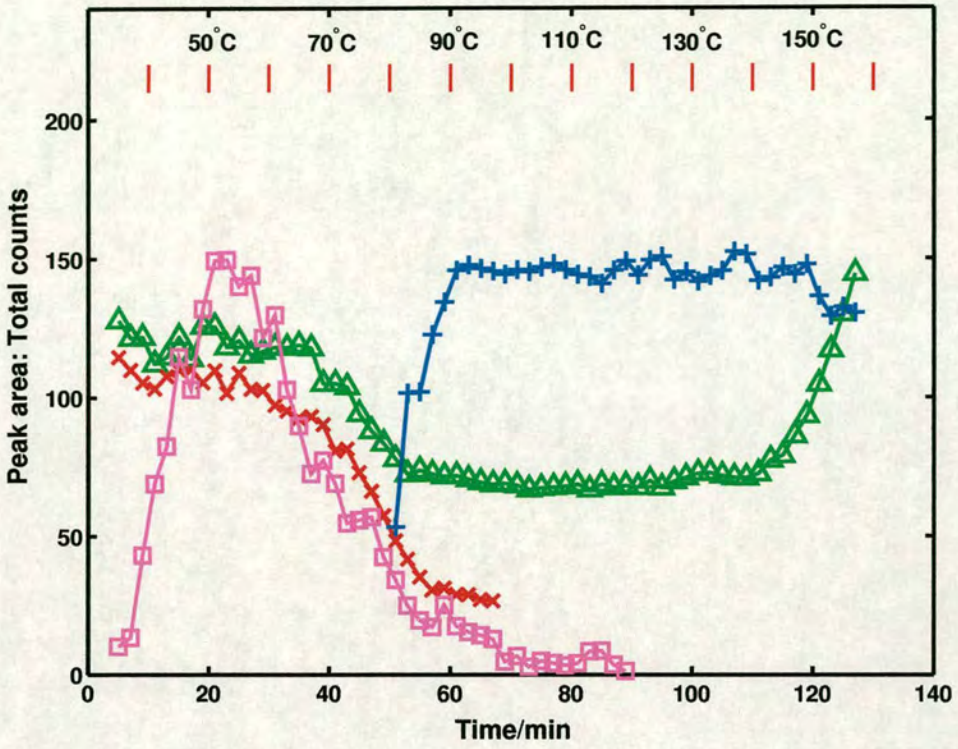

Figure 3.9: *Peak areas over time and increasing temperature showing gypsum (-221) (1/d 3.489 nm^{-1}) (□) , potlandite (101) (1/d 3.805 nm^{-1}) (△), ettringite (104) (1/d 2.132 nm^{-1})(×) and ms14 (006) (1/d 2.092 nm^{-1}) (+).*

Clark and Brown [24] state no observation of potlandite CH and calcium sulphate $C\bar{S}H_2$ when tricalcium aluminate and $C\bar{S}H_2$ are hydrated on 0.5 M NaOH and temperatures up to 90°C. They also found as predominant phases after hydration a sodium (U-phase) and carbonate - substituted AFm which strongly contradicts this work and the predictions of Damidot and Glasser [30]. The thermodynamic calculation of phases stability was established using the geochemical code PhreeqC [23].

The phase assemblages were predicted using solubility products reported by Damidot and Glaser [31] and Reardon [114] at 25°C. A synthesis of these results could be found in the Appendix (Table A.2). Both sets of input data predict the phase assemblages observed in this work.

3.4.2.2 Hydration of CH + $A_2\overline{S}_3H_{16}$ in 1M NaOH solution

When ettringite formation takes place in more aggressive conditions of alkalinity (up to 1.0M NaOH solution) and elevated temperatures more complex assemblages are observed. The synchrotron diffraction patterns of ettringite synthesis are shown in Fig. 3.10, for temperatures up to 150°C and a alkaline environment of 1M NaOH. 62 patterns were collected every 2min for 2h, while the temperature was ramped from 30 to 150°C at a rate of $1°min^{-1}$. In spite of the retarding effect of NaOH/KOH [17, 23], at 30°C ettringite stability does not seems to be affected in 1 M NaOH. From Fig. 3.11 the following phase assemblage is reported at ambient temperature: CH + AFt + $C\overline{S}H_2$. Typically, ettringite formation is preferentially favourable when the pH and alkali/hydroxyl concentrations are depressed [17].

Interpretation of the stability of ettringite based on the data reported by Hampson and Bailey [60] and Brown [17] strongly suggest that the upper stability limit for ettringite is in the pH range above 12.5 in a cementitious system. Thermodynamic calculations by Damidot and Glasser [31] suggest that the presence of soda extends the stability region to a lower pH limit of 10.7 or even perhaps as low as 10 at 125mM/L of NaOH while at the same time expanding the upper stability limit from 12.5 to about 13 over the same range of soda additions. These data agree with the experimental data presented here which demonstrate that ettringite is indeed stable over the study conditions from 30 to 75°C.

Strong reflections of CH (001), AFt (104) and $C\overline{S}H_2$ (-221) are observed after approximately 5 min after reaction at d-spacing 4.927, 4.710 and 3.481nm (1/d 2.029, 2.123 and $3.481nm^{-1}$ respectively). However ettringite dissolution is enhanced at elevated temperatures. With increased temperature incorporation of sodium in the solid phase takes place and a sodium-substituted AFm, referred to as 'U-phase', was observed as a transient hydration product. These findings are in agreement with prior work of Shimada [123], who found ettringite to convert to 'U-phase' during heat treatment at 80°C in NaOH solutions above 0.25M. The intensity of AFt (104) decreases slowly while an intermediate phase is formed at 4.456nm (1/d $2.243nm^{-1}$, pattern 10). This corresponds to the (103) 'U-phase' ($C_4A\overline{S}_{1.5}N_{0.5}H_{15}$), which was first reported by Dosch and Strassen in 1968 [39]. A distinctive (106) reflection is observed at 3.528nm (1/d $2.833nm^{-1}$). In particular 'U-phase' formation was found to cause expansion [81]. The ettringite initially produced is increased even when the 'U - phase' formation took place.

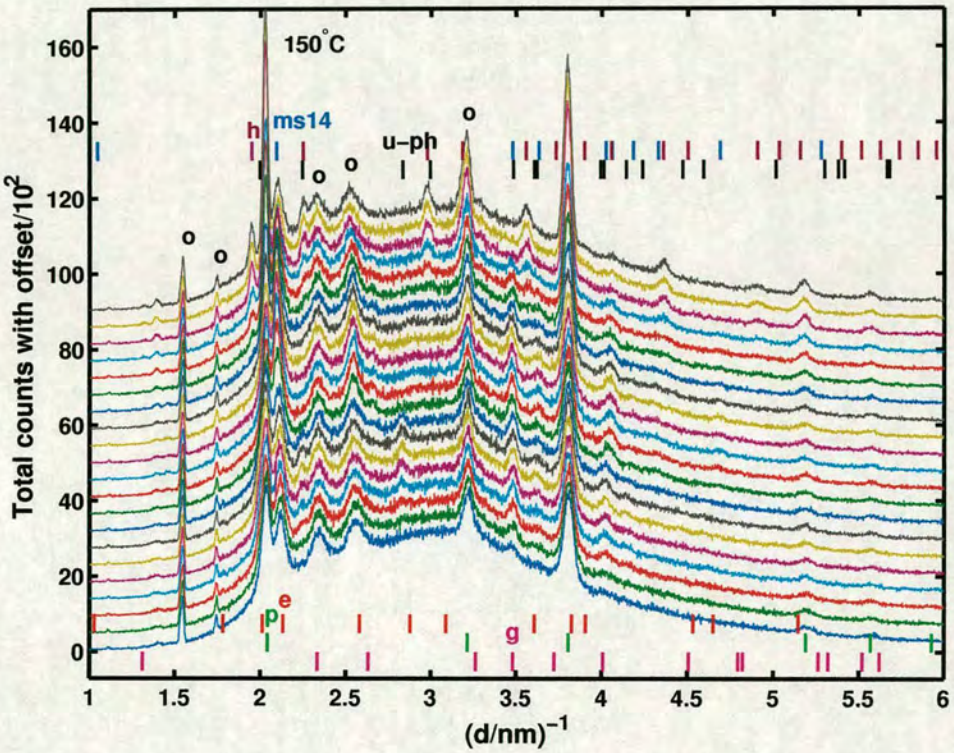

Figure 3.10: *Ettringite synthesis at 150°C in 1 M NaOH. For reason of clarity, only one in every three diffraction patterns is shown. The experiment was ramped over 2 h and held for 5 min at the final temperature. 62 patterns were collected, one every 2 min. Key: o = peek polymer cell; p = CH; g = $C\bar{S}H_2$; ms-14 = $C_4A\bar{S}H_n$; h = C_3AH_6; u-ph = $C_4A\bar{S}_{1.5}N_{0.5}H_{15}$.*

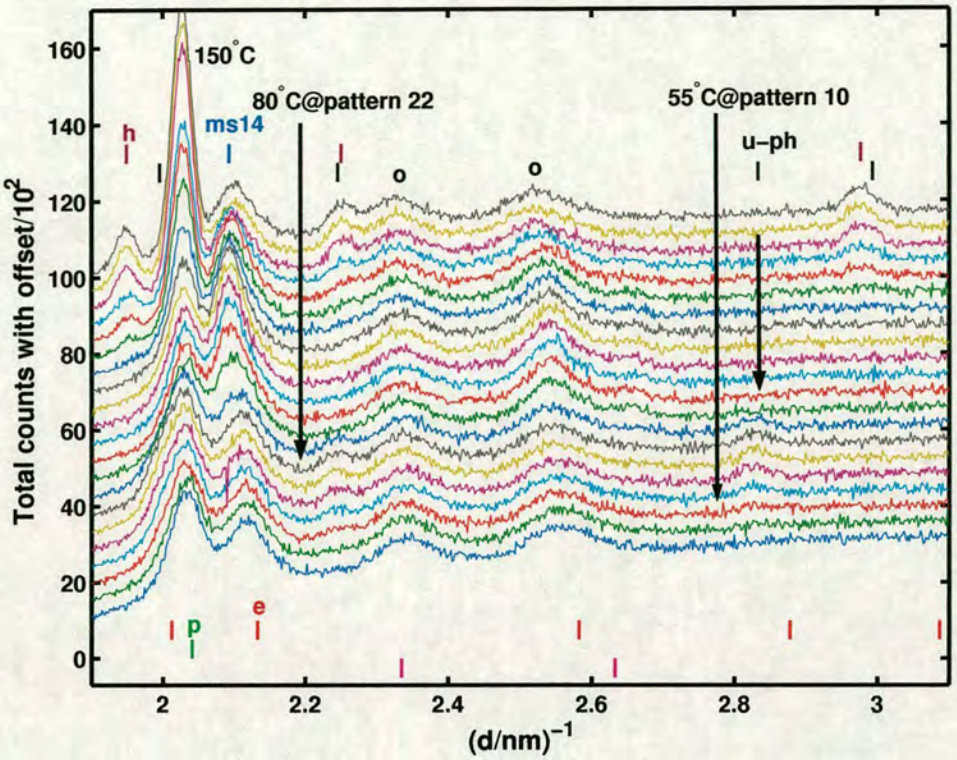

Figure 3.11: *Expanded plot of ettringite synthesis at 150°C in 1 M NaOH. Key: o = peek polymer cell; p = CH; g = $C\overline{S}H_2$; ms-14 = $C_4A\overline{S}H_n$; h = C_3AH_6; u-ph = $C_4A\overline{S}_{1.5}N_{0.5}H_{15}$.*

At 55°C the 'U - phase' co-exists with CH, AFt and AFm. Synchronously the (1,0,10) AFm peak is observed to grow at 2.489nm (1/d 4.017nm^{-1}), being subsequently replaced by (431) C_3AH_6 at 2.461nm (1/d 4.056nm^{-1}) at 80°C. This suggests that the AFm is a metastable phase with respect to C_3AH_6 for low sulphate concentration. The presence of a cationic species seems to accelerate AFm formation, as has been observed already at 55°C in this work and to promote its stability in the phase assemblage.

At pattern 22 the main ettringite reflection (104) at 1/d 2.123 nm^{-1} is replaced by AFm (006) with a *d*-spacing of 4.778nm while the temperature raises to 80°C±1. The 'U - phase' peaks are no longer observed above 80°C. The CH (001) reflection continues to be observed throughout the experiment. The following phase assemblage was found at 85°C: C_3AH_6 + AFm + CH, consistent with previous work [30, 31]. For this assemblage Atkins *et al* [3] have calculated a corresponding $SO_{4aq.}$ concentration of 193mM/L at 85°C and 1M/L NaOH.

When the temperature is ramped even higher, to 150°C, the overall phase assemblage stays the same but with a significant change in solution composition. Above 130°C, C_3AH_6 become the dominant phase as a result of AFm decomposition. New C_3AH_6 reflections (211, 220, 321, 420, 521) are observed at 5.133, 4.444, 3.359, 2.811, and 2.294nm (1/d 1.948, 2.252, 2.977, 3.558 and respectively 4.358nm^{-1}).

A decrease in peak area associated with the AFm (006) reflection can be seen in Fig. 3.12. This is accompanied by a boost in CH and augmentation of C_3AH_6 at temperatures from 130 to 150°C. However, AFm is still observed in the last pattern, whereby it is concluded that an additional increment in temperature will probably lead to complete decomposition to hydrogarnet.

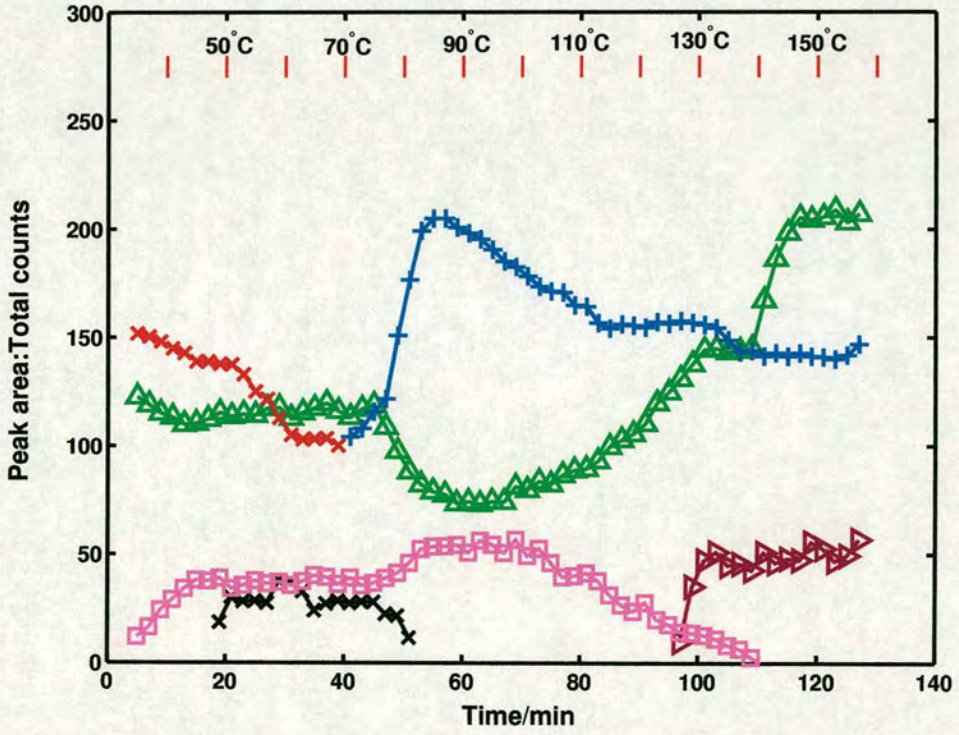

Figure 3.12: *Main peak areas over time and increasing temperature from 30 to 150° C. Areas of* AFt *(104) (1/d 2.132 nm^{-1}) (× red),* AFm *(006) (1/d 2.092 nm^{-1}) (+), C_3AH_6 (211) (1/d 1.948 nm^{-1})(◁), CH (001) (1/d 2.029 nm^{-1})(△),* $C\bar{S}H_2$ *(-221) (1/d 3.481 nm^{-1}) (□) and 'U - phase'(103) (1/d 2.243 nm^{-1})(× black).*

However, at temperatures above 80°C and lower than 100°C, AFm is a stable phase. Its stability is governed by the calcium concentration in solution and thus by a high pH. As can be seen in Fig. 3.12, from 80 to 100°C the CH (001) peak area increases following its solubility diminishment with increasing temperature and alkali contribution.

The addition of sodium causes calcium depression in solution while the aluminium and sulphate increases considerably. Both AFt and AFm phases are stabilized by high pH, which one forms depends on the sulphate concentration as there is an excess of aluminium. However elevated temperature increases the SO_4 solubility even further and so above 130°C AFm decomposition is preferred.

3.5 Conclusions

On establishing the stability of the calcium sulphoaluminate hydrate phases both types of hydrates were considered, because of the expected transformation of one type to an other under different conditions.

Direct synthesis of calcium alumino-monosulphate hydrate

1. According to the present work AFm monosulphate 14-hydrate is observed even when formulations have a stoichiometric composition of 12-hydrate.
2. The first period of reaction is always characterized by the presence of ettringite. The AFm 14-hydrate is a stable phase up to the maximum experimental temperature of 150°C. AFm and small amounts of $C\bar{S}H_{0.5}$ co-exist at 150°C.
3. On cooling to ambient temperature, no disproportion to form the high sulphate form was observed (ettringite). The product of the reaction when still moist with the mother liquor always show peaks characteristic of the monosulphate 14-hydrate structure.

Thermal stability of ettringite in alkaline solutions up to 150°C

Ettringite hydration in increasing sodium hydroxide concentrations does not induce changes to the stable hydrates assemblage. A summary of the phase assemblages identified in this work is given in Table 3.2 and explained bellow:

Phase assemblages		
+ 0.5 M NaOH	**+ 1 M NaOH**	**Temperature/°C**
CH + AFt + $C\bar{S}H_2$	CH + AFt + $C\bar{S}H_2$	30°C
CH + AFt + $C\bar{S}H_2$	'U - phase 'co-exist with CH, AFt and AFm	55°C
AFt and AFm co-exist	'U - phase 'co-exist with CH and AFm	75°C
AFm + CH	C_3AH_6 + AFm + CH	85°C
AFm + CH	C_3AH_6 + AFm + CH	150°C

Table 3.2: *Phase assemblages identified in the CaO - Al_2O_3 - $CaSO_4$ - H_2O system using Synchrotron energy dispersive diffraction method.*

1. Ettringite is stable phase at 30°C and it persists in alkaline solutions up to 1 M NaOH.

2. Ettringite formation was observed to depend upon the concentration of calcium in solution; thus the formation of calcium hydroxide and sodium-substituted monosulphate phase competes with ettringite formation.

3. Increasing temperature increases the extent of AFm formation and promotes the formation of 'U - phase'. The 'U - phase' was observed at temperatures between 55 and 80°C, conflicting with the study of Damidot and Glasser [31], which indicate that sodium will not be incorporated into the solid phase.

4. AFm is a metastable phase with respect to C_3AH_6 for low sulphate concentration.

5. Above 130°C, C_3AH_6 become the dominant phase as a result of AFm decomposition in agreement with Taylor's statements on the formation of hydrogarnet in cement pastes moist cured at 90°C for 2 months [131].

Chapter 4
Crystal growth from solution of ettringite

The aim of the work reported in this chapter is to explore the range of morphology developed by ettringite produced in different conditions with the emphasis on the temperature as an influencing factor. In particular a new cryo-SEM method is used to image the ettringite particles at high resolution and as close as possible to their natural state. The importance of investigating the ettringite morphology lies in its influence on the rheological evolution of the cement slurry at early times, as it will be shown in Chapter 5.

4.1 Introduction

Ettringite is a hydrous calcium alumino-sulphate mineral represented by the formula $C_6A\overline{S}_3H_{32}$. According to Bannister [7] *et al.*, the natural mineral ettringite is found very rarely in nature and was originally discovered as transparent acicular crystals lining the cavities of metamorphosed limestone inclusions. Ettringite is formed during the initial stages of hydration of portland cement containing small amounts of gypsum as a source of soluble sulphate. When gypsum is consumed, most of the ettringite transforms to aluminium monosulphate hydrate ($C_4A\overline{S}H_{14}$) [48]. Ettringite and monosulphate hydrate are in equilibrium as long as no external source of sulphate is available. In marine structures or structures in contact with different formation waters containing high levels of sulphate, the monosulphate hydrate reverts back to ettringite, causing expansion and cracking of the structure [85].

Ettringite formation is an important reaction in cement hydration [87]. Its growth during early stages of hydration of normal portland cements is generally believed to be responsible for the prevention of quick setting [86] which, in the absence of gypsum ($C\overline{S}H_2$) in cements, could occur because of the precipitation of calcium aluminate hydrates. Furthermore, ettringite is believed to cause destructive expansion which occurs in portland cement concrete when it comes in contact with aggressive formation waters.

However, the precipitation of ettringite in the early stages of hydration does not promote any expansion because the cement paste matrix is very porous and flexible, instead it contributes to early strength of concrete [64, 67]. Because ettringite has a high water content of 46% by weight, its formation affects the consistency and workability of cement. Its morphology is also found to produce changes in the rheological behaviour of cement (Chapter 5). At later stages the matrix becomes rigid and brittle and cannot accommodate the expansion [131]. Ettringite is believed to produce the expansive forces typically attributed to factors such as crystal growth, varied hydration, and/or adsorbed crystal surface water.

Numerous theories and models explaining the mechanism of ettringite formation and its expansion were grouped in two schools of thoughts: the crystal growth theory and the swelling theory. According to the first, expansion is caused by the growth of ettringite crystals which form on the surfaces of the expansive particles or in pore space solution. The growth of these crystals causes crystallization pressure and hence expansive forces. According to the second school, expansion is caused by swelling of the ettringite particles which are of colloidal size. These particles are commonly referred to as a gel. The gel has a large specific area and takes up water to produce overall expansion by swelling. However a major disagreement exists between the two schools [26]. According to the first school, hydration is more favorable and quicker in the presence of lime and ettringite formation is a topochemical mechanism. According to the second school ettringite always forms in a through-solution mechanism. Recent investigations on ettringite formation acknowledge a through-solution mechanism by inter-diffusion of calcium and aluminate ions moving through solution away from the source mineral [89]. A review of literature on sulphoaluminate cements, shows that understanding of the morphology of ettringite formation remains a controversial issue [26]. Most of the studies of the mechanism of ettringite formation were focused to explain the expansion characteristics of expansive cements and lack a common opinion about the growth mechanism. Therefore, this study will be focused mainly on the mechanisms of crystal growth as processes which govern the crystal morphology. The $C_6A\overline{S}_3H_{32}$ produced from undersaturated solutions with respect to portlandite and calcium sulphate, presents itself as long slender, needle-shaped crystals [80, 86]. However in the concrete systems $C_6A\overline{S}_3H_{32}$ is formed under conditions of supersaturation. Replicating those conditions Mehta [86] concluded that ettringite crystals formed under supersaturation conditions are no longer slender needles but rather short prisms, probably hexagonal in cross-section, with a thickness-length ratio of about 1:3.

Most past studies of ettringite involved the reaction of cement components with water; here simple inorganic compounds have been used in order to isolate and study only the reaction pertaining to the nucleation and growth of ettringite as follows:

$$6CH + A_2\overline{S}_3H_{16} + 10H \Rightarrow C_6A\overline{S}_3H_{32} \tag{4.1}$$

It is the purpose of this work to further investigate the difference in morphology of ettringite, grown from laboratory reagents portlandite (CH) and aluminium sulphate ($A_2\overline{S}_3H_{16}$), versus cementitious phases. Two main processes are known to govern the crystal growth [70]. The first consists of the diffusion of particles to the surface of a growing crystal before their incorporation in the crystal lattice. The second process can be divided into several stages: adsorption of the particles by the surface, migration along the surface and finally incorporation in the lattice. Crystallization conditions and the nucleation process are governed by factors such as temperature, degree of supersaturation of the solution, pH, viscosity of the solution, rate of stirring, presence of impurity, etc [109]. Temperature influence on the growth of crystalline ettringite, hence on its morphology will be explored in this study.

4.2 Theoretical aspects on crystal growth from solution

Formation of a crystal from solution is governed by three important stages as shown schematically in Fig. 4.1.

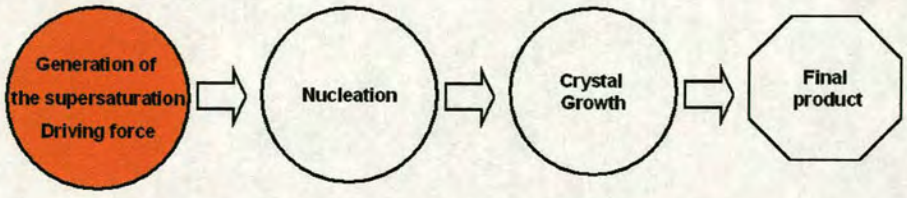

Figure 4.1: *Main stages of crystal formation from solution.*

A crystalline material is a three-dimensional pattern of atoms, ions, or molecules, having fixed distances between constituent parts. The formation of crystalline material may occur from a melt, from a gaseous phase, from a supercritical fluid or from solution [94]. The most important requirement for crystallization is supersaturation, which is the driving force for nucleation to occur [33]. Typically a solution is described in terms of the concentration of its components.

In order for precipitation to take place, the solution has to be supersaturated [97].

The supersaturation can be achieved by a number of methods [70] such as:

1. method that uses the temperature dependence of the solubility. In practice the solubility of most substances increases with rising temperature. If such solution is gradually cooled, its solubility decreases and hence the solution becomes supersaturated.

2. method which involves the removal of a solvent at constant temperature. This method can be applied to any substance and involves ordinary evaporation. The evaporation of the solvent is known to increase the concentration of a solute in a solution and this results in a supersaturation.

3. method based on the use of chemical equilibrium between substances. In practice the supersaturation is achieved by this method by mixing two or more solutions of relatively dissolved substances. The new compound formed by a chemical reaction has a concentration higher than its solubility in a given substance, hence the solution becomes supersaturated with respect to the new compound.

4. method which involves introducing into the solution some substance which reduces the solubility of the solute. The formation of precipitates by the introduction of various agents into the liquid phase is known as 'salting out'.

The formation of a supersaturated solution is a prerequisite for crystallization to occur. Here supersaturation achieved by cooling and solvent evaporation will be explained shortly on a typical solubility diagram (Fig. 4.2). The diagram is divided into three regions:

- The stable (unsaturated) region where crystallization is impossible.
- The metastable (supersaturated) region, between the solubility line and nucleation line, where growth may occur but spontaneous nucleation does not.
- The labile supersaturated region of spontaneous and rapid nucleation.

Supersaturation achieved by cooling a saturated solution is represented in Fig. 4.2 by the line AC. Cooling a solution with concentration, C, from the initial point A will lead to the point B on the solubility curve. At this point the solution reaches the saturation. On further cooling

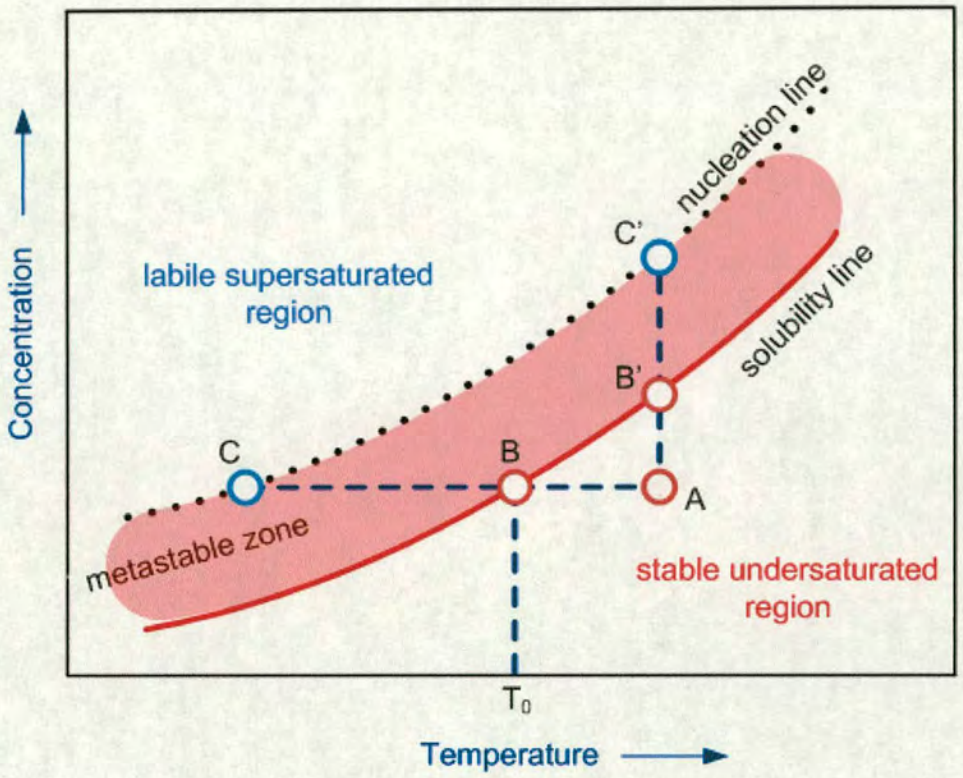

Figure 4.2: *The solubility-supersolubility diagram*

the system becomes supersaturated but spontaneous nucleation to form crystals does not occur immediately in this region until a point C on the metastable boundary is reached.

Concentrating a saturated solution by evaporation of solvent is shown by the line AC'. When the initial concentration is increased by solvent removal the saturation concentration is obtained at point B'. On this line if solvent evaporation continues the supersaturation is attained at point C' and hence spontaneous nucleation occurs. The degree of supersaturation in a solution can be defined in two ways [70]: using the concept of absolute supersaturation (Eq. 4.2) or as degree of supersaturation ((Eq. 4.3):

$$\Delta C = C - C_0 \tag{4.2}$$

$$\alpha = \frac{\Delta C}{C_0} \tag{4.3}$$

where C is the actual concentration and C_0 is its solubility limit at a given temperature. When C is constant, the departure of a solution from its equilibrium state can be expressed in terms

of absolute supercooling, relative supercooling or coefficient of supercooling:

$$\Delta T = T - T_0 \tag{4.4}$$

$$\beta = \frac{\Delta T}{T_0} \tag{4.5}$$

$$\gamma = \frac{T_0}{T} \tag{4.6}$$

where T_0 is the dissolution temperature and T is the actual temperature. However the higher is the relative supersaturation, the sooner crystallization will start [126].

In a supersaturated solution, part of the solute tends to reorganize itself into a solid form [53]. The minimum amount of new phase capable of independent existence is known as nucleus or crystallization center [70]. Minute structures are formed, first from the collision of two molecules, then from that of a third with the pair, and so on [94]. Initially short chains (monolayer) are formed and later the lattice structure builds up. However, the structures formed in this manner become stable nuclei only after attaining a certain size, known as critical size and determined by their solubility [100]. This process is known as primary nucleation.

Nucleation of new crystals induced because of prior presence of crystals of the material being crystallized is termed 'secondary nucleation' [33]. The new crystals became new centers for growth, or secondary nuclei. Crystals grown in the form of needles or dendrites are often fragile and small parts of the crystal may break, forming secondary nuclei. There is also evidence that the shear forces, imposed on a crystal face by the solution flowing past, are sufficiently to produce secondary nuclei [33].

As soon as an ordered structure is formed by nucleation, the growth units (atoms, ions or molecules) can diffuse from the surrounding supersaturated solution to the surface of the nuclei and incorporate into the lattice resulting in crystals of visible size [94]. Three main processes govern the crystal growth [70] as shown in Fig. 4.3:

(I) the diffusion of the growth units to the surface of a growing crystal.

(II) the adsorption of the growth units by the surface.

(III) the migration along the surface and incorporation in the lattice.

The rate of growth of a crystal depends on several factors such as: temperature, degree of supersaturation, viscosity of the solution, pH, rate of stirring, etc.

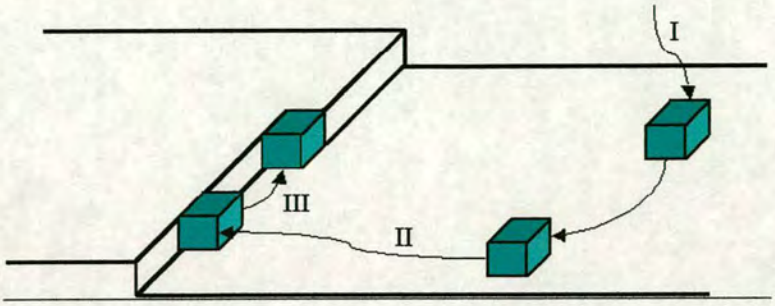

Figure 4.3: *Incorporation of crystal forming elements on the surface of a growing crystal.*

The complex dependence of the rate of growth on various factors has resulted in the development of a large number of theories which will be shortly detailed below. However, special growth theories for growth from solution are not yet developed. The existing theories modify general models, where the solvent is seen as an impurity [11–14, 121]. The main theories are shortly described below. A more detailed review of a set of growth theories is given by Sgualdino [121].

Diffusion theories

These theories concentrate on modelling crystal growth process from a technological point of view [121]. The basic *tent* of this theory is that deposition of a solid on the face of a growing crystal is a diffusional process [70, 94].

When a crystal is placed in a supersaturated solution, a layer with a variable concentration of the crystallizing substance is formed near the surface of the crystal [70]. The concentration across this layer is diffusionally controlled and varies from a concentration, C, equal to the concentration of the bulk solution, to the saturation concentration C_i, at the surface of the crystal (Fig. 4.4). This layer is called diffusion layer. On stationary crystals in stagnant aqueous solutions this thickness takes values between 20 and 150μ. In vigorously stirred solutions the layer thickness is zero and the concept of film diffusion is not sufficient to explain the mechanism of growth.

The rate of growth or dissolution of a crystal depends on the amount of matter diffusing through the layer. The mass diffusing through the layer taken by unit area is proportional to the absolute supersaturation, according to the semi-empirical equation:

$$\frac{dm}{dt} = k_m A(C - C_0) \tag{4.7}$$

where: m is the solid mass deposited in time, A the surface area of the crystal, C the solute concentration in solution (supersaturation), C_0 equilibrium saturation concentration and k_m is the coefficient of mass transfer.

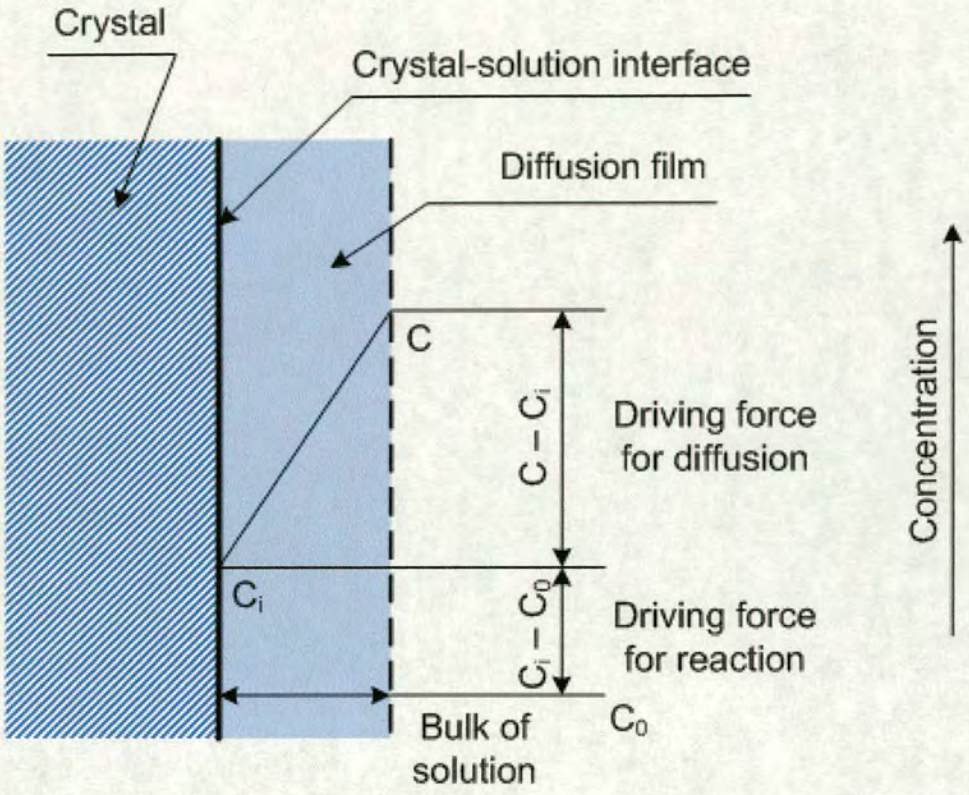

Figure 4.4: *Film model for crystal growth.*

Eq. 4.7 implicitly contains the two steps common to all heterogenous processes [75, 121, 124, 140], which are:

- mass transfer of the growth units from the solution to the crystal face, which is diffusionally controlled.
- arrangement of the growth units in the sites of the crystal surface, which is described by the rate equation for the first-order reactions.

Mass transfer of the solute is described by an equation such as:

$$\frac{dm}{dt} = k_d A(C - C_i) \tag{4.8}$$

where k_d is the coefficient of mass transfer by diffusion.

The integration rate can be written:

$$\frac{dm}{dt} = k_b A(C_i - C_0) \tag{4.9}$$

where: k_b is the kinetic constant of the integration rate (at the boundary separating the two phases), C_i the concentration at the surface of the crystal face and C_0 equilibrium saturation concentration.

Adsorption Layer Theories

These theories are based on the assumption of the existence of an absorbed growth unit on a crystal face, F, and that the growth process is a sequence of repeatable steps [63, 70, 94]. The growth units in the vicinity of a crystal face tend to attach themselves onto the surface in the position where the attractive forces are greatest, for example they will migrate towards positions where maximum number of like elements are located.

Different growth mechanism were proposed according to whether the F surface is perfect or not [121]:

- growth by two dimensional nucleation (2D), in the case of a perfect face. An activation energy is required to create a critical 2D nucleus and therefore growth takes place only above a critical supersaturation. Two models account the two-dimensional growth mechanism: the mononuclear and the polynuclear model, the last is known as 'birth and spread' model. The polynuclear model assumes the nucleation ('birth') of the critical nuclei and their subsequent growth ('spread') laterally across the surface at a finite rate, while the mononuclear model assumes a spread on the surface at infinite rate.

- growth determined only by the flow of the growth units either diffusing on the surface or through the bulk of the mother phase. This is the case of a non-perfect face, when one ore more screw dislocation cross the flat surface and hence self-perpetuating ledges of steps are present on the face. This model describes growth at low supersaturations and is known as Burton-Cabrera-Frank (BCF) model. The screw dislocations in the crystal are a continuous source of new steps and therefore the screw mechanism provides a way for steps to grow uninterrupted.

When a crystal is exposed to a saturated environment, the flux of the growth units, to the surface exceeds the equilibrium flux so that the number of units joining the surface is greater than that

leaving [33], hence resulting in a growth of the surface. The ability of a surface to capture and integrate the arriving growth units depends on the strength and the number of interactions between the surface and the growth unit.

In the three dimensional representation of a crystal, a growth unit forms a maximum of three bonds with the surface, as shown in Fig. 4.5. Following the classification of Hartman [63], a face with three bonds is a kinked or a K face, a stepped or a S face and a flat or face F are faces where two bonds and respectively one are possible. In the ideal case, F faces are atomically flat, S faces are composed of ledges, and K ledges consist of kinks only.

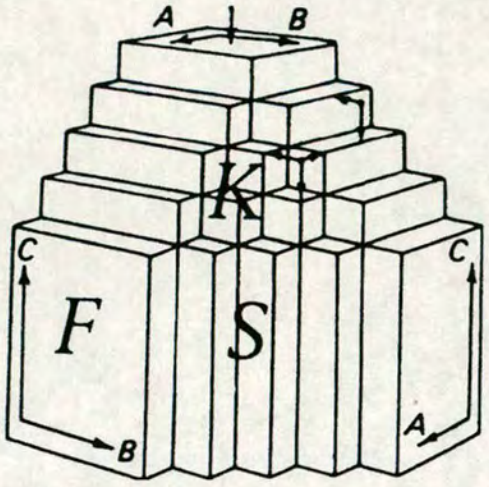

Figure 4.5: *A three-dimensional crystal showing K, S, and F faces [63].*

The requisite for the growth of a crystal is the presence of a sufficient number of kinks on its faces. K faces are typically composed of kinks, but on S and F faces kinks can be also supplied by statistical fluctuations. Because S faces are composed of ledges, the kink density on them is expected to be much higher than on F faces. A natural consequence of the surface structure is that the F faces are the slowest growing faces, S faces grow at a faster rate than the F faces, and K faces are the fastest growing faces, so that they are usually absent in the growth morphology [63].

4.3 Experimental details

Two types of experiments were conducted to grow ettringite crystals from solution. The development of the supersaturation, the driving force for the nucleation and subsequently for crystal growth, was induced by cooling and solvent evaporation.

'Cooling crystallization'

A slurry of calcium hydroxide (3.50g) and aluminium sulphate hydrate (5.0017g[1]) was mixed in purified water heated at $\simeq$ 70°C (100 mL/16.4Mωcm) for 5s. This temperature was chosen to reproduce similar conditions often encountered by the cementitious systems. The mixture was weighed out in stoichiometric proportions to form ettringite: CH : $A_2\overline{S}_3H_{16.3}$ = 6:1. The amount of water in the aluminium sulphate reagent was determined by conventional gravimetric method. After approximately 5min reaction time, the resulting mixture was vacuum filtered through a 0.45μm nitrate membrane filter. The mother liquor was transffered to capped HDPE bottles under nitrogen flow as an additional precaution against CO_2 contamination. The samples were then stored in the refrigerator at 9°C for a month. A change in temperature throughout the sample (rapid quench) is expected to produced supersaturation and hence the precipitation of crystalline ettringite. The samples were investigated by low-temperature scanning electron microscope every 7 days for a month, to observe morphological changes over time.

A Hitachi S-4700 II cold field-emission scanning electron microscope (FEG SEM), equipped with a Gatan Alto cryo-preparation system for high-resolution low-temperature SEM, an EDAX (Energy Dispersive) Phoenix X-ray microanalysis system for elemental analysis was used for all the experiments outlined here except where otherwise stated. Low vacuum mode is an insufficient answer in observing the ettringite structures under conditions that are closely related to its natural state in the crystallizing solution, as the sample needs to be dried before loading. Even with the versatile environmental scanning electron microscope (ESEM) it is difficult to prevent dehydration, which will occur at any vacuum levels and is difficult to control even with Peltier stages and water vapour in the SEM chamber.

A suitable solution was found to be a system equipped for high resolution low-temperature SEM, where the samples could be observed in natural state without inducing artifacts such as: chemical fixation, use of solvents, sample contamination, dehydration, etc. The cryo-SEM method is more familiar to biologists, for observing biologic materials, very sensitive to the vacuum conditions and/or the high electron beam energy in the SEM. Fundamentally, the principle of this technique is simple, the sample is frozen and maintained frozen. In this way, no dehydration occurs and delicate structures are maintained without shrinkage. Fast freezing means also that the chemical balance is well maintained for microanalysis.

[1]The commercial material had a water content equivalent to $Al_2(SO_4)_3 \cdot 16.3H_2O$.

The samples mounted on specimen stubs were frozen in the freezing chamber which is built into the preparation unit of the microscope. This is typically obtained by boiling nitrogen at -196°C in an insulated container and subjecting to vacuum, that of a rotary pump. The sample holder is then withdrawn, under vacuum, into a vacuum transfer device for transfer to the cryo-preparation chamber. After transfer to the (separately pumped) cryo-prep chamber the sample is maintained at a low temperature and low contamination conditions. Finally a thin conductive coating (sputter coating, 60%Au, 40%Pd) of 1.2nm thickness was applied to allow high resolution imaging and microanalysis in the SEM. Nonconductive samples are typically subject to a build up of electrons on the examined surface. This build up of electrons or charging eventually causes scattering of the incoming electron beam, which interfere with imaging and analysis.

Transfer to the SEM chamber is via an interlocked airlock and onto a cold stage module fitted to the SEM stage. Contamination of the specimen with condensing water vapour or other contaminants, while inhibiting sublimation of water from the specimen was avoided by maintaining good vacuum of about 10^{-9}Torr. Energy-dispersive X-ray analysis were used when necessary to distinguish the identity of structures in the precipitates.

The pH and conductivity of the supernatant were measured using an Accumet Research AR15 pH/mV/°C Meter fitted with a combined pH electrode and conductivity cell. The pH meter was calibrated using two buffers, typically 7.0 and 9.2 (phosphate and borate solutions). Liquid-junction potential effects were minimized by appropriate conditioning and storage of the electrode and by allowing suspended sediment to settle prior to sampling. The conductivity cell was calibrated using a 0.01M KCl solution with a conductivity of 1.4mS/cm.

To determine the amount of species released during mixing, aliquots of $\sim$ 7mL of supernatant were taken at roughly 1, 30, 60, 90, 120, 150 and 180min intervals. Five mL dil. HCl (800mL water + 6mL concentrated HCl) were added to the extracted liquid to prevent carbonation, and the sample further diluted by ten with water before analysis by inductively coupled plasma atomic emission spectroscopy (ICP-AES, Thermo Jarrell Ash IRIS).

'Crystallization by evaporation'

A slurry was prepared using the same stoichiometric proportions as described above for the crystallization by cooling. The working temperature was ambient temperature, 25°C±2. After filtration the supernatant was left to evaporate in plastic petri dishes in a glove box under dry

nitrogen flow to prevent carbonation, approximately one week was necessary to remove all the water. The evaporation rate was slowed down using Whitman filter paper (43μm) as 'breathing lid', to keep a fairly constant supersaturation of the sample and hence obtaining uniform crystals. Due to difficulties encountered in reaching the equilibrium saturation with respect to ettringite and hence reproducibility of those experiments, a set of precipitation experiments were conducted using synthetic ettringite as source of precipitate. 1g of pure synthetic ettringite and 100mL deionized water, roughly ten times the saturation of ettringite at equilibrium, were placed in HDPE bottle with a magnetic stirrer. The sample was left to equilibrate for 20 days at ambient temperature to reach the equilibrium with respect to ettringite. Every second day the experiment was sampled for analysis by ICP-AES to track the content in Ca, Al and SO_4 versus equilibrium concentration. Because of the small amount of samples resulting from this experiment, an additional experiment using larger volumes of samples was conducted in duplicate. After 20 days the steady state was achieved. The sample was then vacuum filtered and the supernatant placed for evaporation, at ambient temperature in open air. After complete evaporation the precipitate was observed by SEM. Complementary techniques such powder X-ray diffraction (XRD) and Raman spectroscopy (RS) were used where required. Synthetic ettringite was prepared using the same stoichiometric proportions described in the 'cooling crystallization' section. The slurry was stirred at ambient temperature at 600rpm for 48 hours. Subsequently the slurry was left to equilibrate for another 7 days and then vacuum filtered. The solid was then washed 8 times to leach excess gypsum and gently dried on $CaCl_2$ solution to keep constant a relative humidity of 30%. The synthesized solid material was then analyzed by X-ray diffraction, using a Bruker AXS D8 diffractometer (CuK_α radiation, 40 kV, 40 mA) and identified as pure crystalline ettringite.

4.4 Results and discussions

4.4.1 Crystallization by solution cooling

In this method supersaturation is produced by a change in temperature throughout the sample. The solubility of synthetic ettringite is known to increase with temperature. The calculated ion activity products (IAP), expressed as log IAPs are reported to increase with temperature ranging from 5 to 75°C [108, 114]. The result of a fairly elevated temperature coefficient of solubility of ettringite, crystallization by cooling is considered a suitable method for crystal growth.

The ettringite crystallization process takes place in such a way that the point on temperature dependence of the composition moves into the metastable solution region along the saturation curve in the direction of lower solubility as explained on a typical solubility diagram and shown in Fig. 4.2. Samples obtained by this method exhibit good crystallization (Fig. 4.6).

The ettringite crystals formed in these conditions are long, thin rods, hexagonal in cross-section (Fig. 4.7a) and seem to develop by aggregation of several crystallites (stable nuclei, particles longer than the critical size). The rods present a radial arrangement with an average in length $\sim 600\mu$m and width $\sim 5\mu$m, indicating an aspect ratio of about 1:100 (Fig. 4.9 and Fig. 4.10).

The larger crystallites are apparently fractured (Fig. 4.7a and Fig. 4.8) and have ragged edges and ends. Disordered material (unstructured) has been observed as a part of the core figure (Fig. 4.10a). According to crystal growth theory, we might assume the presence of unstructured material to be a consequence of the recrystallization that is the final stage of the crystallization processes. However it is well known that the contact between the precipitated phase and the supernatant leads to a change in the physical and/or chemical properties of the solid phase. This process involves recrystallization of non-equilibrium shapes of primary particles to form more compact shapes.

The activity of the dissolved substance in solution (and consequently its concentration) in equilibrium with a crystal is a function of their shape, specifically, the activity in equilibrium solution increases with decreasing size [126]. In our case, the solution is undersaturated with respect to crystals smaller then equilibrium crystal size, which will dissolve and supersaturated with respect to crystals larger then equilibrium crystal size which will grow. All these processes are diffusionally controlled, a statement also sustained by Mori *et al.* [93] and Brown *et al.* [18].

However, if initial supersaturation is increased, the critical supersaturation at which homogeneous nucleation becomes important will be attained and this results in a sudden increase in the number of particles formed. As a result, their final size begins to decrease and the crystals become more anhedral as they have insufficient time to develop well-defined crystal faces. A precipitate formed under such conditions often appears unstructured (no crystal structure).

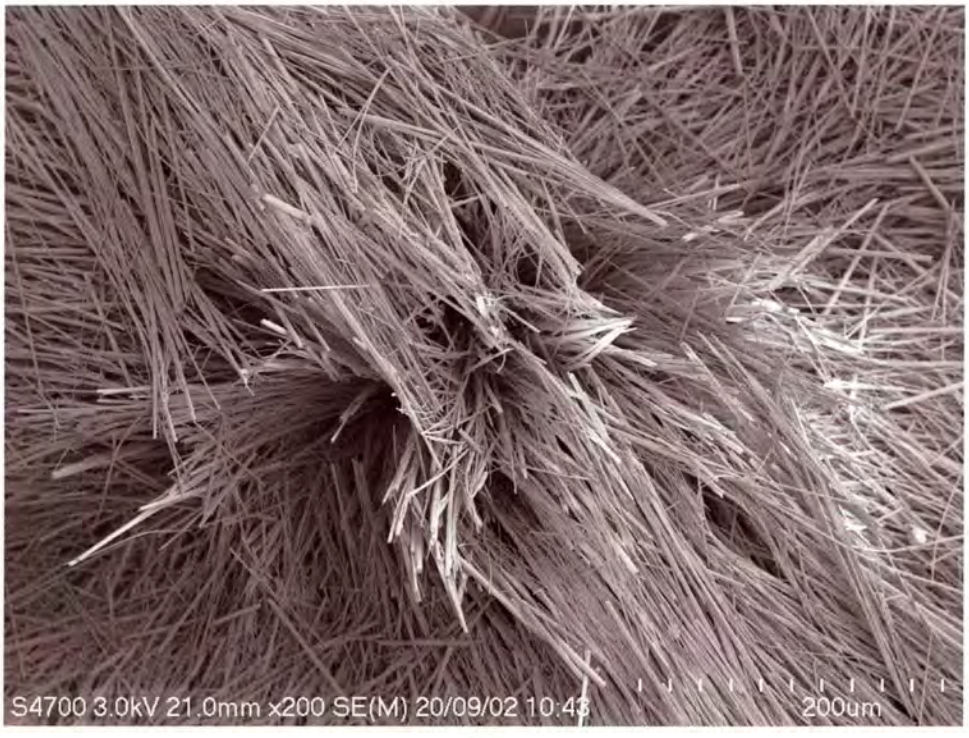

(a)

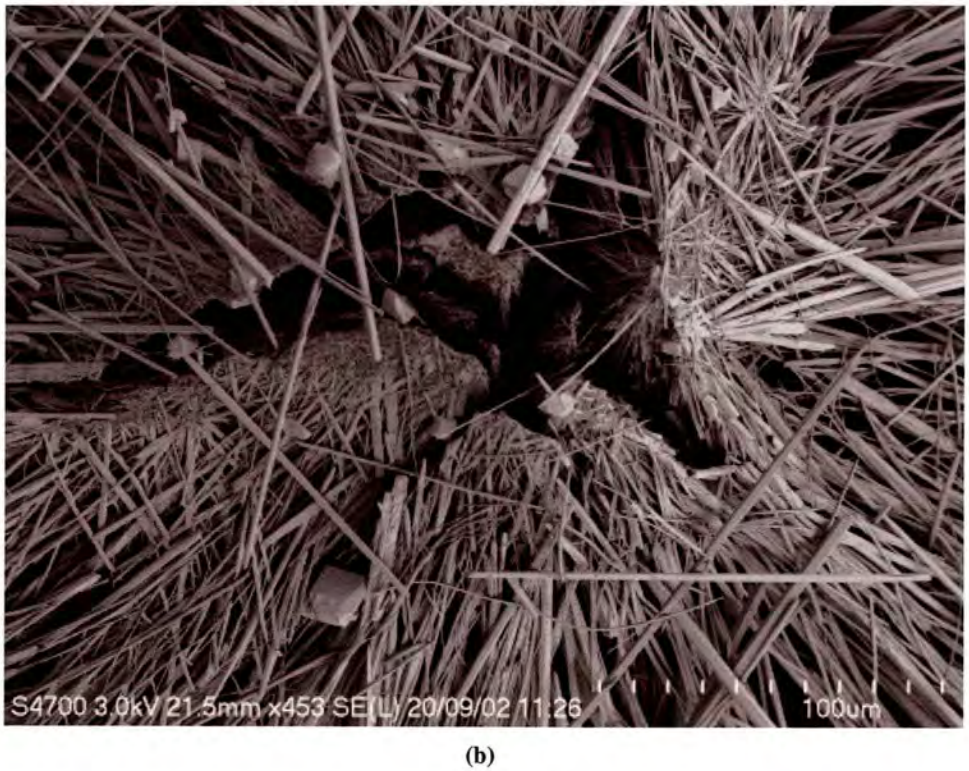

(b)

Figure 4.6: *(a) Synthetic ettringite grown in solution, showing needle-like morphology. (b) Fractured core co-existing with gypsum impurity.*

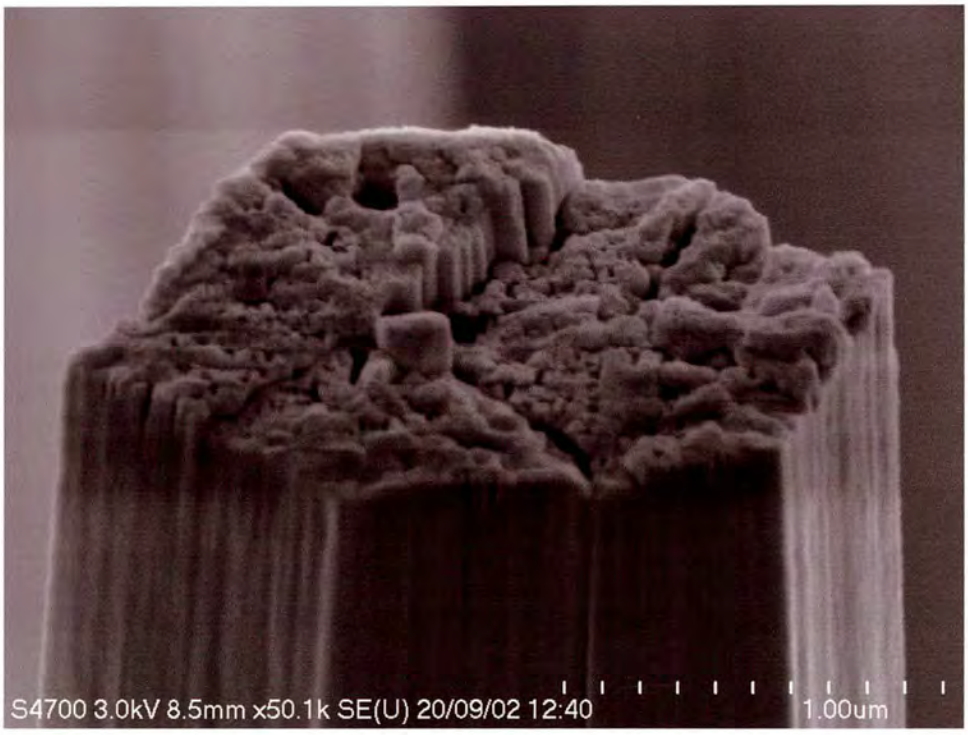

(a)

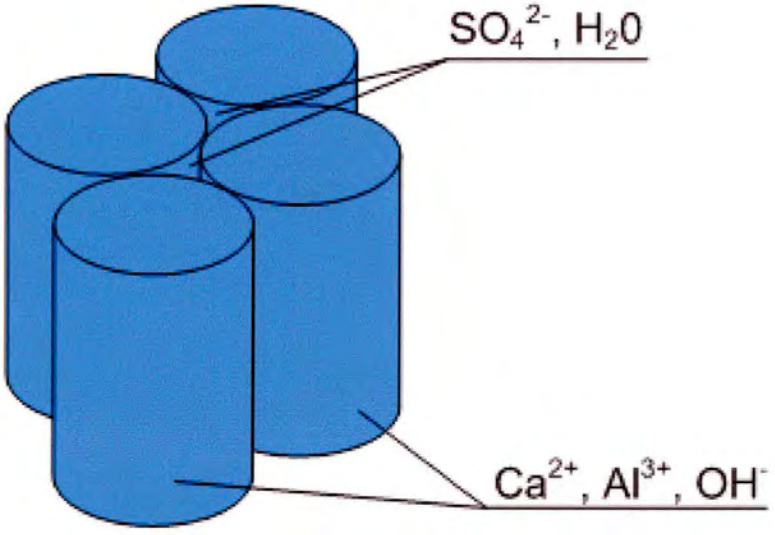

(b)

Figure 4.7: *(a) SEM of one single ettringite entity showing hexagonal cross-section. (b) Crystal structure of ettringite, showing columns whose empirical composition is* $[Ca_3Al(OH)_6 \cdot 12H_2O]_2^{3+}]$ *and channel sites occupied by sulphate ions and water.*

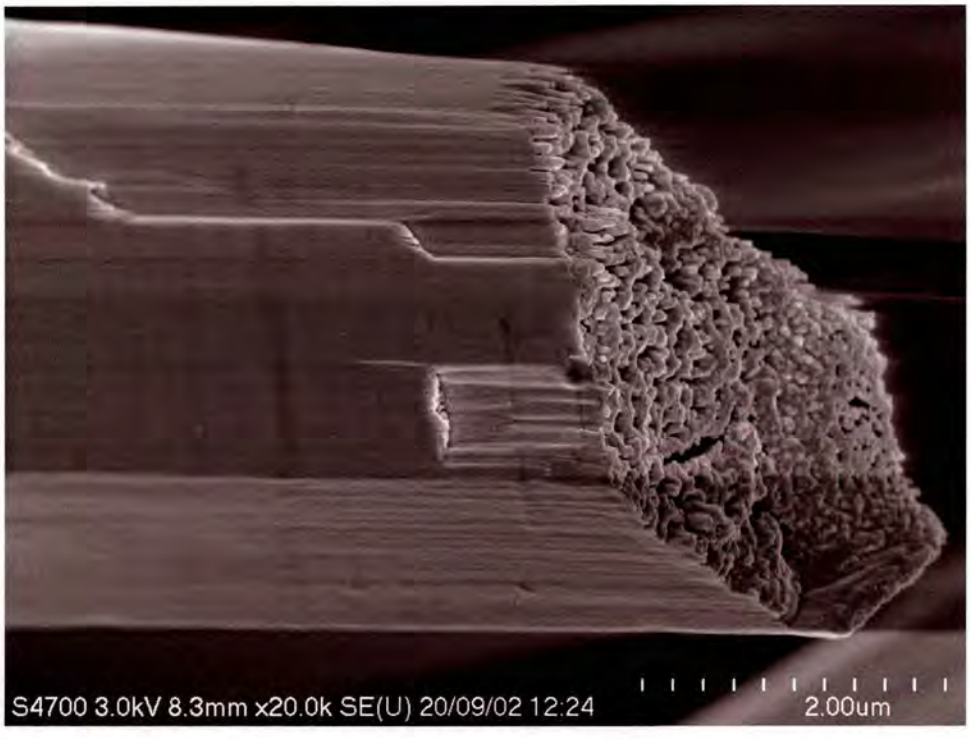

Figure 4.8: *Indication of an internal structure of fibrils in the ettringite rods.*

At high supersaturations the rate of crystal growth can reach such high values that the heat of crystallization released cannot be transferred sufficiently quickly from the crystal into neighbouring solution or conducted into the bulk of the crystal. In this way, the crystal faces become surrounded by depleted solution, as diffusion cannot supply solute to the crystal at a fast enough rate. Since the crystal edges reach into the regions of the last depleted solution they tend to continue growing. This cause elongation of the crystal and, at the same time, extension of its surface to aid transfer of heat of crystallization.

Very long ettringite fibres (Fig. 4.9) with a typical hexagonal habit are observed. Again we note that the end face is rough. There is also some indication of an internal structure of fibrils, ('brush type'), in the ettringite rods (Fig.4.8).

The fastest growing face was identified to be the one perpendicular to the c-crystallographic axis which has the lowest lattice density, in agreement with Coveney [67]. The relative growth rates of faces were determined on the basis of knowing the crystal structure.

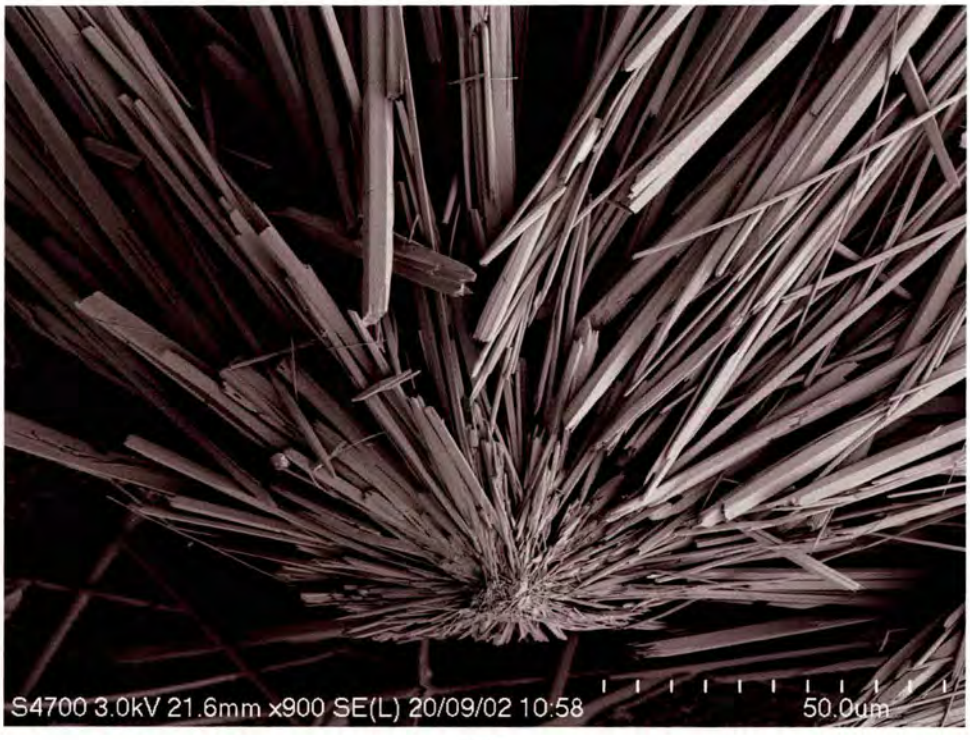

(a)

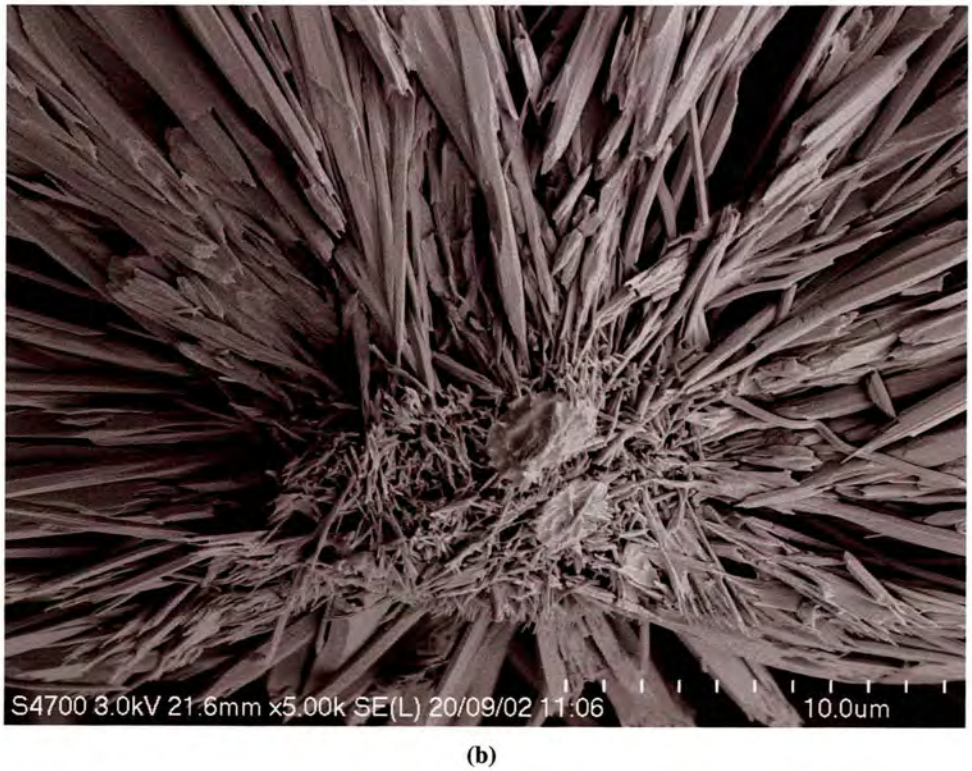

(b)

Figure 4.9: *(a) Ettringite rods exhibiting a radial arrangement. (b) SEM micrograph of a ettringite core grown by solution cooling.*

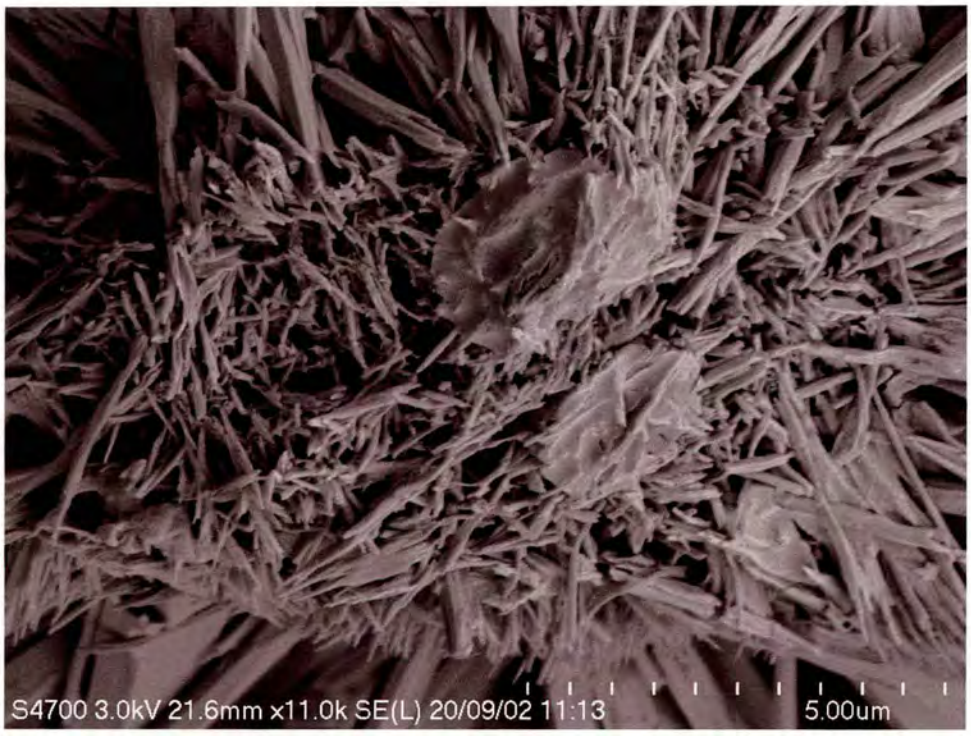

(a)

(b)

Figure 4.10: *(a) SEM micrograph showing the existence of unstructured material as part of the core. (b) Large crystallite fractured with ragged ends.*

According to Bravais-Friedel-Donnay-Harker approach [33] the binding energy between crystal planes is inversely proportional to the interplanar spacing, meaning that the closer the molecules the larger at their interaction energies. The growth rate of a face (hkl) is proportional to the inverse of the distance between the (hkl) planes in the crystal structure, $1/d_{(hkl)}$.

The ettringite crystal structure consists of columns and channels running parallel to the *c*-axis of the hexagonal prisms as shown in Fig. 4.7b. The composition of the columns is $[Ca_6Al(OH)_6 \cdot 24H_2O]^{6+}$, per half unit cell [91].

The material in the channels is $[(SO_4)_3. \sim 2H_2O]^{6-}$. Each of the columns is composed of $Al(OH)_6$ octahedra alternation with triangular groups of edge-sharing CaO_8 polyhedra with which they share the $(OH)^-$.

Each calcium is coordinated to four water molecules, the hydrogen atoms of which form a column of nearly cylindrical surface. For each channel, there are two SO_4 tetrahedra pointing up, followed by one pointing down and then followed by a site containing three water molecules. This site is partially occupied so that there are only two water molecules present at any time.

The internal structure of fibrils observed in Fig. 4.8 can be simply explained based on the structural information of ettringite. The fibrils can be viewed as columns of $[Ca_6Al(OH)_6 \cdot 24H_2O]^{6+}$ composition running parallel to the *c*-axis of the crystal. The anions and remaining water molecules form a randomly disordered arrangement in the channels between the columns. Hydrogen bonds link the water molecules of the columns with the anions and water molecules in the channels. The water molecules are loosely bound into the structure and so water can easily be removed at higher temperature or lower humidity.

This is evident in Fig. 4.8, where a free space can be seen between the fibrils. This is probably, because same of the water was released during sample analysis. Ettringite can thus exist with different water contents but the same crystal structure. The fibre structure appears to be fragile, such that the shear force (caused only by samples manipulation) imposed on a crystal face by the solution flowing past it might be sufficient to produce breaking and initiate a secondary nucleation with a relevant influence on ettringite rheology.

The fragility is given presumably by the weak hydrogen bonds bridging calcium and aluminium atoms. Moreover, calcium coordination to the four water molecules brings alone a column of nearly cylindrical surface of hydrogens. Four out of every five atoms in ettringite structure is either a part of a water molecule or an hydroxide. The ettringite structure is almost all water. This fact is reflected in a very weak lateral strength of the ettringite crystal.

The ettringite crystals grown here through solution mechanism, were much more elongated with a radial fibrous appearance suggesting a rapid growth. This is generally caused by a high absolute supersaturation.

Measurements of the species released in the supernatant in equilibrium with the slurry along the cooling curve suggest a high level of supersaturation (Table B.1). The degree of supersaturation with respect to aluminium, calcium and sulphate approximated using Eq. 4.3 was about four times the saturation at equilibrium.

This can be also seen in Fig. 4.11, where the actual concentration of the supernatant are compared with the equilibrium concentration. The supernatants withdrawn at the lowest temperature of 50°C only were used to precipitate ettringite crystals. When the supernatant was extracted, its concentration point on the solubility-supersolubility diagram was situated already on the nucleation line, hence resulting in a instantaneous precipitation.

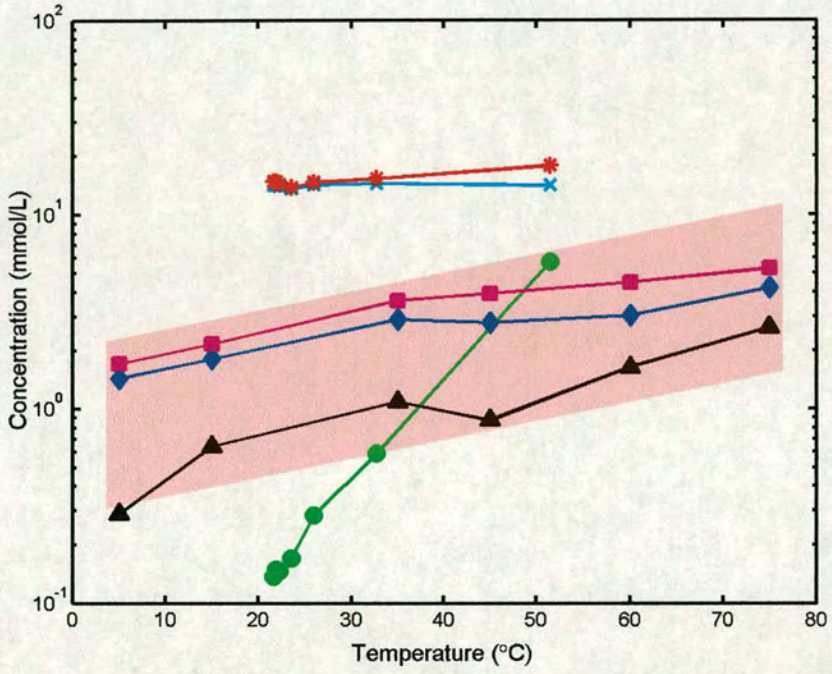

Figure 4.11: *Temperature dependence of the supernatant concentration prepared by mixing reactant solutions. Concentrations of aluminium, calcium and sulphate are shown as follows:* Al^{3+} (•), Ca^{2+} (∗), $SO_4{}^{2-}$ (×). *Equilibrium concentrations (at saturation) of aluminium, calcium and sulphate as determined by Perkins [108] in temperature-dependent ettringite dissolution experiments, are also shown:* Al^{3+} (▲), Ca^{2+} (■), $SO_4{}^{2-}$ (♦). *The area highlighted in pink represent the solubility line (in red) in the solubility-supersolubility diagram Fig. 4.2.*

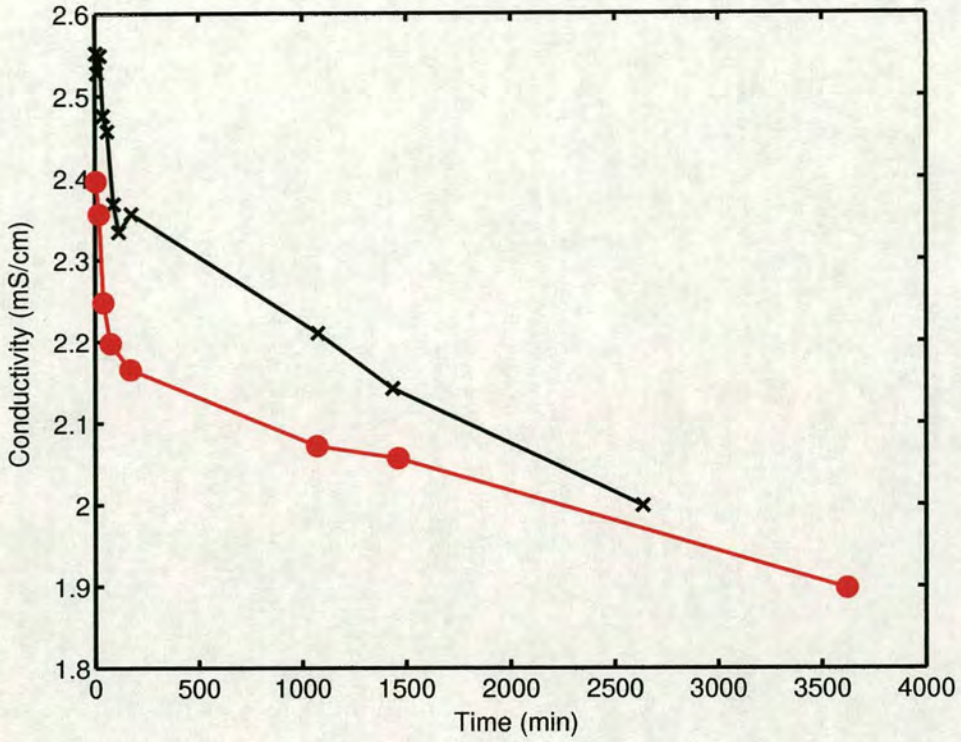

Figure 4.12: *Representation of the time variation of conductivity of the supernatant. The conductivity is shown for two samples where the supernatant was withdrawn from the reactants mixture at 1* (×) *and 20min* (•). *The change in solution conductivity indicates an induction time equal to zero at the time when first measurement was taken. The nucleation process appears to cease after ~3 days.*

The conductivity measurements of the supernatant shown in Fig. 4.12 indicate a zero induction time for the nucleation process, which also translate in an instantaneous precipitation.

The initial supersaturation of the supernatant is driving the nucleation and crystal growth processes of ettringite, and dictates the morphology. Dendrites (rods) formation are typically, seen for initial supersaturations higher than 10 and, associated with a heterogenous nucleation process and a combined mechanism of growth (diffusion and surface reaction) [126]. In this study, ettringite exhibits dendritic morphology at even lower initial supersaturation and its mechanism of growth is diffusionally controlled. Typically when a solution is cooled, the supersaturation is high, and the rate of growth of a crystal depends strongly on the rate of diffusion [94, 109]. In accord with the dendrite-like morphology that ettringite exhibit, Brown and LaCroix [18] predicted a nucleation and growth model controlled by diffusion.

Ettringite crystals usually grow fastest on the (001) face [67]. Hence an increased rate of growth would result in a much more elongated crystal, which is favoured by crystallization on cooling. As the (001) face is only small this face is favoured over other larger faces parallel to the c-axis. Hence the aspect ratio of the crystal is much increased when growing rapidly.

4.4.2 Crystallization by solvent evaporation

Crystals produced by evaporation have an aspect ratio of about 1:10 (Fig. 4.13). The crystals formed are substantially shorter than those prepared by using the cooling method, exhibiting an average in length of $\sim 60\mu$m and width $\sim 5\mu$m. Twinning phenomena occur too.

In contrast to the cooling method, in which the total mass of the system remains constant, in the solvent evaporation method the solution loses components which are weakly bound to other components and therefore the volume of the solution decreases. In almost all cases, the vapour pressure of the solvent above the solution is higher than the vapour pressure of the solute and therefore, the solvent evaporates more rapidly and the solution becomes supersaturated. At ambient temperature the measured Ca^{2+} concentrations (Table B.2) leaves behind the saturation level with respect to ettringite. As the supply of sulphate ions is uninterrupted the liquid phase remains rich in Ca^{2+} ions. In presence of an adequate amount of alumina numerous ettringite nuclei precipitate in solution. However the crystallization by evaporation takes place at a fairly constant saturation. The value of supersaturation is therefore low because the crystallization takes place by the growth of nuclei formed at the beginning of the evaporation process. Such nuclei will continue to appear until the degree of supersaturation reaches a value sufficient for crystallization. Hence, crystals produced by evaporation are much shorter, yet keep the radial habit (Fig. 4.13 and 4.14).

(a)

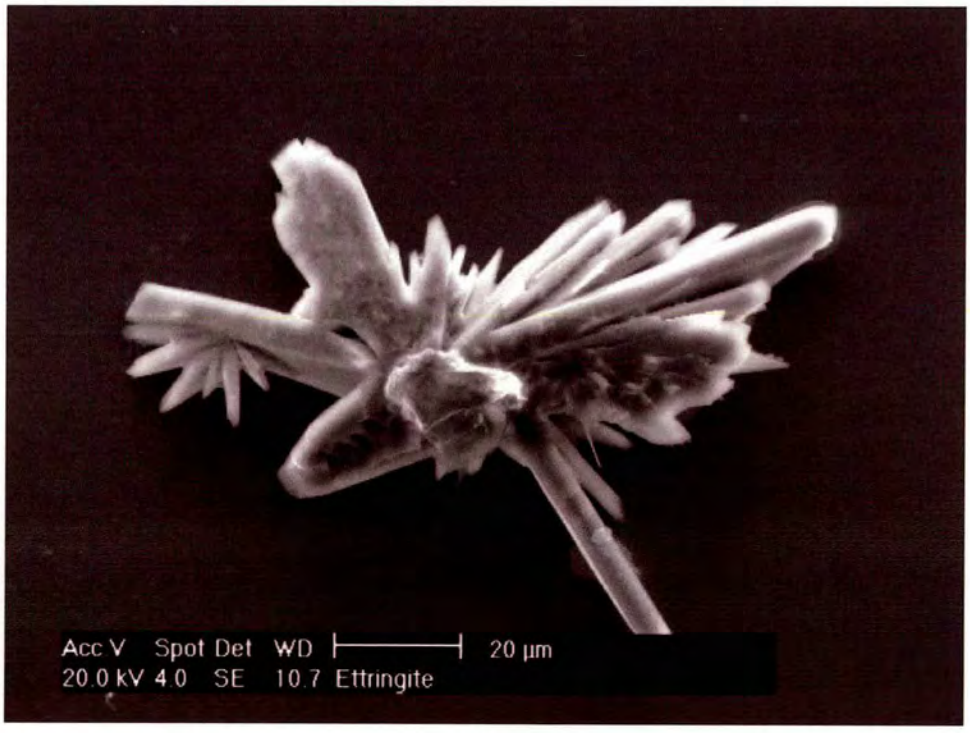

(b)

Figure 4.13: *(a) SEM of ettringite obtained at ambient temperature by evaporation method showing a six-sided morphology. (b) Crystals have an average in length of* $\sim 60 \mu m$.

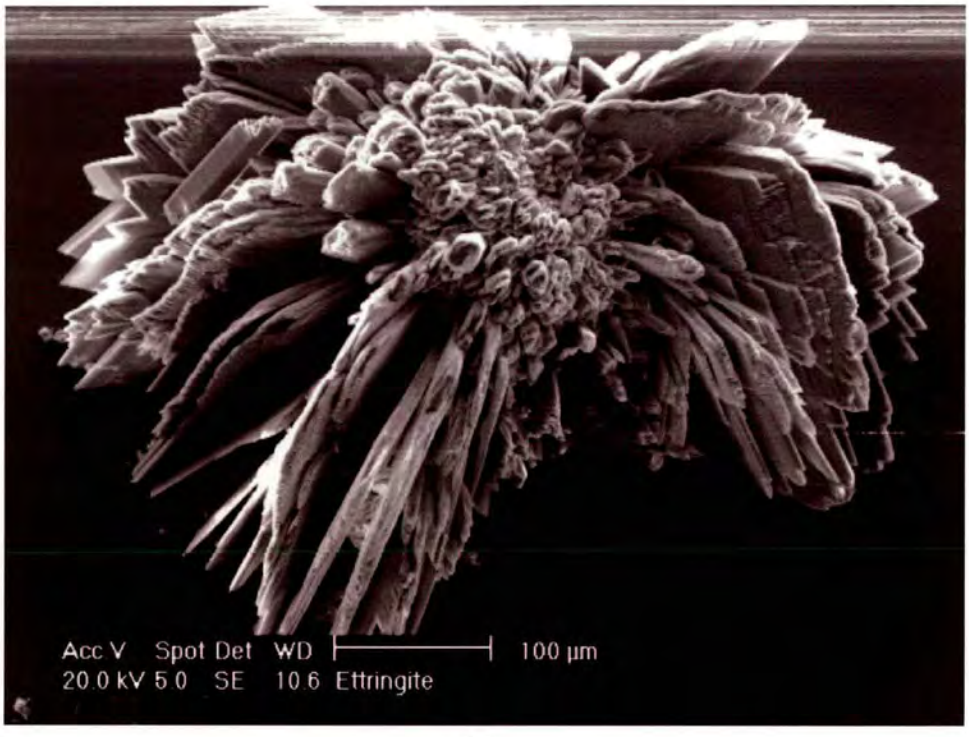

(a)

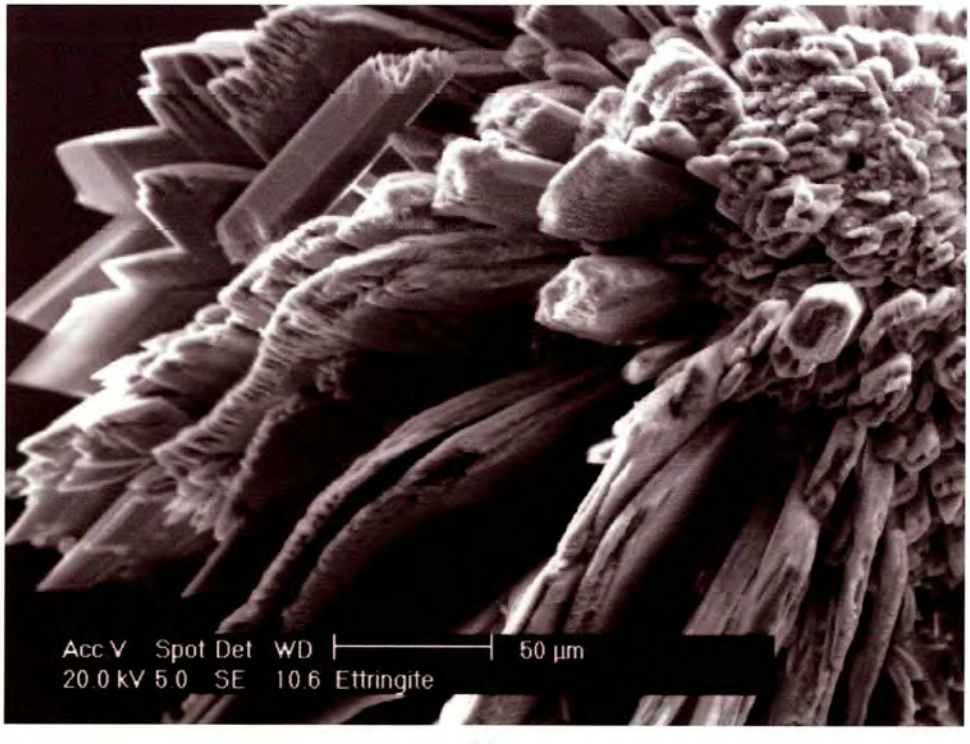

(b)

Figure 4.14: *(a) and (b) Short ettringite crystals exhibiting a radial habit.*

When the supernatant was evaporated in open air, no ettringite crystals grew from solution, although the supernatant contained a stoichiometric proportion of ions to form ettringite. After complete evaporation the precipitate consisted of gypsum and calcium carbonate crystals co-existing with amorphous alumina gel. The precipitate was analyzed by X-ray diffraction and Raman spectroscopy. The X-ray diffraction of the precipitate revealed only gypsum as crystalline material. In order to establish the problems encountered by this crystallization, Raman Spectroscopy was chosen as complementary technique. Raman spectra were recorded on a LabRam micro-spectrometer using a He-Cd blue laser at 488 nm. The Raman spectra of the precipitate shows strong peaks at 1006.7 and 1086.6 cm^{-1} corresponding to the typical vibrations for the SO_4^{2-} and CO_3^{2-} groups (Fig. 4.15 and Fig. 4.16).

However, the Raman spectra were not very conclusive and due to difficulties in identifying the presence of alumina gel, the composition of the precipitate was mapped using an EDAX Phoenix X-ray microanalyser system.

Fig. 4.17 shows maps of the elemental composition of the precipitate sample with respect to Ca, O, S, Al and C. The presence of aluminium is now clearly observed and any uncertainties related to its formation following ettringite decomposition are solved. The stability of ettringite is affected by the CO_2 from air. The amount of CO_2 in the open air is approximately 0.03 to 0.04%, hence 300ppm are sufficient to induce changes in the ettringite crystallization and shift the equilibrium. It appears that when carbonate ions are present in the supernatant, a lower pH is induced and the ettringite nuclei cannot achieve the equilibrium with the supernatant. As the carbonation is also a process controlled by diffusion there is a tendency to form gypsum and calcium carbonate in agreement with the work of Nishikawa [99]. In his study, synthetic ettringite carbonated with excess water was found to decompose to gypsum, calcium carbonate and alumina gel. However its decomposition is favoured by high water/solid ratios [99].

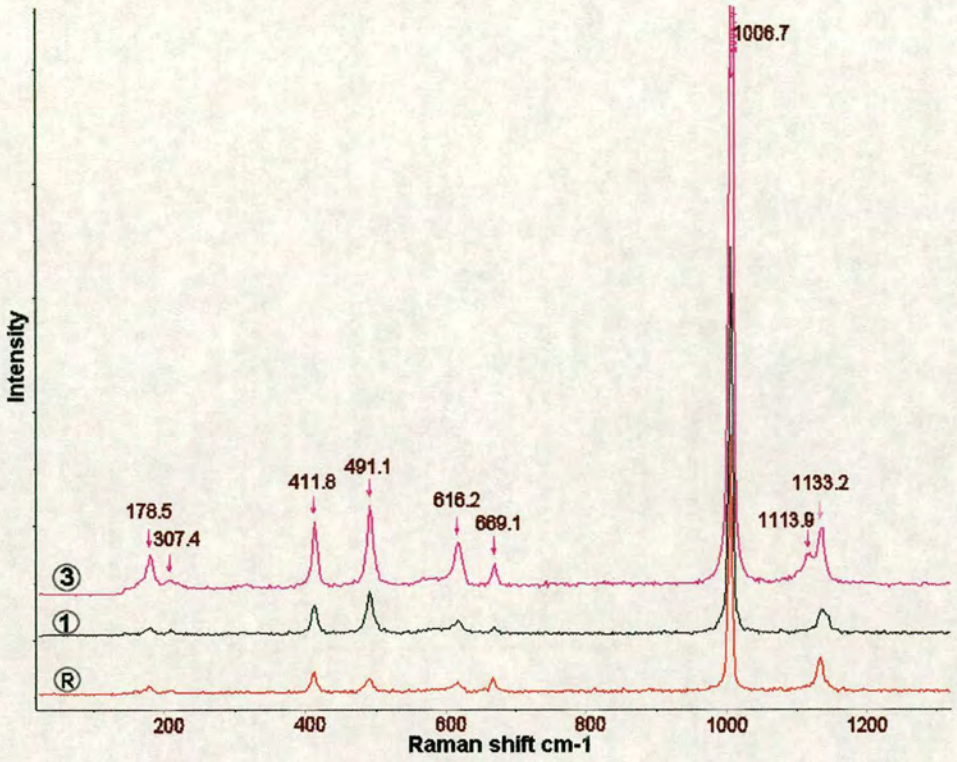

(a)

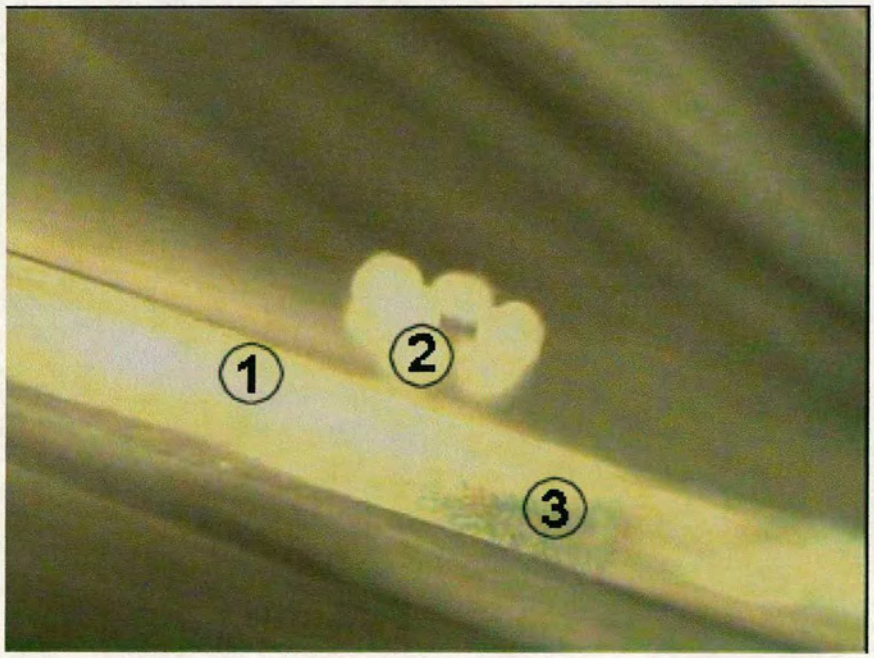

(b)

Figure 4.15: *(a) Raman spectra of two areas on the sample compared with a gypsum reference specimen, (R). Strong peak is observed at 1006.7* cm^{-1} *corresponding to the vibration of the* SO_4^{2-} *species. (b) Image of the precipitate obtained by evaporation of a supernatant having as a source synthetic ettringite, showing areas which were subject of investigation.*

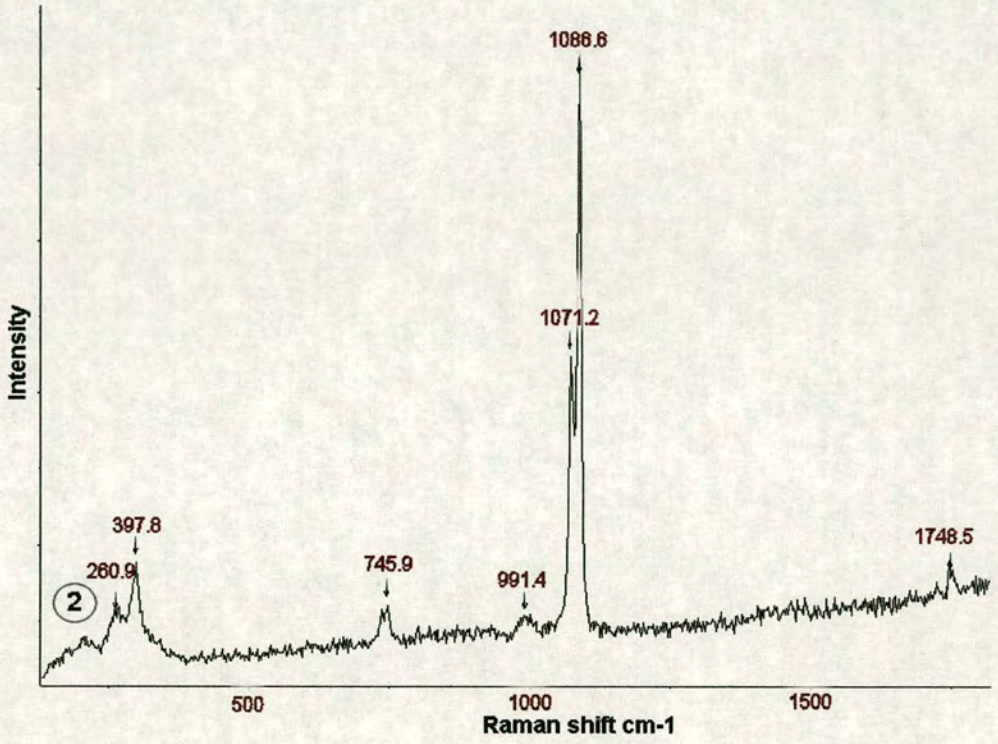

Figure 4.16: *Raman spectra showing strong peak at 1086.6* cm^{-1} *corresponding to the vibration of the* CO_3^{2-} *species. The area investigated is marked in Fig. 4.15b.*

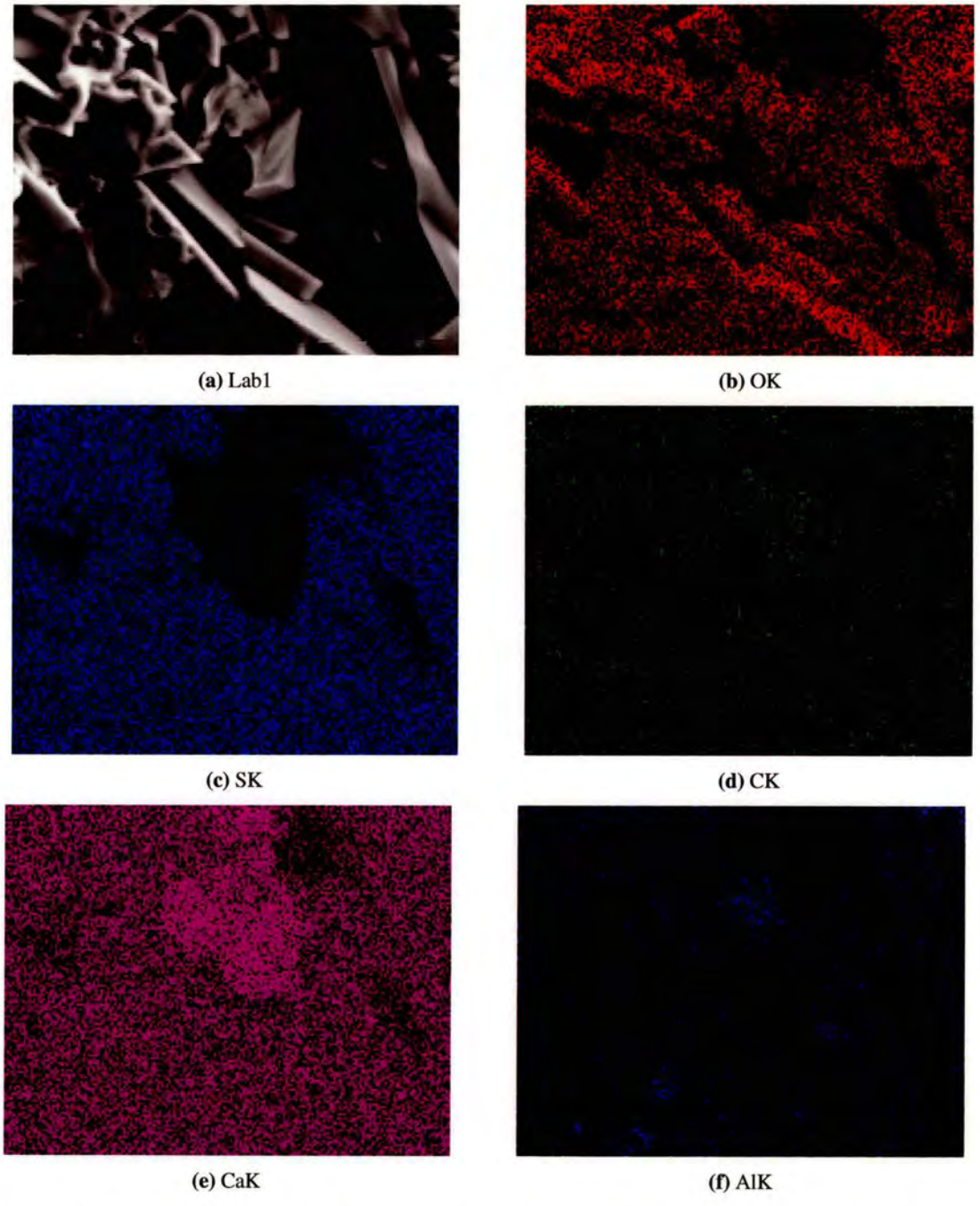

(a) Lab1 **(b)** OK **(c)** SK **(d)** CK **(e)** CaK **(f)** AlK

Figure 4.17: *Compositional map of the precipitate obtained by ettringite supernatant evaporation at ambient temperature. (a) Image of the spot investigated. (b) OK. (c) SK. (d) CK. (e) CaK. (f) AlK.*

4.5 Conclusions

1. General crystallization methods for ettringite synthesis have been developed starting from supersaturated solutions of pure phases. Two methods in which the supersaturation was achieved distinctively have proved to be successful and the results reproducible.

2. The morphology of synthetic ettringite was found to vary with crystallization factors, the temperature for instance. Crystallization by cooling favours the formation of ettringite crystals with high aspect ratio of about 1:100, whereas crystallization by evaporation forms much stubbier particles. However ettringite crystals are always hexagonal in cross-section with a radial disposal from a central core.

3. Ettringite grown by cooling the supernatant has a fibrous appearance with a 'brush type', fibril internal structure suggesting a more rapid growth.

4. Ettringite crystals are identified to grow fastest on the (001) face in agreement with Coveney's work [67].

5. Non-structured material was observed as part of the aggregate-crystal core, possibly due to recrystallization process.

6. Initial supersaturation governs the mechanism of growth of ettringite, hence its morphology.

7. Ettringite decomposes to gypsum, calcium carbonate and alumina gel when exposed to CO_2 in air at room temperature.

Chapter 5
Flow properties of freshly prepared ettringite suspensions in water

The purpose of this chapter is to examine the contributions of the morphology of the hydration products, in early cement hydration, to the rheology evolution. Although, much is known about the rheological properties of cement slurries, a better understanding of the flow properties is needed to be able to predict the flow of cement slurries from the properties of the components. More specifically, this chapter presents an original investigation of an important engineering 'consequence' of the morphology of ettringite. This work was recently published in the Journal of Colloid and Interface Science [134].

5.1 Introduction

The rheology of suspensions is of both practical and theoretical interest for a wide range of applications. Industrial suspensions include cements, drilling muds, paints, printing inks, coal slurries and many products like foodstuffs, medicines, liquid abrasive cleaners etc. In oilwell cementing, slurries are pumped down the wellbore where they harden to serve as a strong, supporting and impermeable seal. To ensure easy pumping and complete filling of the well annulus without separation of water and cement, the rheology of the slurry is of great importance. A great amount of research has been performed over the past years to achieve a complete characterization of the rheology of cement slurries. The complexity of cement slurry rheological behaviour [98] lies in the influence of factors such as: water cement ratio, size and shape of cement grains, chemical composition of the cement, hydration kinetics, presence of additives and mixing history.

During the first hours of cement hydration, tricalcium aluminate (C_3A) hydration is very important for the rheological behaviour. The hydration is very much influenced by the presence of gypsum [90]. Without gypsum the initial hydration reaction is fast, leading immediately to a stiff consistency. The addition of gypsum makes the concrete placeable (Fig. C.1). In the

presence of dissolved Ca^{2+} and $SO_4{}^{2-}$, C_3A forms ettringite (AFt). In cement the AFt phase is derived from pure ettringite with a partial substitution of aluminium by iron, and $SO_4{}^{2-}$ by other anions. This hydrate phase is formed around the C_3A containing grains and protects them from further rapid hydration. Fast initial ettringite growth may also be the cause of false setting [21]. An important event for rheological study is that C_3A is converted only partially to ettringite during the first minutes of cement hydration. Minerals formed during cement hydration have a considerable influence on the rheological properties due to their morphology and the complex chemistry involved.

A wide range of rheological techniques have been used to study the effects of hydration on flow properties of fresh cement paste during the so called induction period, the dormant period occurring during the first few hours after cement and water are mixed. Lei and Struble [79] combined rheological measurements consisting of creep/recovery tests with scanning electron microscopy to evaluate the hydration kinetics and accompanying microstructural changes occurring in cement paste. They attributed the typically plastic Bingham behaviour of the cement pastes with a progressive increase in yield stress as a function of hydration time. This increase was believed to be due to the formation of hydration products like calcium silicate hydrate, the early gel layer, or crystalline AFt, that strengthen the bond between particles. Rods of AFt intimately mixed with the gel were observed [79]. Recently, these observations have been confirmed by Kirby and Lewis [72], who studied rheologically the property evolution and hydration behaviour of pure white Portland cement pastes and concentrated cement-polyelectrolyte suspensions. The advanced hydration enlarges the contact area between particles as more gel forms resulting in increase in yield stress. Some understanding of such phenomena has come from the extensive studies of the properties of colloidal gels as a function of solid volume fraction and strength of interparticle interactions performed by Rueb and Zukoski [115, 116]. The rheological properties of freshly mixed water - cement systems are also very important for the pumping, spreading, moulding and compaction of concrete [5, 130].

Because ettringite is formed rapidly in cement/water systems as one of the earliest hydration products, it is likely that it plays an important role in determining the cement/water rheology at early times. We can view the cement paste as comprising a concentrated suspension of relatively large cement clinker particles in an aqueous dispersion of much smaller ettringite particles. We have therefore carried out a rheological study of pure ettringite suspensions. Beyond the intrinsic interest of such a system, the results provide insight into the behaviour of cement slurries.

The amount of ettringite formed in a cement paste rises rapidly from zero to a maximum controlled by the sulphate content of the cement. We estimate that the maximum ettringite volume fraction in the continuous phase of the cement slurry is about 0.1. We have therefore chosen to investigate the rheology of ettringite/water systems over a range of concentrations up to 0.08.

More specifically the aim of the work has been to investigate experimentally the dependence of the shear viscosity of ettringite rod suspensions on size and shape distributions and particle volume fraction. An extensive review of the rheology of rod systems was given by Wierenga et al. [138]. Non-Newtonian effects appear because of particle shape/orientation and the interactions between the suspended particles. For these colloidal particles surface chemistry is also important. Brownian forces, direct interparticle forces and hydrodynamic interactions via the solvent are all of comparable magnitude. Consequently, the rheology of colloidal suspensions exhibits very diverse behaviour. One of the objectives of this project is to determine whether a relatively complex system like ettringite can be understood within the broad framework that has been developed for colloidal systems. This project describes the preparation structure of ettringite suspensions, their rheological characterisation and a comparison of this with models developed for rod-like colloids.

5.2 Experimental

5.2.1 Preparation of ettringite suspensions

Ettringite was synthesized by mixing a calcium hydroxide slurry and an aluminium sulphate solution as previously described by Hall et al. [59]. The water content of the hydrated aluminium sulphate was checked by measuring the dehydration weight loss and the stoichiometric proportions were adjusted accordingly. The reaction is known to be rapid and complete at room temperature within 30 to 60min [59].

$$6CH + A_2\overline{S}_3H_{16} + 10H \Rightarrow C_6A\overline{S}_3H_{32} \tag{5.1}$$

A stock suspension of ettringite with a solid volume fraction of 0.10 was prepared from 9.36g aluminium sulphate[1] and 6.55g calcium hydroxide (both Sigma Aldrich commercial grade) slurried with 100g of deionized water. The solid volume fraction of the stock was measured

[1]The commercial material had a water content equivalent to $Al_2(SO_4)_3 \cdot 16.3H_2O$.

gravimetrically and found to be in good agreement with the calculated value. The initial pH of the stock suspension was 10.6. By monitoring the supernatant liquid periodically using inductively coupled plasma atomic emission spectral analysis (ICP-AES on a Thermo Jarrell Ash IRIS) it was found that complete conversion to solid ettringite occurs after 2h. The composition of the product was checked using X-ray powder diffraction and found to be pure ettringite with gypsum traces (<2%).

Samples of known concentration were made by dilution of stock suspension using deionized water, based on the following densities for (25°C) $\rho_{\text{ettringite}}$ = 1.78 gcm^{-3}, ρ_{H_2O} = 0.99704 gcm^{-3}. The samples were left to equilibrate for about 10min before performing the measurements. The low solubility of ettringite, $\log K_{sp} = 44.43$ [31], ensured that no major dissolution effects of freshly diluted samples were expected. Ettringite solubility in pure water has been studied from ambient temperature up to 100°C and was found to be essentially constant up to 60°C in a solution with a pH between 10.4 and 11 [50]. The initial ionic strength of the stock slurry was estimated to be 0.031M. Chen and Mehta [20] found that zeta potential of the ettringite particle surface was -11.6mV.

5.2.2 Scanning Electron Microscopy of ettringite suspensions

The particle shape, size and aspect ratio of the ettringite suspensions were measured from scanning electron microscope images. A Philips-FEI XL30 field emission gun scanning electron microscope (FEG-SEM) was used in high vacuum mode. The specimens were taken from three fresh suspensions (having solids volume fractions of 0.03, 0.05 and 0.10) and placed on a microscope slide to cover an area of about 1cm^2, dried and carbon coated. Particle size parameters were estimated by image analysis of micrographs, using Feret's method [66] that gives the distance between two tangents on opposite sides of the particle, parallel to a given direction. The length of the particle was quantified by the projected area diameter, the diameter of a circle having the same dimension as the particle length viewed normally to a plane surface on which the particle is at rest. Only particles clearly lying flat on the slide surface were selected.

5.2.3 Rheological characterization

Rheological tests were carried out in controlled shear rate mode with concentric cylinders geometry using a roughened cup and bob and, in the case of dilute suspensions, double gap (Fig.

5.1a). The temperature of the suspensions in the rheometer was maintained at 25°C in all measurements. For each experiment 10mL of sample was used. After placing the sample in the rheometer, it was left to equilibrate for 60s and then sheared at a constant shear rate of $100s^{-1}$ for 600s 'preshear'. The specimen was then subjected to a controlled ramping of shear rate up and then down. In determining the shear stress/shear rate flow curves care was taken to ensure that at each shear rate the sample reached steady state by waiting 160s. All dilute systems, with $\phi \leq 0.005$, were measured at a single 'optimal' shear rate using the double gap geometry in order to maintain a stable flow and prevent sedimentation. Visual observations of the flow through a transparent cup defined this shear rate to be $20s^{-1}$ (Fig. 5.1b).

5.2.4 Review of particulate suspensions rheology; fundamental concepts: $\dot{\gamma}\ \tau\ \eta$

A brief review of theoretical fundamentals on rheology of particulate suspensions, which will be needed to help understanding and interpreting the experiments, will be summarized here. It is not intended that this should be an extensive review but rather a guide to some of the most important aspects of concern with the principle of a measuring system, typical flow curves of colloidal suspensions, structures in a suspension and rheological models.

Simply, when a fluid (suspensions, emulsions, polymer solutions, melts, etc) is subject to a stress its response takes two forms, first is an elastic response where every molecule suffers a displacement from initial position to a new deformed equilibrium position [42, 46]. Second if the stress is subsequently removed there is a tendency for the fluid to recover its former configuration but incomplete as a consequence of the appearance of viscous flow. So now, one can define the flow as being concerned with the relationships between the stress, τ, shear strain rate, $\dot{\gamma}$, and time. In a shear flow parallel layers of liquid move in response to a shear stress (the component of stress tangential to the area considered) to produce a velocity gradient which is referred as shear rate, $\dot{\gamma}$, equivalent to the rate of increase of shear strain. The ratio of shear stress to shear rate under simple steady shear is quantified as 'resistance' to flow and known as viscosity coefficient of the fluid, η. In simple shear, the viscosity is related to the shear stress and the shear strain rate by the relation:

$$\eta = \frac{\tau}{\dot{\gamma}} = \frac{\text{force}}{\text{area}} \times \text{time} = \frac{\text{N}}{\text{m}^2} \times \text{s} = \text{Pas}. \tag{5.2}$$

(a)

(b)

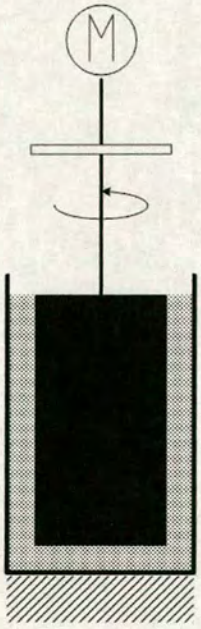

(c)

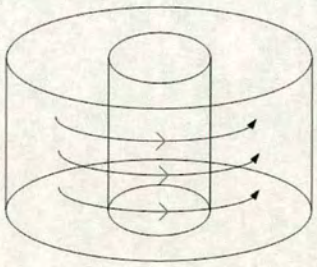

(d)

Figure 5.1: *(a) CVO rheometer (Bohlin Instruments) fitted with coaxial cylinder geometry (roughened cup and bob and double gap). (b) Experimental set-up showing a transparent cup used to observe the flow and determine the optimal shear rate at which dilute systems sedimentation is prevented. (c) Representation of the principle of the coaxial cylinder rheometer working on controlled shear mode. Torque/shear rate is measured on the rotor axis. Outer cylinder is stationary. (d) Flow pattern in a rotational rheometer/viscosimeter, describing a laminar (steady) and one dimensional flow.*

Principle of the rotational rheometer

Experimentally the viscosity cannot be measured directly, commonly it is calculated from the relationship between shear stress and shear rate, which are linked directly to the basic units of physics: force, length and time as described by Eq. (5.2).

One of the most versatile measuring systems, used today to solve all kinds of rheological problems, is the rotational rheometer. This instrument is known as absolute rheometer as it can subject fluids to defined shear rates and measure the resulting shear stress or vice versa. The principle of a coaxial cylinder rheometer working on controlled shear mode is shown in Fig. 5.1c. The coaxial cylinder rheomether comprises an outer cylinder (cup), which is jacketed for an accurate temperature control of samples, and an inner cylinder (rotor) which is driven by a motor, M. Its speed is controlled for a constant or programmed rotor speed while the other cylinder is stationary.

The flow of a fluid sample filling the annular gap between two cylinders, of such system, is described as follows [118]:

1. the driven inner cylinder forces the liquid in the annular gap to flow.
2. the resistance of the liquid being sheared between the stationary and the rotating boundaries of the system results in a viscosity-related torque working on the inner cylinder which counteracts the torque provided by the drive motor. A torque detector, normally a spring that twists as a result of the torque applied is placed between the drive motor and the shaft of the inner cylinder.
3. the twist angle of the torque spring is a direct measurement of the viscosity of the sample.

For rotational rheometers it is assumed that always the flow of the fluid in the measuring system is laminar (steady) and one dimensional. This means that no variation with time occurs and the fluid moves only in the direction of rotation, as shown in Fig. 5.1d. Commonly for narrow gaps and modest rotational speeds, a steady flow is achieved and satisfactory viscosity data are registered.

Types of rheological behaviour

The viscosity can be independent of the shear strain rate (in which case the fluid is said to exhibit Newtonian viscosity) or dependent on the shear strain rate (non-Newtonian viscosity).

Fluids that exhibit Newtonian viscosity (e.g., water, alcohols, some oils and glasses) are relatively easy to characterize. Most particulate suspensions of interest to cement industry are non-Newtonian.

A tremendous amount of experimental work on flow characterization for different type of fluids has been reported in the literature [42, 45, 56, 57, 77, 107, 111, 112]. The majority are based either on the measurement of the shear stress as function of the rate of deformation or on shear viscosity as function of shear strain rate. An example of typical rheograms used to characterize flow properties in fluids are shown in Fig. 5.2.

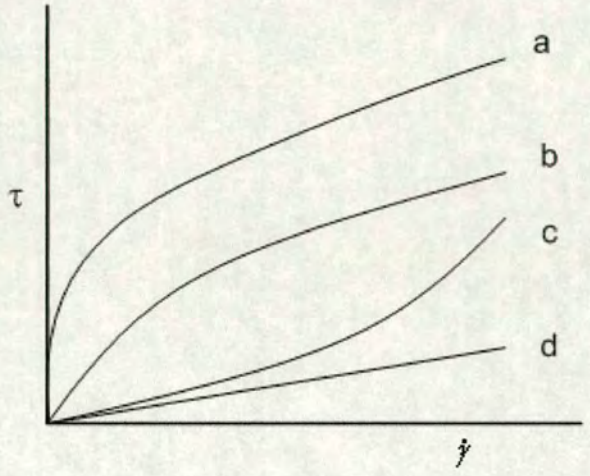

Figure 5.2: *Typical rheograms encountered in fluids; a - plastic (showing flow above a yield stress, corresponding to the transition from elastic to plastic deformation) b - pseudoplastic (shear thinning), c - shear thickening, d - Newtonian.*

As shown schematically in Fig. 5.2, the different types of viscous response to a shear stress can be illustrated by plots of the shear stress versus shear strain rate (or alternatively by plots of the viscosity versus shear strain rate). The simplest case represents the Newtonian behaviour.

5.2.5 Rheological models

An empirical expression commonly used for non-Newtonian, shear thinning fluids is the Ostwald-de Waele [6] or power-law expression:

$$\tau = K\dot{\gamma}^n \tag{5.3}$$

where K is a constant (consistency), and n is the power-law index, < 1 for shear thinning fluids.

In some cases below a critical stress τ_0 (the yield stress) the material behaves effectively like a solid then flows like a viscous liquid when this stress is exceeded ($\tau > \tau_0$), often as a power-law fluid. The Herschel-Bulkley model describes well such viscoplastic materials exhibiting a yield response, with a power-law relationship (Eq. (5.3)) above the yield stress τ_0:

$$\tau = \tau_0 + K\dot{\gamma}^n. \tag{5.4}$$

The Herschel-Bulkley relation (Eq. (5.4)) reduces to the equation of a Bingham plastic when $n = 1$. The ideal Bingham material is an elastic solid at low shear stress values and a Newtonian fluid above a critical value called the Bingham yield stress.

Usually fluids display Newtonian behaviour at low stresses/shear rates before displaying shear thinning, sometimes followed at high shear rates by a second, lower-valued upper Newtonian region. One equation which describes this flow behaviour is the Cross-model :

$$\frac{\eta - \eta_\infty}{\eta_0 - \eta_\infty} = \frac{1}{1 + (\lambda\dot{\gamma})^m} \tag{5.5}$$

where η_0 and η_∞ are the asymptotic values of viscosity at low and very high shear rates respectively, λ has the units of time and m is a shear index which is dimensionless. The degree of the shear thinning is dictated by the value of m. When m approaches zero the fluid is Newtonian, while increasing negative values of m indicate increasingly shear-thinning behaviour. This simple model was chosen because it has fewer parameters than alternatives such as the Carreau model [9] and will be seen to represent the experimental data with a single analytic curve, in preference to a piecemeal fit such as the truncated power law model [84].

5.2.6 Dependence on particle shape and concentration

For very low particle concentrations the relative shear viscosity η_{rel}, as a function of the volume fraction ϕ, is given by the Einstein equation:

$$\eta_{rel} = \frac{\eta_s}{\eta_0} = 1 + [\eta]\phi \tag{5.6}$$

where η_s is the suspension viscosity, η_0 the solvent viscosity and $[\eta]$ is a particle shape dependent factor called the intrinsic viscosity. For hard spherical particles $[\eta] = 2.5$ and for rods with an aspect ratio of 22.4, $[\eta] = 50.2$ [138]. This equation describes only particle-fluid interac-

tions and does not include the hydrodynamic action of one particle upon another and so holds only for very dilute suspensions.

At higher concentrations the shear viscosity of spherical particle suspensions can be related to the maximum packing fraction, ϕ_c, by equations such as the semi-empirical Kreiger-Dougherty equation [4]

$$\eta_{rel} = (1 - \phi/\phi_c)^{-[\eta]\phi_c}. \tag{5.7}$$

For elongated particles the shear viscosity of the rods is related to the rotational diffusion behaviour [38].

In the semi-dilute concentration regime $r_i^{-2} \ll \phi \ll r_i^{-1}$ (r_i - particle aspect ratio, L/d where L is the rod length and d the rod diameter) the 'tube'model proposed by Doi and Edwards [35, 36] predicts that the shear rate viscosity is given by:

$$\eta \simeq \eta_s \left[1 + (\phi r_i^2)^3\right]. \tag{5.8}$$

Doi and Edwards [35, 36] performed an extensive study on rod-like macromolecules in concentrated solution. They found out that the shear viscosity of rods diverges at lower density then any other systems due to restrictions of rods rotational dynamics. Those restrictions take place when the rod number density is exceeding L^{-3}. The rotational, end-over-end motion of each rod is severely restricted as well as the translation motion perpendicular to the rods axes and a permanent overlap could take place (as shown in Fig. 5.3a and b). Consequently, the dynamics of such system is very different from those of dilute ones due to rods 'entanglement' (rods cannot pass through each other). In the semi-dilute regime the rods are orientationally disordered and the constraints between the rods will reduce the rotational diffusion constant, D_r, from the dilute system value D_{r_0} to:

$$D_r \simeq \beta D_{r_0}/(\phi r_i^2)^2 \tag{5.9}$$

where β is a measure of the release of the tube-constraints. For dilute suspensions the rotational diffusion coefficient is given by:

$$D_{r_0} = \left(\frac{kT}{3\pi\eta_s L^3}\right) \ln\left(\frac{r_i}{3}\right) \tag{5.10}$$

where η_s is the viscosity of the solvent and L is the length of the rod.

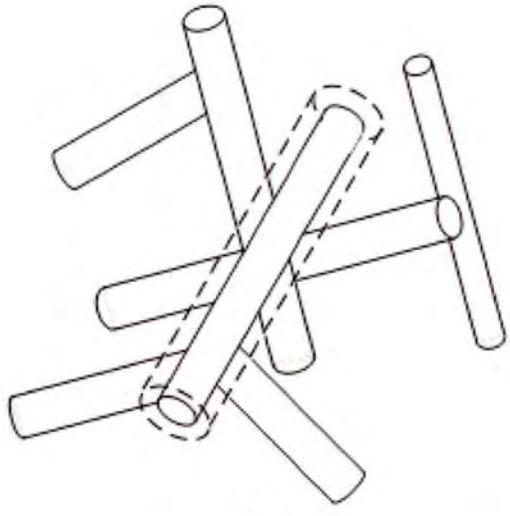

(a)

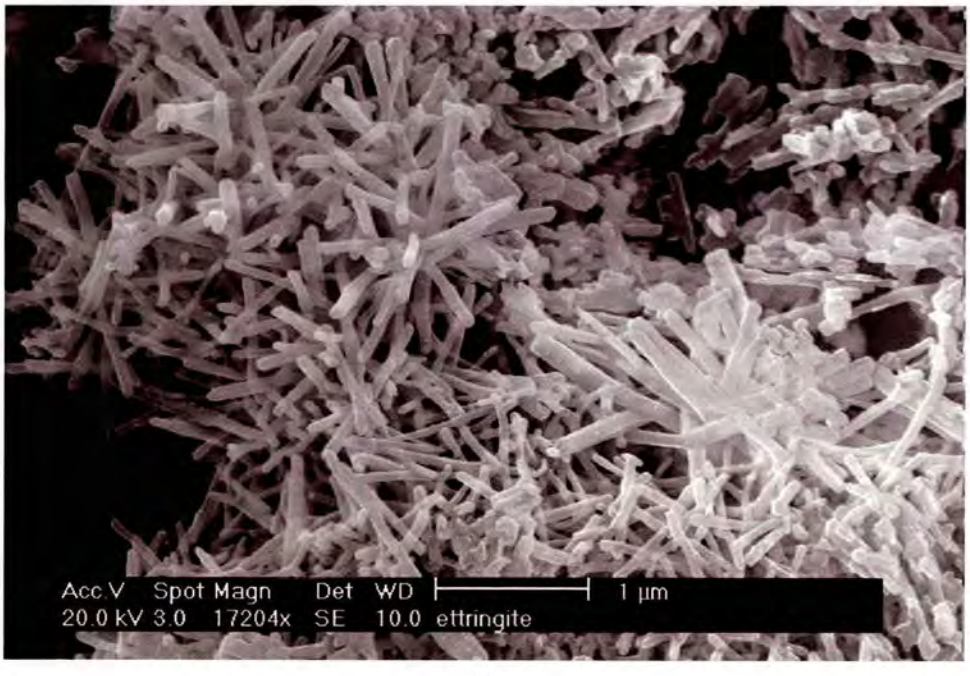

(b)

Figure 5.3: *(a) Sketch showing highly entangled rods, where due to constraints the rod diffuse only in the direction of its own axis, changing its direction gradually. (b) Comparative SEM micrograph showing, in the same manner, ettringite needle strongly entangled. The structures were grown, in the present study, for a solid volume fraction,* $\phi = 0.05$.

The associated rotational relaxation time τ_r is $(6D_{r_0})^{-1}$. Competition between shear forces and Brownian motion gives rise to shear thinning effects which increase as a function of the Péclet number:

$$Pe_{rot} = \tau_r \dot{\gamma} = \dot{\gamma}/6D_r. \tag{5.11}$$

Doi and Edwards [35] predicted that semi-dilute suspensions of rods would have a constant viscosity up to a Péclet number of around unity and thereafter show shear-thinning behaviour. Hinch and Leal [65] and others have also associated a change over of flow regimes with $Pe_{rot} \simeq 1$ although the precise definitions of D_r and Pe_{rot} can vary slightly between authors [138].

5.3 Results and discussion

5.3.1 Ettringite particle characteristics

It was found that ettringite suspensions at ambient temperature consisted of crystal-like needles (rods) with an estimated aspect ratio, r_i, between 4 and 16 (Fig. 5.4a). The rods are fibrous, thin, hexagonal in cross-section (see Fig. 5.4b) and have a length $0.2-2.2\mu$m and cross-section diameter $\leq$ 200nm.

A study was performed on 6 specimens with different solid volume fractions from 0.03 to 0.1. Approximately 15 particles were measured from each sample. The length and diameter of ettringite particles were measured using the protocol stated in section 2.2. The resulting data were plotted as a cumulative distribution function and a median of $r_i = 8.4$ was extracted for better statistics (Fig. 5.5).

Polydispersity is known to have a significant effect on the build-up of stress in a suspension [139]. The ratio of the mean value to the standard deviation (coefficient of variance) can be also used as a measure for polydispersity. Typically, a polymer latex system will be regarded as monodisperse if the coefficient of variance is less than 10% [66]. Here we measured a spread of diameter and length for ettringite rods with a variation coefficient of 47% and 57% respectively. The mean aspect ratio was approximately 9 with a coefficient of variance of 37%. Examination of r_i for many samples as a function of particle length/volume revealed that this quantity was essentially independent of particle size.

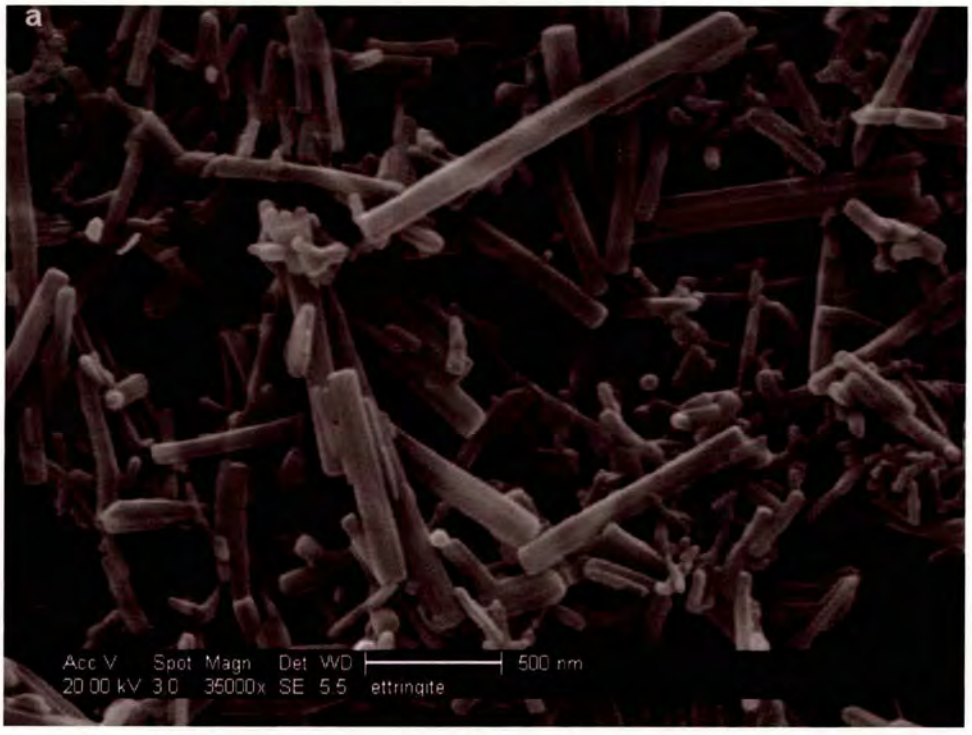

(a)

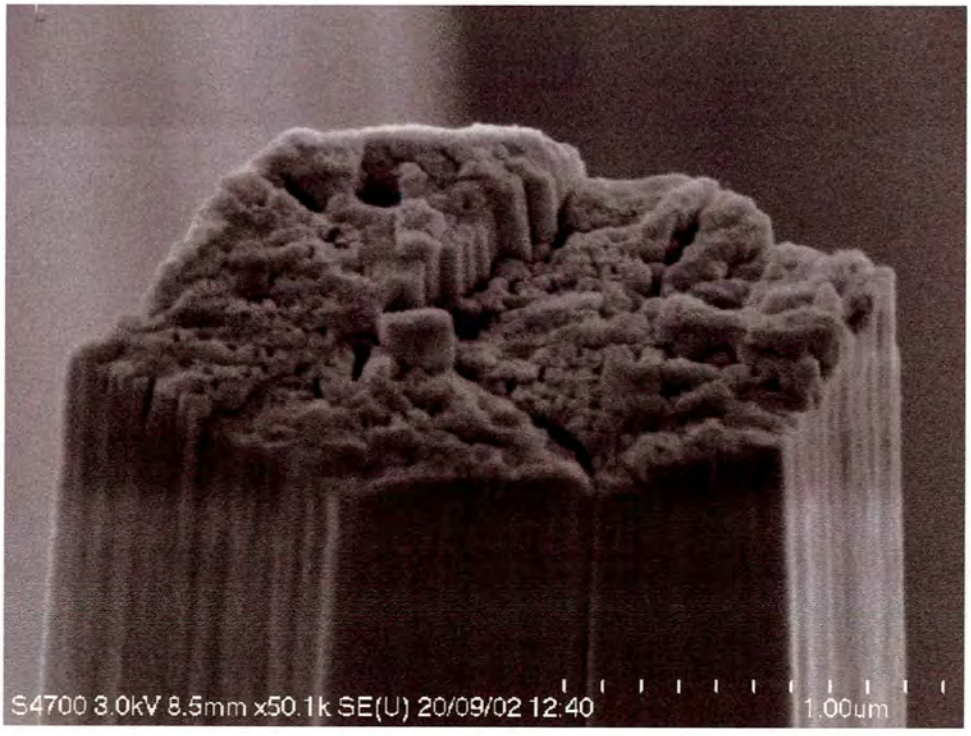

(b)

Figure 5.4: *(a) Scanning electron micrograph of fresh ettringite grown for a solid volume fraction, $\phi = 0.03$. (b) Hexagonal cross-section of an ettringite crystal grown by cooling from a supernatant with low supersaturation.*

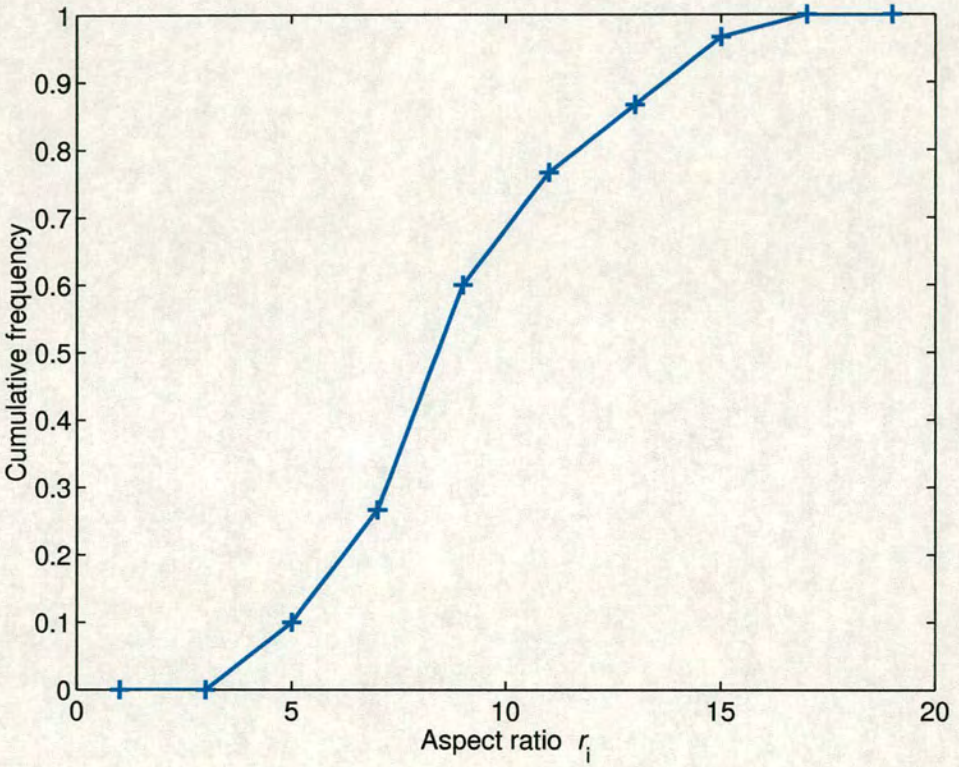

Figure 5.5: *Cumulative frequency plot showing a median value* $r_i = 8.4$. *A sample of* $n = 30$ *particles was measured.*

To summarize, the ettringite particles at ambient temperature are hexagonal rods of mean length of $\sim 1\mu m$, mean aspect ratio r_i of 9 and median r_i of 8.4. The system was moderately polydisperse but with an aspect ratio statistically independent of particle size. Hence, a single median aspect ratio $\langle r_i \rangle$ of 8.4 was used later, in the data interpretation.

5.3.2 Flow curves of ettringite suspensions

The rheological behaviour of ettringite suspensions for eight different solids volume fractions, ϕ, in the interval 0.01 - 0.08 was investigated at shear rates from 1 to $100s^{-1}$. The shear viscosity as a function of shear rate is shown in Fig. 5.6.

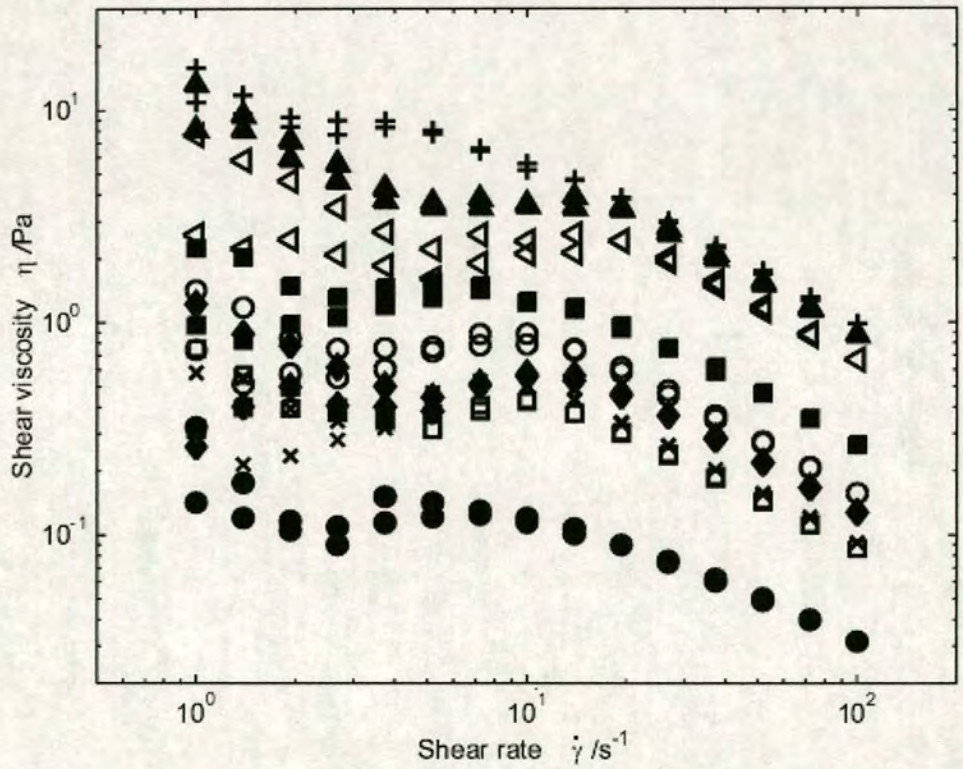

Figure 5.6: *Shear viscosity of rod-like ettringite suspensions dependence on different solids content as a function of the shear rate applied. Suspensions at nine volume fractions from 0.01 to 0.08 are shown as follows: 0.01* (•), *0.02* (□), *0.025* (♦), *0.03* (×), *0.04* (○), *0.05* (■), *0.06* (◁), *0.07* (▲), *0.08* (+).

Above a critical shear rate, $\dot{\gamma}_c$, of about $10s^{-1}$, the material becomes shear-thinning. At low shear rates, though the experimental data present some fluctuations, the lower viscosity is essentially constant. $\dot{\gamma}_c$ decreases slightly with increasing volume fraction being $\sim 2s^{-1}$ for $\phi = 0.08$.

For ramps of shear rate up and down, very similar curves were measured above $10s^{-1}$, which is a good evidence that a steady state was achieved at each shear rate.

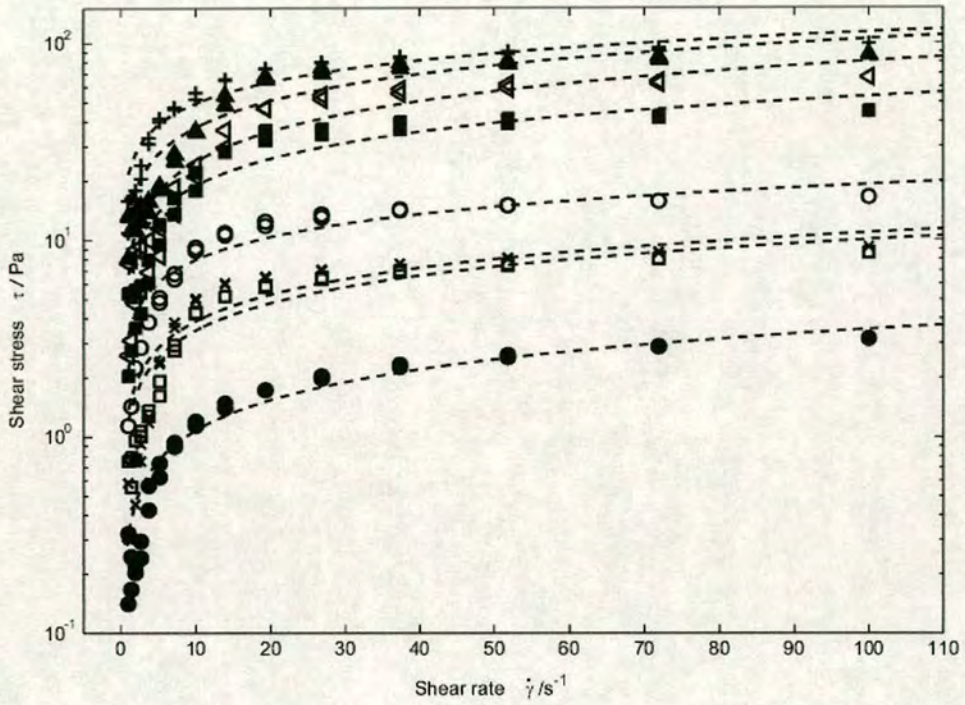

Figure 5.7: *Shear stress versus shear rate over a range of different solid contents, compared with the predictions of Ostwald-de Waele, equation 5.3. The ettringite data are shown for volume fractions of 0.01* (•), *0.02* (□), *0.03* (×), *0.04* (○), *0.05* (■), *0.06* (◁), *0.07* (▲), *0.08* (+). *The drawn lines are the Ostwald-de Waele fits. The fit-parameters are listed in Table 5.1.*

The shear stress-strain rate curves for increasing ϕ are shown in Fig. 5.7, where the low shear rate behaviour can be seen more clearly. This figure also displays the best fit power law models, which give a good description of the data above $\sim 5s^{-1}$. The best-fit parameters for the power-law model are given in Table 5.1.

The consistency, K, is strongly dependent on the solid volume fraction, ϕ, whilst the power-law index is essentially independent of ϕ at the moderately shear-thinning value of 0.5. The data at $\phi = 0.02$ and 0.03 seems to fall on the same curve. This could be due to sample artifacts such as sample aging, inhomogeneities and remaining chemistry. However, this difference is believed do not affect the trends of the results.

ϕ^a	K^b	n^c
0.01	0.33	0.51
0.02	1.20	0.46
0.03	1.38	0.44
0.04	3.31	0.38
0.05	6.70	0.45
0.06	7.78	0.50
0.07	13.38	0.45
0.08	21.63	0.36

[a] ettringite volume fraction
[b] consistency
[c] power law index

Table 5.1: *Best fit parameters*

The existence of a yield stress has been also investigated. There is some evidence of a developing yield stress for ϕ above 0.06 (see Fig.5.7 and the slightly diverging low shear viscosity in Fig. 5.6) as the system approaches $\phi = r_i^{-1} \sim 0.1$. However data at lower shear rates /stresses than were studied here would be required to resolve this issue.

The data in Fig. 5.8 demonstrate that the Cross model can be considered a reasonable description for the system in the range of applied shear rates from 1 to 100s^{-1}. Some of the data on the Newtonian plateau at low shear rates display some differences between the shear rate ramp-up and ramp-down curves. Some of this is random scatter, but there are indications that in some cases the measurement times at low shear rates were not quite long enough for a steady state to be reached. For such data, the model has been fitted to the average of the up and down ramp curves. The zero shear rate viscosities so obtained are believed to be realistic for each concentration and the uncertainties introduced do not materially influence the subsequent discussion and conclusions.

The model fit parameters are given in Table 5.2. As the ratio between the two Newtonian plateaux is a strong function of aspect ratio [138], we have fixed the viscosity at infinite shear rate to be $\eta_\infty = \eta_0/0.85r_i$. The parameter m was chosen to take the value 1.5 to describe the shear thinning region. With some scatter in the experimental data we find that the viscosity at low shear is a strong function of ϕ, while the parameter λ is essentially independent of ϕ. As ϕ approaches 0.1 the parameter λ increases and we observe a narrow low shear viscosity plateau. At the highest measured concentration (ϕ = 0.08) the system is markedly more shear-thinning and fixing η_∞ at the dilute limit results in a poorer fit to the data. This can be resolved by increasing η_0/η_∞ to 40 and reducing m to 1.15 (see Fig 5.8).

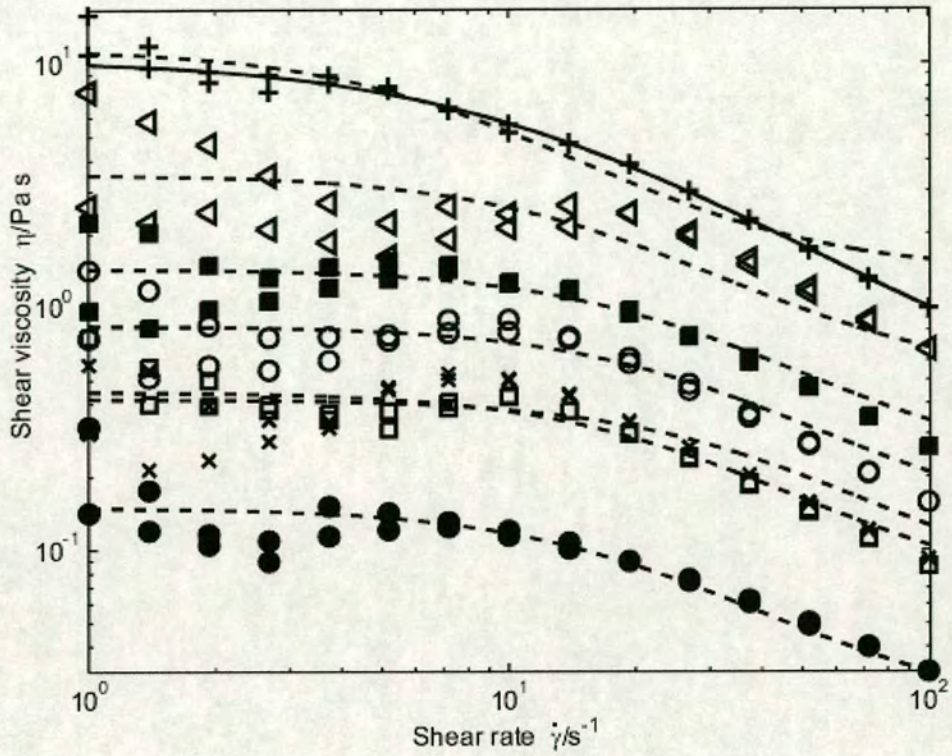

Figure 5.8: *Cross-model describing ettringite suspensions flow with asymptotic viscosities at zero and infinite shear rates. Solid volume fractions: 0.01 (•), 0.02 (□), 0.03 (×), 0.04 (○), 0.05 (■), 0.06 (◁), 0.08 (+). Dashed lines represent the Cross model fit with the infinite shear viscosity fixed at $\eta_\infty = \eta_0/0.85r_i$ and m = 1.5. The solid curve shows an alternative fit for the highest concentration suspension with m = 1.15 and $\eta_\infty = \eta_0/4r_i$.*

ϕ^a	$\eta_0{}^b$	λ^c
0.01	0.14	0.046
0.02	0.45	0.039
0.03	0.42	0.025
0.04	0.84	0.034
0.05	1.44	0.038
0.06	3.46	0.053
0.08	11.58	0.139

[a] solid volume fraction
[b] viscosity at zero shear rate (Pa s)
[c] constant with units of time

Table 5.2: *Best fit parameters of Cross model for m = 1.5 and $\eta_\infty = \eta_0/0.85r_i$*

However, since the interpretation of these data will focus only on η_0, further refinement of fitting the whole flow curve was was not pursued.

For values of ϕ below 0.01, the absolute viscosities determined at $20s^{-1}$ are given in Table 5.3.

ϕ^a	$\eta_{20s^{-1}}{}^b$
0.0001	1.55
0.0005	2.95
0.001	3.80
0.003	9.05
0.005	26.54
0.01	90.86

[a] ettringite volume fraction
[b] absolute viscosity at $20s^{-1}$ expressed in mPa s

Table 5.3: *Absolute viscosities determined at* $20s^{-1}$

5.3.3 Comparison with models

Calculations show that for all suspensions studied the natural electrolyte concentration of the stock slurry is sufficiently high that the Debye length is always less than 5nm. The Debye length was estimated using the ionic strength based on the solubility product of the natural electrolyte at equilibrium, $\log K_{sp} = 44.43$ [31]. This is negligible compared to the dimensions of the rods and indicates that we may interpret the rheological data assuming hard body interactions, with negligible long-range electrostatic effects.

We have seen that as the ettringite particle concentration is increased, particle-particle interactions cause the dynamics of the flow to become more complex. In very dilute systems ($\phi \ll r_i^{-2}$) of rod-like particles the flow properties are only governed by hydrodynamic interactions with the fluid.

Fig. 5.9 shows the low shear relative viscosity as a function of volume fraction ϕ. The experimental points were chosen such that the volume fraction falls in the dilute concentration range, $\phi < r_i^{-2}$, typically described by equation 5.6. Although the dependence of η_{rel} on ϕ is essentially linear in the range $0.01 < \phi/\phi^* < 0.3$ ($\phi^* \sim r_i^{-2}$), the slope is much higher than that predicted by equation 5.6 using $[\eta] \sim 10$ for rods of aspect ratio $r_i = 8.5$ [138], indicating that even in this concentration range the system is far from the infinite dilution limit.

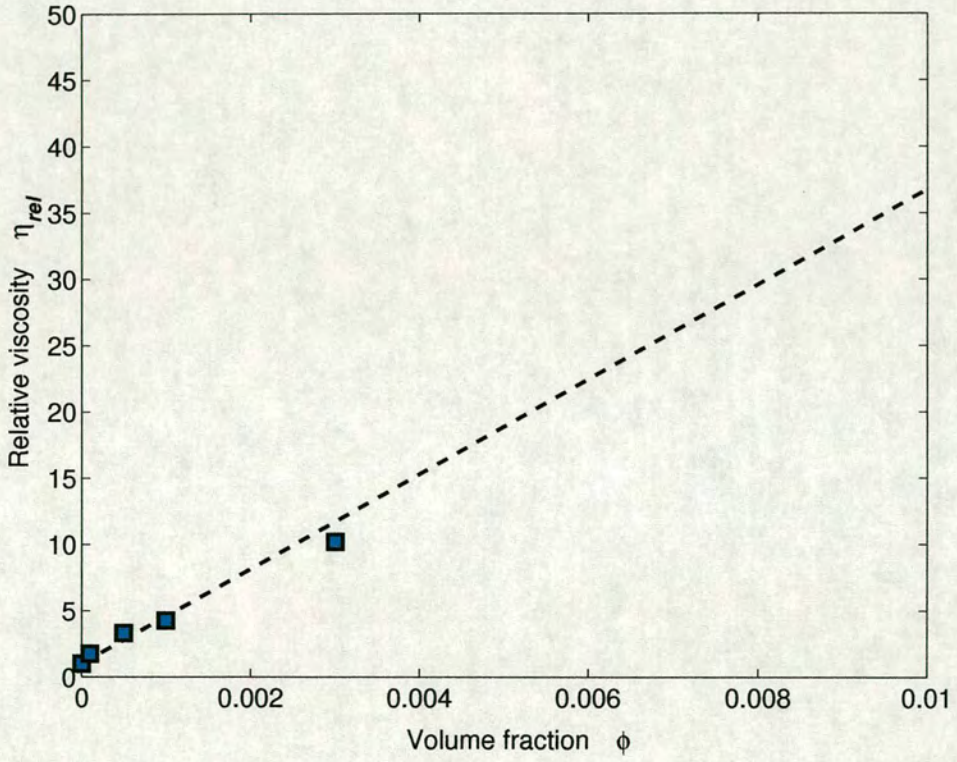

Figure 5.9: *Relative low shear viscosity, $\eta_{20s^{-1}}/\eta_{H_2O}$, as a function of ettringite rod volume fraction. The line has a slope of approximately 3000, far in excess of $[\eta] \sim 10$ for rods of this aspect ratio. The value of η_{H_2O} at 25°C was taken to be 0.89 mPa s.*

We estimate the minimum overlap concentration for those ettingite suspensions, based on the experimental value $\langle r_i \rangle$, to be $\phi^* = 0.01$. For $\phi > 0.01$ we expect a transition towards the semi-dilute regime.

Fig. 5.10 shows the viscosity dependence on the solid volume fraction, ϕ. Also shown is the Doi-Edwards model prediction, equation 5.8, and the Krieger-Dougherty model equation 5.7 using $[\eta] = 10$ and 3 . It can be seen that the viscosity of the suspensions does indeed increase with solid volume fraction, ϕ, with a marked change of slope at around $\phi^* \sim 0.01$. The data are in fact remarkably consistent with the Doi-Edwards prediction [35, 36] and the transition from the dilute to the semi-dilute regime is clearly seen at a value of ϕ^* consistent with the particle size and shape. An alternative way to examine the data is in terms of the Péclet number. Using the mean value of L and $r_i = 9$ in equation 5.10, we estimate the mean rotational diffusion coefficient of the ettringite rods at infinite dilution to be 1.3s^{-1}. We therefore expect the onset of shear-thinning behaviour at $Pe_{rot} \simeq 1$ ie. at $\dot{\gamma} \simeq 6D_r \simeq 8\text{s}^{-1}$, essentially in agreement with experimental observation for the most dilute suspension for which accurate full flow curves could be obtained, $\phi = 0.01 = \phi^*$. As ϕ increase above ϕ^*, $\dot{\gamma}_c$ decreased but not as rapidly as predicted by equation 5.10.

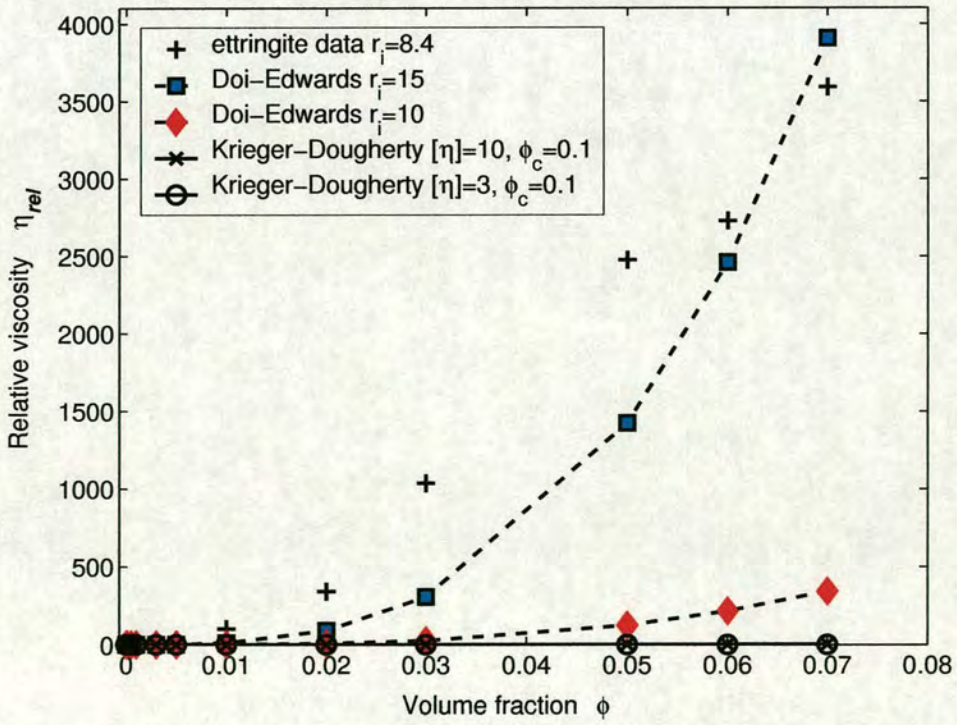

Figure 5.10: *Shear viscosity of ettringite rods suspensions as a function of the particle volume fraction for a shear rate of* 20s^{-1}.

5.4 Conclusions

We have studied the effect of particle volume fraction and rod size and aspect ratio distribution on the shear rheology of ettringite suspensions. Suspensions of ettringite rods were synthesized using commercial grade reagents in the appropriate stoichiometric amounts as previously described by Hall et al. [59]. The synthesis protocol is critical since the method is known to produce diverse morphology in different conditions (chapter 4). Using this method we have prepared ettringite rods, hexagonal in cross-section with aspect ratio, r_i, between 4 and 16. The ettringite particles were well-characterized by electron microscopy so that the effect of shape and size on the shear rheology was successfully studied.

We have investigated the rheology of ettringite suspensions with ϕ between 0.0001 - 0.08. Although the system is very complex, the rheological behaviour of ettringite rod-like particles compares remarkably well, within a factor of 2 to 3, with semi-empirical and physical predictions.

The general flow curves show a strong shear thinning behaviour for $\dot{\gamma}_c \sim 10\text{s}^{-1}$, well described by the Ostwald-de Waele model. Little evidence of a yield stress was found as the system approaches $\phi = 0.1$. $\dot{\gamma}_c$ decreases slightly with increasing volume fraction being $\sim 2\text{s}^{-1}$ for $\phi = 0.08$.

At low shear rates the viscosity is essentially constant. The Cross model is a reasonable description of the system in the range of applied shear from 1 to 100s^{-1}.

The intrinsic nature of the background electrolyte eliminated the long-range electrostatic effects and allows us to assume hard body interactions for rheological data interpretation. The viscosity at zero shear rate is a strong function of ϕ in line with that expected from the Doi-Edwards model for rod-like suspensions.

We report a quantitative description of the system by the Doi-Edwards prediction, with a marked change of slope at $\phi \sim 0.01$. The minimum overlap concentration ϕ^* (the value of ϕ at which the rods start to interact significantly) was found to coincide with the experimental break point around $\phi = 0.01$. Hence the complex ettringite system displays a rheology which can be interpreted semi-quantitatively using well established rheological models and principles. We are therefore now in a position to predict how an ettringite dominated suspension might behave as the rods nucleate and grow, and to some extent even aggregate.

5.5 Significance of the ettringite flow behaviour for cement slurry rheology

As was highlighted in the introductory section ettringite is a key mineral with large implications in early hydration of cement systems. Because it is one of the earliest hydration products, the rheological property evolution of a cement suspension in water is very often related to its formation. Therefore the results presented in this study have direct significance for the cement slurry rheology experiencing similar conditions to those presented here.

Typically cement suspensions behave like Bingham-fluids [5]. Usually, three parameters such as the relative yield value, the relative viscosity coefficient and the stiffening value, are investigated to predict their flow behaviour. Past studies on cement suspensions rheology [5, 72, 79] have identified increased values of the yield stress and viscosity caused by the hydration products formation, which are believed to strengthen the bonds between cement particles. Also, the relative yield value was found to increase with increasing temperatures from 8 to 30°C due to a boost in the ettringite content. More specifically the cement particles are eventually interconnected by the ettringite rods and held together by the early gel (calcium silicate hydrate), forming a three-dimensional, space-filling network. This network is possibly responsible for a progressive increase in the yield stress.

The data on ettringite rheology brings clear evidence of a developing yield stress above a volume fraction of 0.06 and approaching 0.1, the maximum estimated value of the ettringite volume fraction in the continuous phase of the cement slurry. It was found that increasing ettringite solids content results in higher shear stresses at lower characteristic shear rates. A corresponding contribution to the overall yield stress value of the cement slurry is therefore expected under similar conditions.

The results also shows that the non-Newtonian flow behaviour of ettringite is governed by the shape of the particles, their size distribution, concentration and surface properties. It was found that the high effective hydrodynamic volume of rotating rods dominates the rheological behaviour of ettringite suspensions. This is further evidence that not only the amount of hydrated product is important in determining the rheology of cements during early hydration but more the morphology and the interparticle force are decisive factors.

This study is now in the position to give understanding of several speculations made to explain increased failure strain measurements in cement suspensions. This effect was associated with a

change in the nature of the forces that holds the cement particles together or with a yield stress very sensitive to the amount of hydration product whereas the failure strain is sensitive to the dominant interparticle force [79].

Although this study was restricted to ettringite rheology alone, it is reasonable to think that the trends that have been observed here could be extended to the cement systems.

Chapter 6
Conclusions and future work

6.1 Synthesis of calcium aluminosulphates: reactions, stoichiometry, analysis of products, stability

Chapter 2 presents a novel synthesis method to produce monosulphate hydrate. Microwave radiation was successfully employed to overcome the constraints of pre-existing synthesis methods, which mainly result from solving the equilibrium diagrams in the C-$\overline{S}$-A-H system. The attractive properties of the microwaves in the rapid and controllable synthesis of monosulphate have been demonstrated here. The relatively long reaction times were halved and the yield was substantially improved. This allowed the use of the synthesized product in a subsequent study, to explore the hydration stages of monosulphate hydrate in varying conditions of relative humidity. A stability map of monosulphate at relative humidities from 10 to 100% and temperatures up to 100°C is shown in Fig. 6.1.

Of particular interest are the rehydration experiments where lower hydrates were reverted back to higher hydrates. A new in-situ X-ray diffraction experiment was designed as described in chapter 2 to observe monosulphate 12-hydrate rehydration to monosulphate 14-hydrate. The outcome of this work proves new capabilities of laboratory X-ray diffraction instruments to produce in-situ experiments but with certain restrictions.

New information on the stability of monosulphate and ettringite is supplied by the synchrotron energy dispersive study in Chapter 3. In the first part of this work all the uncertainties emerging from Chapter 2 with regard to the reaction products were solved. The product of the reaction when still moist with the mother liquor was monosulphate 14-hydrate and on cooling to ambient temperature, no disproportion to form ettringite was observed.

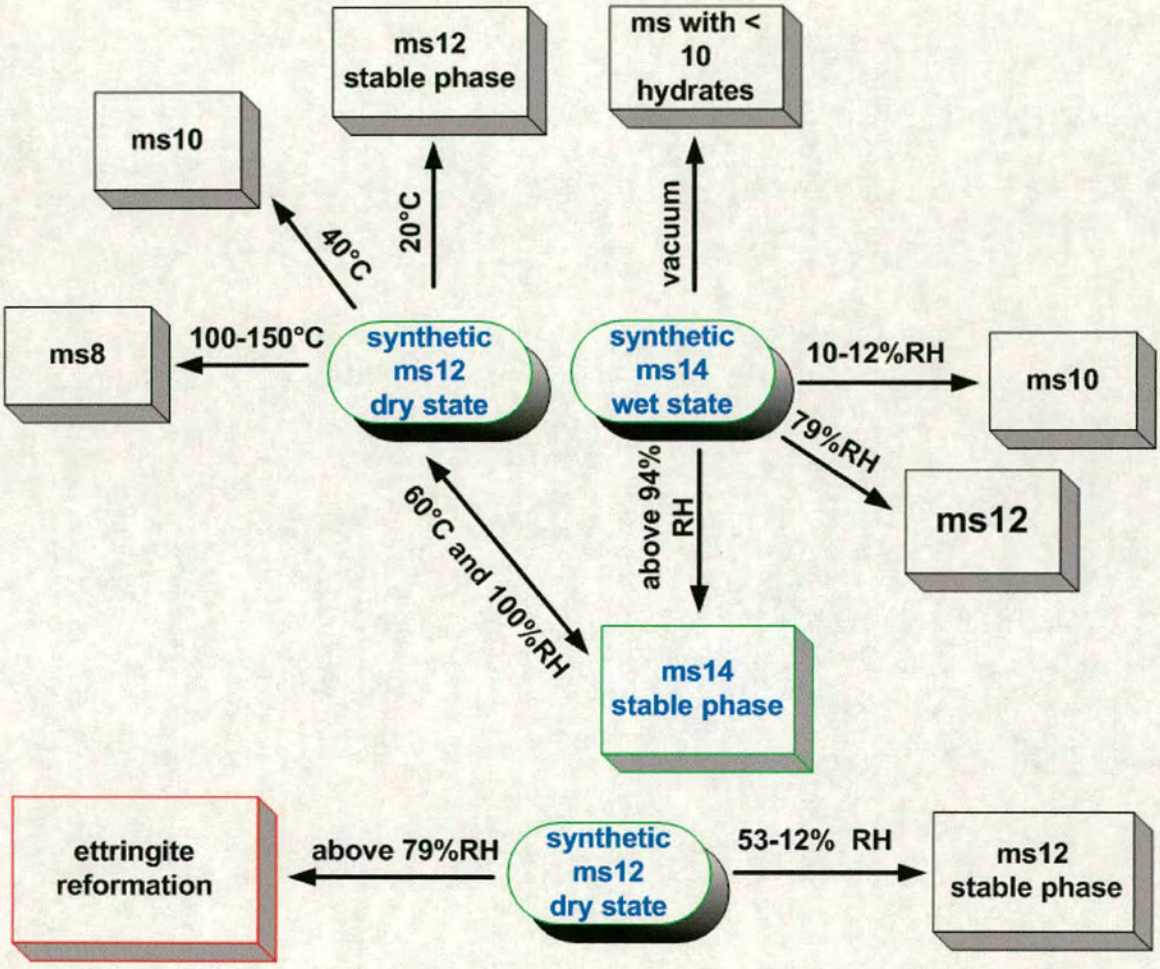

Figure 6.1: *Schematic representation of monosulphate stability derived from the data such as those presented in Chapter 2. The stability map of monosulphate was built for relative humidities from 10 to 100% and temperatures up to 150°C. Key: ms(x) = calcium aluminium monosulphate hydrate ($C_4A\overline{S}H_n$), where x = n = 8, 10, 12, 14 denote the number of water molecules present in the sample, RH = relative humidity.*

In the second part of Chapter 3, the combined action of temperature and alkali was found to increase the extent of monosulphate formation and 'U - phase' was observed in opposition to the study of Damidot and Glasser [31], which indicates that sodium will not be incorporated into the solid phase. All stable phase assemblages were identified for up to 150°C and 1M NaOH and mapped in Fig. 6.2.

Further work would include taking this study one stage further, to establish the stable phase assemblages for up to 1M alkali and 250°C, when monosulphate-14 is possibly decomposing to a mixture of beta-anhydrite and hydrogarnet (Hall&Meller, unpublished work).

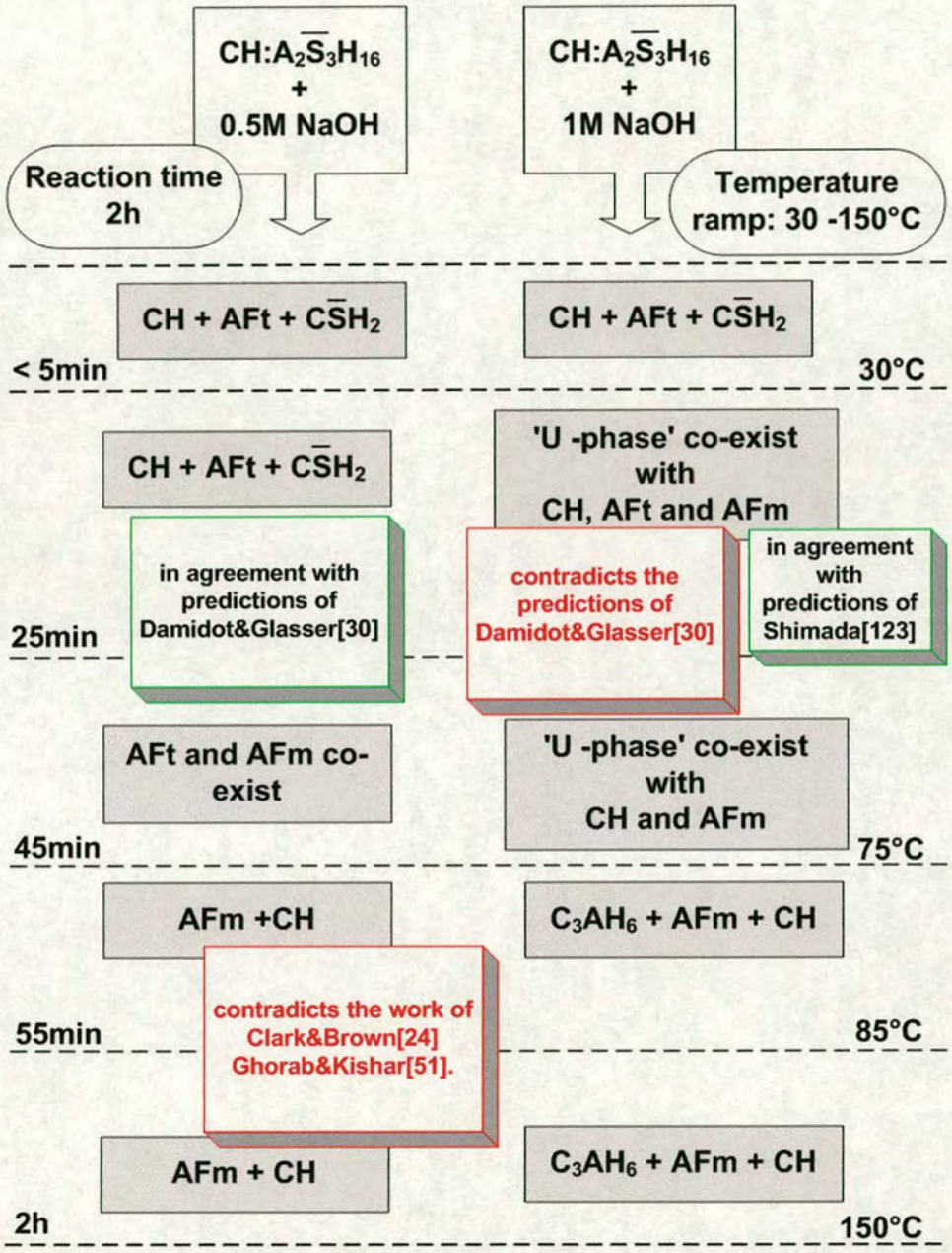

Figure 6.2: *Summary of the stable phase assemblages identified for up to 150°C and 1M NaOH. The temperature and time markings are included to give an indication of when each event occurs. Key: CH = Portlandite/$Ca(OH)_2$, AFt = Ettringite/ $Ca_6[Al(OH)_6]_2(SO_4)_3 \cdot 26H_2O$, $C\bar{S}H_2$ = Gypsum/$CaSO_4 \cdot 2H_2O$, AFm = Monosulphate/$Ca_4[Al(OH)_6]_2SO_4 \cdot xH_2O$, C_3AH_6 = Hydrogarnet/$3CaO \cdot Al_2O_3 \cdot 6H_2O$, U-phase = $NaCa_4Al_2O_6(SO_4)_{1.5} \cdot 15H_2O$*

6.2 Ettringite crystal growth

The work reported in Chapter 4 maps the dependence of ettringite morphology on crystal growth conditions. In particular a new cryo-SEM method is used to provide high resolution information on the rather fragile structures of ettringite. The main advantage of this method is that it offers the opportunity to observe specimens under conditions that are closely related to the natural state.

It has been shown qualitatively that temperature is governing the ettringite morphology. Ettringite crystals show high aspect ratios when crystallizing by cooling, whereby crystallization by evaporation produces ten times shorter particles. They are always hexagonal in cross-section with a radial disposal from a central core. However ettringite is remarkable at forming particles with such high aspect ratios which strongly influences the engineering properties, as shown in Chapter 5. Further work would include exploration of other factors which potentially influence the crystallization process, such as the degree of supersaturation, rate of stirring and presence of impurities.

6.3 Ettringite rheology

In Chapter 5, the rheology of ettringite was rationalized for the first time using models devised for model rod systems. Mixing a calcium hydroxide slurry with an aluminium sulphate solution produces a suspension of rod-shaped ettringite particles. Ettringite rod suspensions exhibit non-Newtonian flow behaviour, which depends on the shape of the particles, their size distribution, concentration and surface properties as well as the suspension medium characteristics. We have measured the shear viscosity of suspensions of ettringite rods with a median aspect ratio, $r_i \backsim 8$, at 25°C as a function of particle volume fraction, ϕ, in the range 0.0001 - 0.08. It was found that the viscosity of the suspensions increased with ϕ, and showed a marked change of slope at $\phi \sim 0.01$, which we identified as the minimum overlap concentration ϕ^*. Above ϕ^*, the system is in the semi-dilute regime. At $\phi > \phi^*$, when $\mathrm{Pe_{rot}} > 1$, hydrodynamic interactions between rods become increasingly significant, and we observe shear-thinning behaviour. The high effective hydrodynamic volume of rotating rods, resulting in much lower values of the maximum packing fraction, ϕ_c, than for spheres, dominates the rheological behaviour of ettringite suspensions. All findings listed above demonstrate significant implications of ettringite for the rheological evolution of the cement slurry at early times.

Further work would include data at low shear rates/stresses as it is emerging from this study. Accurate determinations of the yield stress from creep and recovery tests are suggested, thereby avoiding the microstructural breakdown that is typically associated with the measurement of the yield stress from flow curves.

An important package of further work would be the evaluation of superplasticizers on the rheological evolution of ettringite. Superplasticizers are known to alter the mineralogical composition and the morphology of the hydrates formed [110]. They are typically introduced to cement suspensions in order to improve the rheological properties.

Bibliography

[1] **Allmann R.**, (1968) Die Doppelschichtstruktur der plättchenförmingen Calcium-Aluminium-Hydroxisalze am Beispeil des $3CaO \cdot Al_2O_3 \cdot CaSO_4 \cdot 12H_2O$, *Neues Jahrbuch für Mineralogie*, **Monatshefte**, 140-144.

[2] **Atkins M., D. Macphee, A. Kindness and F.P. Glasser**, (1991) Solubility properties of ternary and quaternary compounds in the CaO - SO_3 - Al_2O_3 - H_2O system, *Cement and Concrete Research*, **21**, 991-998.

[3] **Atkins M., F.P. Glasser, L.P. Moroni and J.J. Jack**, (1993) Thermodynamic modelling of blended cements at elevated temperature, Department of the Environment report no: DoE/HMIP/RR/94.011.

[4] **Ball R. and P. Richmond**, (1980) Dynamics of colloidal dispersions, *Physics and Chemistry of Liquids*, **9**, 99-117.

[5] **Banfill P.F.G**, (1991) Rheology of fresh cement and concrete: Proceedings of the International Conference organized by the British Society of Rheology and University of Liverpool, UK, Spon, London, 373.

[6] **Banfill P.F.G**, (2003) The rheology of fresh cement and concrete - A review, *In Proceedings 11th International Cement Chemistry Congress*, Durban, South Africa, **1**, 50-62.

[7] **Bannister F.A., M. Hay and J.D. Bernal**, (1936) Ettringite from Scawt Hill, *Mineralogical Magazine*, **24**, 324-329.

[8] **Barnes P., S.L. Colston, A.C. Jupe, S.D.M. Jacques, M. Attfield, R. Pisula, S. Morgan, C. Hall, P. Livesey and S. Lunt**, (2002) The use of synchrotron sources in the study of cement materials in *Structure and performance of cements*, edited by Bensted J. and P. Barnes, Spon Press, 2nd edition, London, 477-499.

[9] **Barnes H.A., J.F. Hutton and K. Walters**, (1989) *An introduction to rheology*, Elsevier Science B.V., Amsterdam.

[10] **Batchelor G.K.**, (1977) The effect of brownian motion on the bulk stress in a suspension of spherical particles, *Journal of Fluid Mechanics*, **83**, 97-117.

[11] **Bennema P. and J.P. van der Eerden**, (1977) Crystal growth from solution: development in computer simulation, *Journal of Crystal Growth*, **42**, 201-213.

[12] **Bennema P.**, (1977) Crystal growth from solution - theory and experiment, *Journal of Crystal Growth*, **24/25**, 76-83.

[13] **Bennema P.**, (1969) The importance of surface diffusion for crystal growth from solution, *Journal of Crystal Growth*, **5**, 29-43.

[14] **Bennema P.**, (1967) Interpretation of the relation between the rate of crystal growth from solution and the relative supersaturation at low supersaturation, *Journal of Crystal Growth*, **1**, 287-292.

[15] **Berman A.H. and E.S. Newman**, (1963) Heat of formation of calcium aluminate monosulphate at 25°C, *Journal of Research of the National Bureau of Standards - A. Physics and Chemistry*, **67A**(1), 1-13.

[16] **Berry D.H. and W.B. Russel**, (1987) The rheology of dilute suspensions of slender rods in weak flow, *Journal of Fluid Mechanics*, **180**, 475-494.

[17] **Brown P.W. and J.V. Bothe Jr**, (1993) The stability of ettringite, *Advances in Cement Research*, **5**(18), 47-63.

[18] **Brown P.W. and P. LaCroix**, (1989) The kinetics of ettringite formation, *Cement and Concrete Research*, **19**, 879-884.

[19] **Cernik R.J. and P. Barnes**, (1995) Industrial aspects of synchrotron and X-ray powder diffraction, *Radiation Physics and Chemistry*, **45**(3), 445-457.

[20] **Chen Y. and P.K. Mehta**, (1982) Zeta potential and surface area measurements on ettringite, *Cement and Concrete Research*, **12**(2), 257-259.

[21] **Chen Y. and I. Odler**, (1992) On the origin of portland cement setting, *Cement and Concrete Research*, **22**(6), 1130-1140.

[22] **Christensen N.A., T.R. Jensen and J.C. Hanson**, (2003) Formation of ettringite, $Ca_6Al_2(SO_4)_3(OH)_{12} \cdot 26H_2O$, AFt, and monosulphate, $Ca_4Al_2O_6(SO_4) \cdot 14H_2O$, AFm – 14, in hydrothermal hydration of portland cement and of calcium aluminium oxide-calcium sulphate dihydrate mixtures studied by in situ synchrotron X-ray powder diffraction, *Journal of Solid State Chemistry*, **177**, 1944-1951.

[23] **Clark A.B. and P.W. Brown**, (1999) The formation of calcium sulfoaluminate hydrate compounds part I, *Cement and Concrete Research*, **29**, 1943-1948.

[24] **Clark A.B. and P.W. Brown**, (2000) The formation of calcium sulfoaluminate hydrate compounds part II, *Cement and Concrete Research*, **30**, 233-240.

[25] **Clark S.M.**, (1996) A new energy-dispersive powder diffraction facility at the SRS, *Nuclear Instruments & Methods in Physics Research*, **A**(381), 161-168.

[26] **Cohen D.M.**, (1983) Theories of expansion in sulphoaluminate - type expansive cements: schools of thoughts, *Cement and Concrete Research*, **13**, 809-818.

[27] **Colston S.L., P. Barnes, A.C. Jupe, S.D.M. Jacques, C. Hall, P. Livesey, J. Dransfield, N. Meller and G.C. Maitland**, (2004) An in situ synchrotron energy-dispersive diffraction study of the hydration of oilwell cement systems under high temperature/autoclave conditions up to 130°C, *Cement and Concrete Research*, article in press (doi:10.1016/j.cemconres.2004.09.005).

[28] **Colston S.L., S.D.M. Jacques, P. Barnes, A.C. Jupe and C. Hall**, (1998) In-situ hydration studies using multi-angle energy-dispersive diffraction, *Journal of Synchrotron Radiation*, **5**, 112-117.

[29] **Cody A.M., H. Lee, R.D. Cody and P. G. Spry**, (2004) The effects of chemical environment on the nucleation, growth, and stability of ettringite $[Ca_3Al(OH)_6]_2(SO_4)_3 \cdot 26H_2O$, *Cement and Concrete Research*, **34**(5), 869-881.

[30] **Damidot D. and F.P. Glasser**, (1992) Thermodynamic investigation of the CaO - Al_2O_3 - $CaSO_4$ - H_2O system at 50°C and 80°C, *Cement and Concrete Research*, **22**, 1179-1191.

[31] **Damidot D. and F.P. Glasser**, (1993) Thermodynamic investigation of the CaO - Al_2O_3 - $CaSO_4$ - H_2O system at 25°C and the influence of Na_2O, *Cement and Concrete Research*, **23**, 221-238.

[32] **D'Ans J. and H. Eick**, (1953) The quaternary system CaO - Al_2O_3 - $CaSO_4$ - H_2O at 20°C, *Zement-Kalk-Gips*, **6**, 302-315.

[33] **Davey J.D. and J. Garside**, (2000) *From molecules to crystallizers*, Oxford University Press, Oxford, UK.

[34] **Deb S.K., M.H. Manghnani, K. Ross, R.A. Livingston and P.J.M. Monteiro**, (2003) Raman scattering and X-ray diffraction study of the thermal decomposition of an ettringite-group crystal, *Physics and Chemistry of Minerals*, **30**, 31-38.

[35] **Doi M. and S.F. Edwards**, (1978) Dynamics of rod-like macromolecules in concentrated solution; part 1, *Journal of Chemical Society Faraday Transactions 2*, **74**, 560-570.

[36] **Doi M. and S.F. Edwards**, (1978) Dynamics of rod-like macromolecules in concentrated solution; part 2, *Journal of Chemical Society Faraday Transactions 2*, **74**, 918-932.

[37] **Doi M.**, (1975) Rotational relaxation time of rigid rod-like macromolecules in concentrated solutions, *Journal de Physique (France)*, **36**, 607-611.

[38] **Doi M.**, (1982) Rheology of contcentrated suspensions of slender rods, *Advances in Colloid and Interface Science*, **17**(1), 233-239.

[39] **Dosch W. and H. zur Strassen**, (1967) An alkali-containing calcium aluminate sulphate hydrate, *Zement-Kalk-Gips*, **20**, 392-401.

[40] **Dosch W., H. Keller and H. zur Strassen**, (1968) Written discussion, *In Proceedings of the 5th International Symposium on the Chemistry of Cement*, Rio de Janeiro, The Cement Association of Japan, Tokyo, **II**, 72-77.

[41] **Edwards S.F. and K.E. Evans**, (1982) Dynamics of highly entangled rod-like molecules, *Journal of Chemical Society Faraday Transactions 2*, **78**, 113-121.

[42] **Eirich F.R.**, (1969) *Rheology: theory and applications*, Academic Press, New York, London.

[43] **Famy C., K.L. Scrivener and H.F.W. Taylor**, (2002) Delayed ettringite formation in *Structure and performance of cements*, edited by Bensted J. and P. Barnes, Spon Press, 2nd edition, London.

[44] **Fini A. and A. Breccia**, (1999) Chemistry by microwave, *Pure and Applied Chemistry*, **71**(4), 573-579.

[45] **Fredrickson A.G.**, (1964) *Principles and applications of rheology*, Prentice-Hall, Englewood Cliffs.

[46] **Frish H.L. and Simha R.**, (1956) *Rheology: theory and applications*, Academic Press, New York, London.

[47] **Gabriel C., S. Gabriel, E.H. Grant, B.S.J. Halstead, D. Michael and P. Mingos**, (1998) Dielectric parameters relevant to microwave dielectric heating, *Chemichal Society Reviews*, **27**, 213-223.

[48] **Gartner E.M., J.F. Young, D.A. Damidot and I. Jawed**, (2002) Hydration of portland cement in *Structure and performance of cements*, edited by Bensted J. and P. Barnes, Spon Press, 2nd edition, London.

[49] **Geissen C.B. and G.E. Gordon**, (1968) X-ray diffraction: new high speed technique based on X-ray spectrography, *Science*, **159**, 973-975.

[50] **Ghorab Y.H. and E.A. Kishar**, (1985) Studies on the stability of the calcium sulfoaluminate hydrates. Part 1: Effect of temperature on the stability of ettringite in pure water., *Cement and Concrete Research*, **15**, 93-99.

[51] **Ghorab Y.H. and E.A. Kishar**, (1986) Stability of calcium sulfoaluminate hydrates in aqueous solutions, *In Proceedings of the 8th International Congress on Chemistry of Cement*, Rio de Janeiro, **V**, 105-109.

[52] **Ghorab Y.H., D. Heinz, U. Ludwig, T. Meskendhal and A. Wolter**, (1981) On the stability of calcium aluminate sulphate hydrates in pure systems and in cements, *In Proceedings of the 7th International Congress on Chemistry of Cement*, Rio de Janeiro, **IV**, 496-503.

[53] **Giulietti M., M.M. Seckler, S. Derenzo, M.I. Ré and E. Cekinski**, (2001) Industrial crystallization and precipitation from solutions: state of the technique, *Brazilian Journal of Chemical Engineering*, **18**(4), 423-440.

[54] **Goetz-Neunhoeffer F., H. Poellmann**, (1996) Investigations on stability and long-term behaviour of AFm phases at higher temperatures by X-ray powder diffraction methods, *Materials Science Forum*, **228-231**, 615-620.

[55] **Goldstein, J. I.**, (2003) *Scanning electron microscopy and X-ray microanalysis*, Plenum Press, New York.

[56] **Goodwin J.W. and Royal Society of Chemistry, Continuing Education Committee**, (1982) Colloidal dispersions: the papers given at a review symposium on colloid science, University of Bristol, 8th-10th September 1981, Royal Society of Chemistry, London.

[57] **Goodwin J.W. and R.W. Hughes**, (2000) *Rheology for chemists: an introduction*, Royal Society of Chemistry, Cambridge.

[58] **Greenspan L.**, (1977) Humidity points of binary saturated aqueous solutions, *Journal of Research of the National Bureau of Standards*, **81A**(1), 89-96.

[59] **Hall C., P. Barnes, A.D. Billimore, A.C. Jupe and J. Turrillas**, (1996) Thermal decomposition of ettringite $Ca_6[Al(OH)_6]_2(SO_4)_3 \cdot 26H_2O$, *Journal of Chemical Society, Faraday Transactions*, **92**(12), 2125-2129.

[60] **Hampson J.C. and J.E. Bailey**, (1983) The microstructure of the hydration products of tri-calcium aluminate in the presence of gypsum, *Journal of Materials Science*, **18**, 402-410.

[61] **Hanic F., I. Kaprálik and A. Gabarisová**, (1989) Mechanism of hydration reactions in the system $C_4A_3\overline{S} - C\overline{S} - CaO - H_2O$ referred to hydration of sulphoaluminate cements, *Cement and Concrete Research*, **19**, 671-682.

[62] **Hartman M.R. and R. Berliner**, (2005) Investigation of the structure of ettringite by time-of-flight neutron powder diffraction techniques, *Cement and Concrete Research*, article in press (doi:10.1016/j.cemconres.2005.08.004).

[63] **Hartman P.**, (1973) *Crystal Growth: an introduction*, North -Holland, Amsterdam.

[64] **Havlica J., S. Sahu**, (1992) Mechanism of ettringite and monosulphate formation, *Cement and Concrete Research*, **22**, 671-677.

[65] **Hinch E.J. and L.G. Leal**, (1972) The effect of Brownian motion on the rheological properties of a suspension of non-spherical particles, *Journal of Fluid Mechanics*, **52**, 683-712.

[66] **Hunter R.J.**, (2001), *Foundations of colloid science*, Oxford University Press, Oxford.

[67] **Jonathan L., P.V. Coveney, A. Whiting and R. Davey**, (1999) Design and synthesis of macrocyclic ligands for specific interaction with crystalline ettringite and demonstration

of a viable mechanism for the setting of cement, *The Royal Society of Chemistry; Perkin Transactions*, **2**, 1973-1981.

[68] **Jones F.E.**, (1939) The quaternary system CaO - Al_2O_3 - $CaSO_4$ - H_2O at 25°C, *Transactions of the Faraday Society*, **35**, 1484-1510.

[69] **Jones F.E.**, (1944) The quaternary system CaO - Al_2O_3 - $CaSO_4$ - H_2O at 25°C. Equilibria with crystalline $Al_2O_3 \cdot 3H_2O$, alumina gel and solid solutions., *Journal of Physical Chemistry*, **48**, 311-356.

[70] **Khamskii V.E.**, (1969) *Crystallization from solutions*, Consultants Bureau, New York.

[71] **Kingston M.H. and S.J. Haswell**, (1997) *Microwave enhanced chemistry: fundamentals, sample preparation, and applications*, ACS Professional Reference Book Series, American Chemichal Society, Washinton DC.

[72] **Kirby G.H. and A.J. Lewis**, (2002) Rheological property evolution in concentrated cement-polyelectrolyte suspensions, *Journal of American Ceramic Society*, **85**, 2989-2994.

[73] **Krieger I.M.**, (1972) Rheology of monodisperse latices, *Advances in Colloid and Interface Science*, **3**, 111-136.

[74] **Krishna Rama Siva D., C.K. Chaitanya, S.K. Seshadri and T.S. Sampath Kumar**, (2002) Fluorinated hydroxyapatite by hydrolysis under microwave irradiation, *Trends in Biomaterials and Artificial Organs*, **16**(1), 15-17.

[75] **Kuroda T.**, (1985) Growth of a crystal surface with non-uniformity in supersaturation due to laminar flow of solution along the surface, *Journal of Crystal Growth*, **71**, 84-94.

[76] **Kuzel H.J.**, (1965) Synthese und Röntgenuntersuchung des $3CaO \cdot Al_2O_3 \cdot CaSO_4 \cdot 12H_2O$, *Neues Jahrbuch für Mineralogie*, **Monatshefte**, 193-197.

[77] **Landau L.D. and E.M. Lifshitz**, (1959) *Fluid mechanics*, Butterworth-Heinemann, Oxford.

[78] **Lea F.M. and C.H. Desch**, (1956) *The chemistry of cement and concrete*, Edward Arnold, London.

[79] **Lei G.W. and J.L. Struble**, (1997) Microstructure and flow behaviour of fresh cement paste, *Journal American Ceramic Society*, **80**, 2021-2028.

[80] **Lerch W., F.W. Ashton and R.H. Bogue**, (1929) The sulphoaluminates of calcium, *Bureau of Standards; Journal of Research*, **2**(4), 715-731.

[81] **Li G., P. Le Bescop and M. Moranville**, (1967) Synthesis of the U phase ($4CaO \cdot 0.9Al_2O_3 \cdot 1.1SO_3 \cdot 0.5Na_2O \cdot 16H_2O$), *Cement and Concrete Research*, **27**, 7-13.

[82] **Lidström P., J. Tierney, B. Wathey and J. Westman**, (2001) Microwave assisted organic synthesis-a review, *Tetrahedron*, **57**, 9225-9283.

[83] **Locher F.W., W. Richartz and S. Sprung**, (1976) Erstarren von Zement. Teil I: Reaktion und Gefügeentwicklung, *Zement-Kalk-Gips*, **29**(10), 435-442.

[84] **Lopez X., P.H. Valvante and M.J. Blunt**, (2003) Predictive network modeling of single-phase non-Newtonian flow in porous media, *Journal of Colloid and Interface Science*, **264**, 256-265.

[85] **Mehta P.K. and P.J.M. Monteiro**, (1997) *Concrete microstructure, properties and materials*, International Series in Civil Engineering and Engineering Mechanics, Prentice-Hall, Englewood Cliffs.

[86] **Mehta P.K.**, (1969) Morphology of calcium sulfoaluminate hydrates, *Journal of The American Ceramic Society - Discussions and Notes*, **52**(9), 521-522.

[87] **Mehta P.K.**, (1976) Scanning electron micrograph studies of ettringite formation, *Cement and Concrete Research*, **6**, 169-182.

[88] **Meller N., C. Hall, A.C. Jupe, S.L. Colston, S.D.M. Jacques, P. Barnes and J. Phipps**, (2004) The paste hydration of brownmillerite with and without gypsum: a time resolved synchrotron diffraction study at 30, 70, 100 and 150°C, *Journal of Materials Chemistry*, **14**, 428-435.

[89] **Meller N., C. Hall and J. Crawshaw**, (2004) ESEM evidence for through-solution transport during brownmillerite hydration, *Journal of Materials Science*, **39**, 6611-6614.

[90] **Meredith P., A. M. Donald, N. Meller and C. Hall**, (2004) Tricalcium aluminate hydration: microstructural observations by in-situ electron microscopy, *Journal of Materials Science*, **39**, 997-1005.

[91] **Moore A.E. and Taylor H.F.W.**, (1970) Crystal structure of ettringite, *Acta Crystallographica*, **B**(26), 1048-1049.

[92] **Moore E. and L. Smart**, (2001) *Solid state chemistry: an introduction*, Nelson Thornes, Cheltenham.

[93] **Mori H. and K. Minegishi**, (1968) Effect of temperature on the early hydration of the system $3CaO{\cdot}Al_2O_3$-$CaSO_4{\cdot}2H_2O$-$Ca(OH)_2$-H_2O, *Vth International Symposium on Chemistry of Cement*, **II**, 349-361.

[94] **Mullin J.W.**, (1992) *Crystallization*, Butterworth-Heinemann, 3rd edition, Oxford.

[95] **Muncaster G., A.T. Davies, G. Sankar, C. Richard, A. Catlow, J. M. Thomas, S.L. Colston, P. Barnes, R.I. Walton and D. O'Hare**, (1968) On the advantages of the use of the three-element detector system for measuring EDXRD patterns to follow the crystallisation of open-framework structures, *Physical Chemistry Chemical Physics*, **2** 3523-3527.

[96] **Myneni S.C.B., S.J. Traina and T.J. Logan**, (1998) Ettringite solubility and geochemistry of the $Ca(OH)_2$ - $Al_2(SO_4)_3$ - H_2O system at 1 atm and 298 K, *Chemical Geology*, **148**, 1-19.

[97] **Nancollas G.H.**, (1979) The growth of crystals from solution, *Advances in Colloid and Interface Science*, **10**, 215-252.

[98] **Nelson E.B.**, (1990) *Well cementing*, Schlumberger Educational Services, Texas, 4-1.

[99] **Nishikawa T., K. Suzuki, S. Ito, K. Sato and T. Takebe**, (1992) Decomposition of synthesized ettringite by carbonation, *Cement and Concrete Research*, **22**, 6-14.

[100] **Nývlt J.**, (1971) *Industrial crystallization from solution*, Butterworth & Co, London.

[101] **Odler I., S. Abdul-Maula and Lu Zhongya**, (1987) Effect of hydration temperature on cement paste structure, *In Proceedings of Material Research Society Symposium*, **85**, 139-144.

[102] **Odler I. and R. Wonneman**, (1980) Hydration of C_3A in portland cement in the presence of different forms of calcium sulfate, *7th International Congress on the Chemistry of Cement*, Paris, 510-513.

[103] **Ogawa K. and D.M. Roy**, (1981) $C_4A_3\overline{S}$ hydration ettringite formation, and its expansion mechanism: I. expansion; ettringite stability, *Cement and Concrete Research*, **11**, 741-750.

[104] **O'Hare D., J.S.O. Evans, R.J. Francis, P.S. Halasyamani, P. Norby and J. Hanson**, (1998) Time-resolved, in-situ X-ray diffraction studies of the hydrothermal synthesis of microporous materials, *Microporous and Mesoporous Materials*, **21**, 253-262.

[105] **Onsager, L.**, (1949) The effects of shape on the interaction of colloidal particles, *Annals New York Academy of Science*, **51**, 627-659.

[106] **Papo A.**, (1988) Rheological models for gypsum plaster pastes, *Rheological Acta*, **27**, 320-325.

[107] **Pascal J.P. and H. Pascal**, (1995) On some non-linear shear flows of non-Newtonian fluids, *International Journal of Non-Linear Mechanics*, **30**(4), 487-500.

[108] **Perkins R.B. and C.D. Palmer**, (1999) Solubility of ettringite $(Ca_6[Al(OH)_6]_2(SO_4)_3 \cdot 26H_2O)$ at 5-75°C, *Geochimica et Cosmochimica Acta*, **63**(13,14), 1969-1980.

[109] **Petrov T.G., E.B. Treivus and A.P. Kasatkin**, (1969) *Growing crystals from solution*, Consultants Bureau, New York.

[110] **Prince W., M. Edwards-Lajnef and P.C. Aïtcin**, (2002) Interaction between ettringite and a polynaphthalene sulfonate superplasticizer in a cementitious paste, *Cement and Concrete Research*, **32**, 79-85.

[111] **Quemada D. and C. Berli**, (2002) Energy of interaction in colloids and its implications in rheological modeling, *Advances in Colloid and Interface Science*, **98**, 51-85.

[112] **Quemada D.**, (1982) Unstable flows of concentrated suspensions, *Lecture Notes in Physics*, 210-247.

[113] **Ramachandran V.S. and J.J. Beaudoin**, (2001) *Handbook of analytical techniques in concrete*, National Reasearch Council of Canada, Ottawa.

[114] **Reardon E.J.**, (1990) An ion interaction model for the determination of chemical equilibria in cement/water systems, *Cement and Concrete Research*, **20**, 175-192.

[115] **Rueb C.J. and C.F. Zukoski**, (1996) Viscoelastic properties of colloidal gels, *Journal of Rheology*, **41**(2), 197-218.

[116] **Rueb C.J. and C.F. Zukoski**, (1998) Rheology of suspensions of weakly attractive particles: approach to gelation, *Journal of Rheology*, **42**(6), 1451-1476.

[117] **Satava V. and O. Veprek**, (1975) Thermal decomposition of ettringite under hydrothermal conditions, *Journal American Ceramic Society*, **58**, 357-359.

[118] **Schramm G.**, (2000) *A practical approach to rheology and rheometry*, Gebrueder Haake GmbH, Second edition, Karlsruhe.

[119] **Schuster M. and H. Göbel**, (1997) Application of graded multilayer optics in X-ray diffraction, *Advances in X-ray Analysis*, **39**, 57-71.

[120] **Scrivener K.L. and W. Wieker**, (1992) Advances in hydration at low, ambient and elevated temperatures, *In Proceedings of the 9th International Congress on Chemistry of Cement*, **1** 449-482.

[121] **Sgualdino G, G. Vaccari, G. Mantovani and D. Aquilando**, (1996) Implications of crystal growth theories for mass crystallization: application to crystallization of sucrose, *Progress in Crystal Growth and Characterization*, **32** 225-245.

[122] **Shahwana R. and X. Turrillas**, (1997) Hydration kinetics of $CaAl_2O_4$ using synchrotron energy-dispersive diffraction, *Thermochimica Acta*, **302**, 25-34.

[123] **Shimada Y. and J.F. Young**, (2004) Thermal stability of ettringite in alkaline solutions at 80°C, *Cement and Concrete Research*, **34**, 2261-2268.

[124] **Simon B. and R. Boistelle**, (1981) Crystal growth from low temperature solutions, *Journal of Crystal Growth*, **52**, 779-788.

[125] **Sohn D. and D.L. Johnson**, (1999) Microwave curing effect on the 28-day strength of cementitious materials, *Cement and Concrete Research*, **29**, 241-247.

[126] **Söhnel O. and J. Garside**, (1992) *Precipitation: basic principles and industrial applications*, Butterworth-Heinemann Limited, Oxford.

[127] **Starov V., V. Zhdanov, M. Meireles and C. Molle**, (2002) Viscosity of concentrated suspensions: influence of cluster formation, *Advances in Colloid and Interface Science*, **96**, 279-293.

[128] **Struble L.J. and G.K. Sun**, (1995) Viscosity of portland cement paste as a function of concentration, *Advance Cement Based Materials*, **2**, 62-69.

[129] **Sunagawa I.**, (1981) Characteristics of crystal growth in nature as seen from the morphology of mineral crystals, *Bulletin Minéralogique*, **104**, 81-87.

[130] **Tattersall G.H. and P.F.G. Banfill**, (1983) *The rheology of fresh concrete*, Pitman, London.

[131] **Taylor H.F.W.**, (1997) *Cement chemistry*, Thomas Telford Publishing, London.

[132] **Turrell G. and J. Corset**, (1996) *Raman microscopy: developments and applications*, Academic Press, London.

[133] **Von Hippel A.R.**, (1954) *Dielectric materials and applications*, MIT Press, Cambridge, USA.

[134] **Vladu C.M., C. Hall and G.C. Maitland**, (2005) Flow properties of freshly prepared ettringite suspensions in water at 25°C, *Journal of Colloid and Interface Science*, article in press (doi:10.1016/j.jcis.2005.07.052).

[135] **Walton R.I. and D. O'Hare**, (2000) Watching solid crystallise using in situ powder diffraction, *Chemical Communications*, 2283-2291.

[136] **Warren C.J. and E.J. Reardon**, (1994) The solubility of ettringite at 25°C, *Cement and Concrete Research*, **24**(8), 1515-1524.

[137] **Wierenga A.M. and A.P. Philipse**, (1996) Low-shear viscosities of dilute dispersions of colloidal rodlike silica particles in cyclohexane, *Journal of Colloid and Interface Science*, **180**(2), 360-370.

[138] **Wierenga A.M. and A.P. Philipse**, (1996) Low-shear viscosity of isotropic dispersions of (Brownian) rods and fibres; a review of theory and experiments, *Colloids and Surfaces A: Physicochemical and Engineering Aspects*, **137**(1-3), 355-372.

[139] **Wierenga A.M. and A.P. Philipse**, (1997) Low-shear viscosity of (semi-) dilute, aqueous dispersions of charged boehmite rods: dynamic scaling of double layer effects, *Langmuir*, **13**, 4574-4582.

[140] **Wilcox W.R.**, (1993) Transport phenomena in crystal growth from solution, *Progress in Crystal Growth and Characterization*, **26**, 153-194.

[141] **Zirnsak M.A., D.U. Hur and D.V. Boger**, (1994) Normal stresses in fibre suspensions, *Journal of Non-Newtonian Fluid Mechanics*, **54**, 153-193.

[142] http://www.bruker-axs.de/

[143] http://www.ccdc.cam.ac.uk/products/csd$_s$ystem/mercury/

[144] http://www.lsbu.ac.uk/water/microwave.html.

[145] http://www.victrex.com/

Appendix A
Phase relations in CaO - Al_2O_3 - $CaSO_4$ - H_2O system

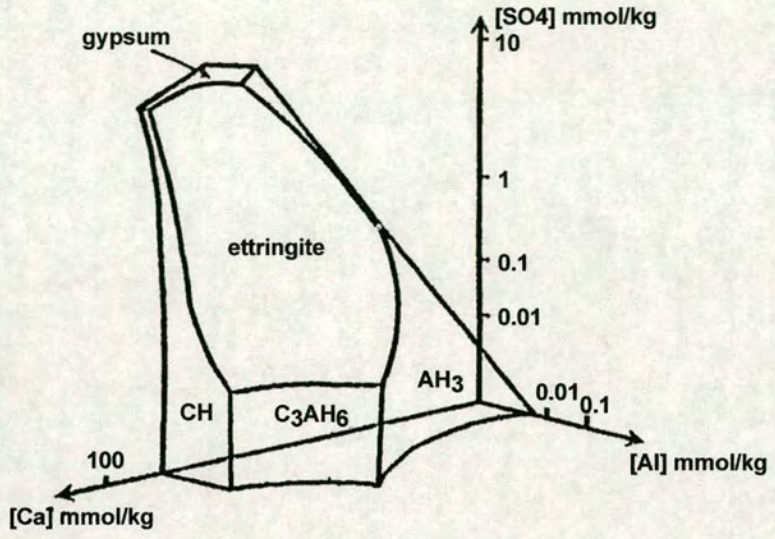

(a)

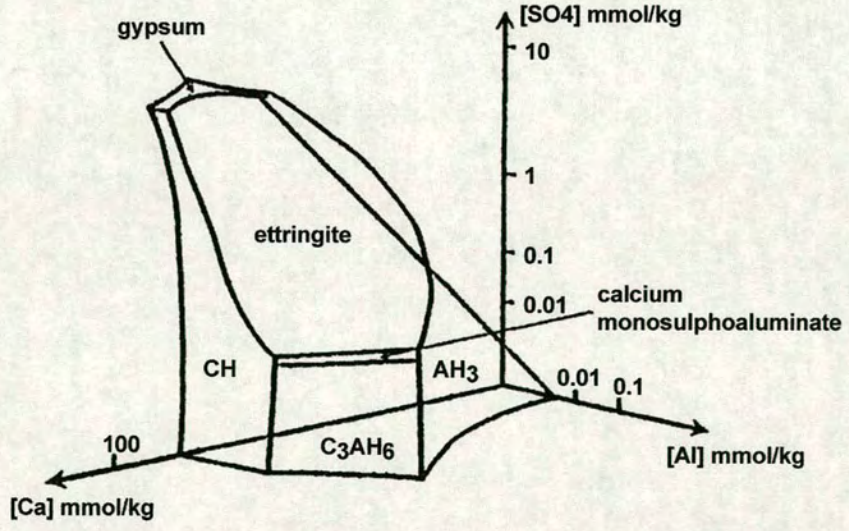

(b)

Figure A.1: *Phase relations in the system CaO - Al_2O_3 - $CaSO_4$ - H_2O at* ***(a)*** *25°C and* ***(b)*** *50°C (according to Atkins and Glasser [3])*

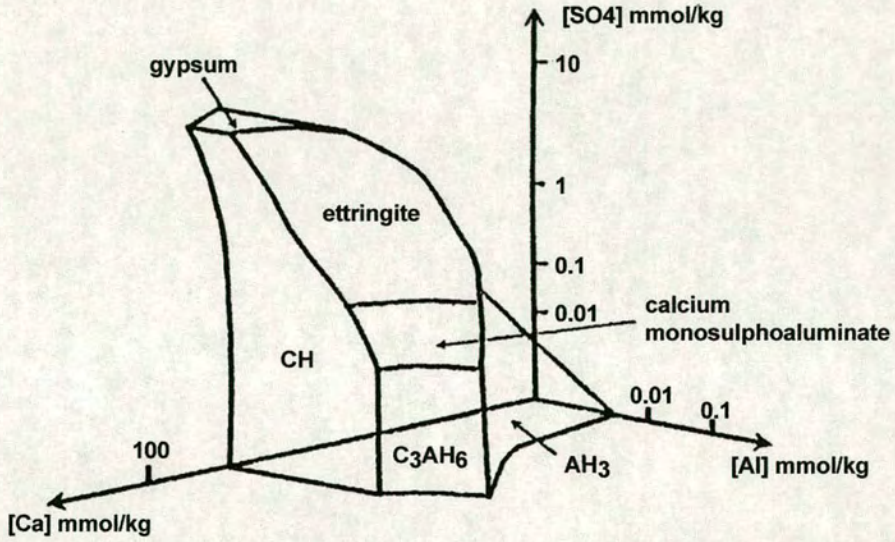

Figure A.2: *Phase relations in the system CaO - Al_2O_3 - $CaSO_4$ - H_2O at 80° C (according to Atkins and Glasser [3])*

Invariant point	T(°C)	$[SO_4]$	[Ca]	[Al]
In water				
C_3AH_6 + AF_t	25	0.015	21.95	0.010
C_3AH_6 + AF_m	25[a]	0.020	21.95	0.09
C_3AH_6 + AF_m	50	0.040	15.95	0.040
C_3AH_6 + AF_m	85	0.060	10.65	0.308
AF_m + AF_t	25[a]	0.007	21.95	0.023
AF_m + AF_t	50	0.042	15.95	0.042
AF_m + AF_t	85	0.41	11.33	0.016
AF_t + $C\bar{S}H_2$	25	12.17	33.3	1e-7
AF_t + $C\bar{S}H_2$	50	12.57	27.92	1e-4
AF_t + $C\bar{S}H_2$	85	10.70	20.72	0.004
In 0.5M NaOH				
C_3AH_6 + AF_t	25	1.981	0.995	0.112
C_3AH_6 + AF_m	50	20.14	0.72	0.448
C_3AH_6 + AF_m	85	54.87	0.325	5.20
AF_m + AF_t	50	66.93	0.841	0.155
AF_m + AF_t	85	183.9	2.056	0.354
AF_t + $C\bar{S}H_2$	25	197.4	11.22	1e-6
AF_t + $C\bar{S}H_2$	50	214.0	10.47	0.001
AF_t + $C\bar{S}H_2$	85	226.0	8.22	0.255
In 1M NaOH				
C_3AH_6 + AF_t	25	11.22	0.435	0.189
C_3AH_6 + AF_m	50	91.13	0.303	0.667
C_3AH_6 + AF_m	85	193.1	0.202	6.90
AF_m + AF_t	50	222.0	0.547	0.199
AF_m + AF_t	85	420.7	1.699	0.377
AF_t + $C\bar{S}H_2$	25	432.8	8.81	1e-5
AF_t + $C\bar{S}H_2$	50	456.0	8.44	0.003
AF_t + $C\bar{S}H_2$	85	473.7	6.76	0.90

[a]Metastable assemblages

Table A.1: *Pseudo-invariant point aqueous compositions in the CH saturated region of the CaO - Al_2O_3 - $CaSO_4$ - H_2O system, as function of temperature and alkali content (from Glasser et al. [30, 31]). Concentrations are given in mM/L.*

Ratio SO_4/Al	[NaOH] M	pH	$SI_{C_3AH_6}$	SI_{AF_t}	SI_{AF_m}	$SI_{'U-phase'}$	SI_{CH}	$SI_{C\bar{S}H_2}$
3:1	0.2	12.7	0.0	0.0	-0.4	-0.7	0.0	-2.7
3:1	0.5	13.1	0.0	0.0	-0.4	0.0	0.0	-2.7
3:1	1	13.3	-0.2	-0.7	-0.8	0.0	0.0	-2.8
1:1	0.2	12.8	0.0	0.0	-0.4	-0.8	0.0	-2.7
1:1	0.5	13.1	0.0	0.0	-0.4	0.0	0.0	-2.7
1:1	1	13.4	0.0	-1.2	-0.8	0.0	0.0	-3.0

Table A.2: *Phase assemblage the system CaO - Al_2O_3 - $CaSO_4$ - H_2O at 25°C. Predictions of Clark and Brown [23] calculated using PhreeqC based on solubility products values (k_{sp}) reported by Damidot and Glasser [31]. SI = 0.0 indicates saturation while a negative value indicates undersaturation.*

Appendix B
Experimental crystal growth study

Sample	Time Taken (min)	Elements (mmol/L) Al	Ca	SO_4	pH	T(°C)
1	1	4.124	16.130	14.381	11.032	26.3
2	30	2.194	11.604	11.088	11.178	22.0
3	60	0.953	10.195	10.094	11.281	20.7
4	90	0.649	9.759	9.507	11.520	20.1
5	120	0.474	9.047	9.080	11.544	19.9
6	150	0.458	8.983	9.129	11.488	20.1
7	180	0.326	8.755	8.944	11.562	20.3

Table B.1: *Concentration of the main species in the supernatant determined by ICP-AES in the crystallization by evaporation experiment. All concentration are expressed in mmol/L. The analytical precision is considered to be better than 1%.*

Sample	Time Taken (min)	Elements (mmol/L) Al	Ca	SO_4	pH	T(°C)
1	5	5.724	17.990	14.192	9.636	51.4
2	30	0.588	15.399	14.489	9.956	32.7
3	60	0.282	14.752	14.243	10.006	25.9
4	90	0.170	13.873	13.580	10.173	23.5
5	120	0.147	14.368	14.082	10.178	22.2
6	150	0.149	14.778	14.201	10.191	21.9
7	180	0.137	14.856	14.219	10.236	21.6

Table B.2: *Concentration of the main species in the supernatant determined by ICP-AES in the crystallization by cooling experiment. All concentration are expressed in mmol/L. The analytical precision is considered to be better than 1%.*

Appendix C
Mineralogical model of the early cement hydration.

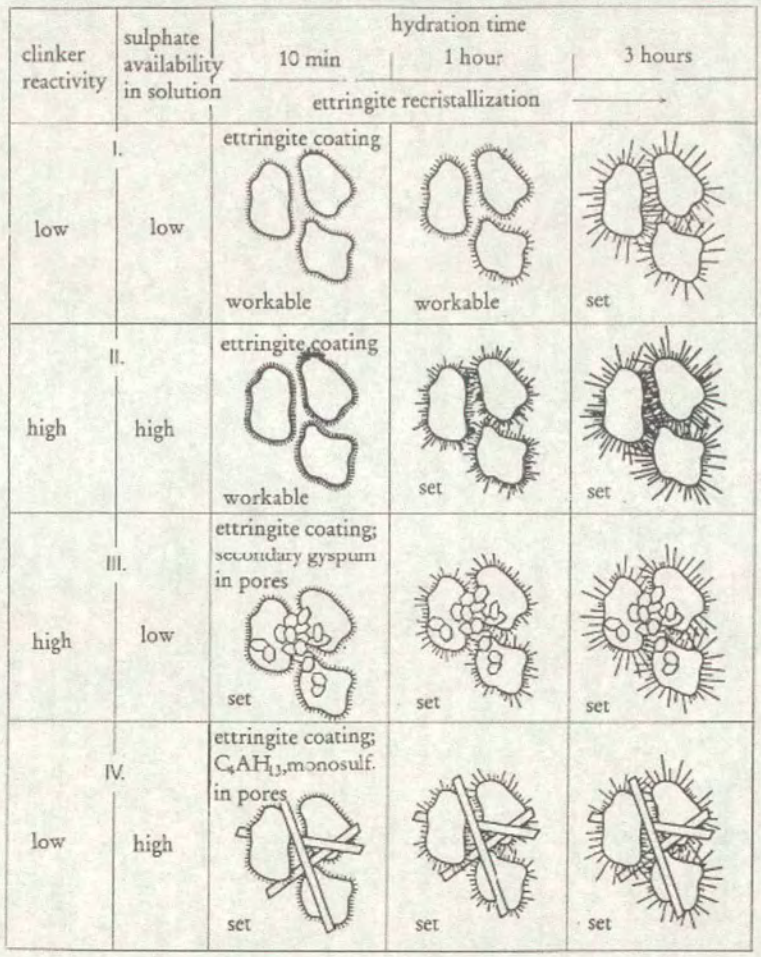

Figure C.1: *Summary of the early cement hydration according to Locher [83]*